

UNIVERSIDADE DE SÃO PAULO
Instituto de Astronomia, Geofísica e Ciências Atmosféricas
Departamento de Astronomia

André Zamorano Vitorelli

**Intervalos de Magnitude
e
Propriedades Físicas de Sistemas de Galáxias**

São Paulo
2015

André Zamorano Vitorelli

Intervalos de Magnitude
e
Propriedades Físicas de Sistemas de Galáxias

Dissertação apresentada ao Departamento de Astronomia do Instituto de Astronomia, Geofísica e Ciências Atmosféricas da Universidade de São Paulo como requisito parcial para obtenção do título de Mestre em Ciências.

Área de concentração: Astronomia.
Orientador: Prof. Dr. Eduardo S. Cypriano

São Paulo
2015

Resumo

Nesta dissertação de mestrado estudamos a relação entre as propriedades físicas de grupos ou aglomerados de galáxias e o intervalo de magnitudes entre a galáxia central e galáxias satélites brilhantes. Para isto, utilizamos dados do levantamento CFHT Stripe-82, em conjunto com o catálogo de aglomerados redMaPPer, que utiliza dados do levantamento SDSS DR8. Com isto, temos 1502 sistemas e mais de 4 milhões de galáxias. Aplicamos a técnica de lentes gravitacionais fracas para obtermos a massa e a concentração de perfis radiais através da combinação de muitos sistemas como se fosse um único, na técnica conhecida como empilhamento (*stacking*). Os sistemas foram divididos em pilhas de acordo com *redshift* e riqueza e então, destes grupos, em intervalos de magnitude $\Delta M_{1-2(4)}$ grandes, médios e pequenos. Calculamos uma estimativa para o cisalhamento (*shear*) médio em intervalos de raio logaritmicamente espaçados. Fazendo o uso de um modelo parametrizado da distribuição radial de massa, investigamos os posteriores dos parâmetros através de um método de MCMC. Comparamos os resultados obtidos e não encontramos evidências significativas de que os sistemas com maiores intervalos de magnitude (fósseis ou quase-fósseis) têm, em média, concentrações maiores, conforme indicado na literatura.

Abstract

We study the relationship between the physical properties of groups and clusters of galaxies and the magnitude gap between the central galaxy and bright satellites. In this work we use data from the CFHT Stripe-82 Survey, together with the redMaPPer cluster catalogue, based on SDSS DR8. We apply cross-correlation weak lensing analysis on stacks defined by placing systems into redshift and richness bins, and then subdividing these into larger, average and smaller magnitude gap (ΔM_{1-2}) ensembles. We calculate estimators for the mean shear in logarithmically spaced radial bins. Using a parametric model for the mass distribution, we probe the posterior distribution of the parameters using a MCMC method. We compare the obtained results and do not find evidence that systems with larger magnitude gaps correlate with larger concentrations, as indicated by literature.

この道や行く人なしに秋の暮

―松尾芭蕉

ANDRÉ ZAMORANO VITORELLI

MAGNITUDE GAPS AND THE PHYSICAL PROPERTIES OF GALAXY SYSTEMS

INSTITUTO DE ASTRONOMIA, GEOCIÊNCIAS E CIÊNCIAS ATMOSFÉRICAS
UNIVERSIDADE DE SÃO PAULO

Copyright © 2015 André Zamorano Vitorelli

PUBLISHED BY INSTITUTO DE ASTRONOMIA, GEOCIÊNCIAS E CIÊNCIAS ATMOSFÉRICAS UNIVERSIDADE DE SÃO PAULO

[TUFTE-LATEX.GITHUB.IO/TUFTE-LATEX/](https://github.com/johndcook/tufte-latex)

Licensed under the Apache License, Version 2.0 (the ``License"); you may not use this file except in compliance with the License. You may obtain a copy of the License at <http://www.apache.org/licenses/LICENSE-2.0> Unless required by applicable law or agreed to in writing, software distributed under the License is distributed on an ``AS IS'' BASIS, WITHOUT WARRANTIES OR CONDITIONS OF ANY KIND, either express or implied. See the License for the specific language governing permissions and limitations under the License.

First printing, September 2015

Contents

<i>I</i>	<i>Theory</i>	23
1	<i>Introduction</i>	25
2	<i>Dynamics and Properties of Galaxy Systems</i>	45
3	<i>Gravitational Lensing</i>	65
<i>II</i>	<i>Application</i>	79
4	<i>Methodology</i>	81
5	<i>Results and Discussions</i>	103
6	<i>Conclusions and Perspectives</i>	121
<i>III</i>	<i>References and Index</i>	123
	<i>Bibliography</i>	125
	<i>Index</i>	143

List of Figures

- 1.1 The all sky measurements of temperature deviations from the average of the Cosmic Microwave Background [Planck Collaboration et al., 2015]. 37
- 1.2 Distribution of galaxies of the 2dF Galaxy Survey [Colless et al., 2001]. 42
- 1.3 A comparison between the Bolshoi simulation and SDSS observation of the nearby universe. *Sources: Nina McCurdy/University of California, Santa Cruz; Ralf Kaehler and Risa Wechsler/Stanford University; Sloan Digital Sky Survey; Michael Busha/University of Zurich* 43

- 2.1 Results from simulations showing the characteristic steepening slope of dark matter density profiles. *Source: Navarro et al. [1996]* 47
- 2.2 The complex, smooth, distribution of matter after the growth of structure in the universe can be understood as an interpolation of spherically collapsed halos. *Source: Cooray and Sheth [2002]* 48
- 2.3 Regions with higher density due to long modes tend to form more collapsed structures due to a higher local average density, which influences the mass distribution around clusters. *Source: Peacock [2003]* 51
- 2.4 The galaxy cluster Abell 2218 as imaged by Hubble, provides a display of the characteristic image of the environment of galaxy clusters, as well as their effect not only in the environment, but, as we will later see, on the images of background galaxies. The yellowish hue of elliptical galaxies and a dominant cD central galaxy shows how the galaxy population of galaxy clusters stand apart from that of galaxies of the field. The thin, distorted arcs are gravitationally lensed images of background galaxies, that we will see in chapter 3. *Source: Image Credit: NASA, ESA, and Johan Richard (Caltech, USA)* 54
- 2.5 The principle of dynamical friction. The gravitational field of a galaxy of mass M and velocity \vec{v} accelerates other smaller galaxies to its track, which then act as a force pulling the massive galaxy backwards. *Source: [Lima Neto, 2014]* 55
- 2.6 A typical massive cD galaxy with an active nucleus, M87. (*Source: Ragniere Menezes, IAG Telescope, OPD*) 56

- 3.1 **Upper:** The double quasar QSO0957 + 561 depicted by the Hubble Space Telescope in the upper right area of the image as the "star like" objects with diffraction rays. The reddish light between them is the forefront deflector galaxy. Their spectra matches as an object at redshift $z = 1.413$, with the deflector at $z = 0.355$. The separation is of about $6''$. *Source: ESO/NASA. Lower:* Reproduction of the spectra of each component, from Walsh et al. [1979] 66
- 3.2 Gravitational lens geometry. In the thin lens approximation we can consider that all the change in direction of the light rays takes place in a specific plane. Here, all distances used must specifically be angular diameter distances, since the large scale structure of space-time is not euclidean. *Source: [Bartelmann and Schneider, 2001]* 68

- 3.3 The effects of the two components of the lensing transformation. κ changes the size of images while γ distorts images laterally. (Source: *Wikipedia*) 70
- 3.4 Considering a spherical symmetry, we can write the ellipticity of an object as a sum of a tangential component and a cross component. Source: *Mirian Castejon Molina* 76
- 4.1 The galaxies in the centre of this optical image are an example of galaxy cluster as imaged by SDSS, displaying the characteristic yellowish hue of elliptical galaxies. Source: *SDSS / Alexie Leauthaud CS82 presentation* 83
- 4.2 Distribution of ellipticities in the x, y coordinate frame of the CS82 survey, as determined by LensFit. The dashed line is the average in both ellipticity directions. 84
- 4.3 Probability mass function for all galaxies identified by redMaPPer as possible members of a system, by radius. We can see that outer radii galaxies have a wider distribution. In the left panel, point transparency was adjusted to reflect galaxy brightness, so that fainter galaxies appear as faint points (in log scale). On the right, the blue/red points indicate lower/higher cluster redshifts respectively. At high redshifts, probabilities tend to be lower. 85
- 4.4 Distributions for the calculated magnitude gaps and errors for ΔM_{1-2} and ΔM_{1-4} . 88
- 4.5 Fractions of clusters by particular magnitude gaps. Positive magnitude gaps generally increase with radius, whereas for the fossil fraction increases with smaller radii, which justifies calling smaller radius a less strict definition. 89
- 4.6 **Upper:** CAMB generated power spectrum at redshift zero used for this work, using Planck 2015 data. **Lower:** The respective matter-matter correlation function, zoomed into the characteristic acoustic oscillation peak. 94
- 4.7 Test of the full model showing the individual contributions of the miscentered clusters, the correctly centred ones, the two-halo term, and the baryonic mass of the central galaxy. 95
- 4.8 The division of the full sample into sub-samples of coherent richness and redshifts are then divided into classes of magnitude gaps. On the course of this work, we display consistently smaller gaps as blue, larger gaps as red and intermediate as green. Richness will always be higher in upper panels and redshift higher on the right. 97
- 4.9 The difference between the redMaPPer calculated i -band luminosity and the ones calculated by our absolute i band magnitudes. The difference occurs because of different luminosity distances owing to different cosmological parameters. This comparison has been used to correct for full cluster luminosities. 101
- 5.1 Results for the tangential shear in logarithmically spaced radial bins for the $\Delta M_{1-2(4)}$ defined stacks. From left to right, increasing redshift bins and from up to down, decreasing redMaPPer richness λ bins. The small lower panel in each of the 6 groups is the results for the cross shear. The 6 upper panels are ΔM_{1-2} , and the 6 lower ΔM_{1-4} 105
- 5.2 Example of a triangle plot for the 5 parameter model for the low redshift, low richness, middle magnitude gap stack. The whole result gallery with triangle plots and fit results as below for each of the fits will be made available online, together with the code as mentioned before. 106
- 5.3 Example fit of the 5-parameter model into the low redshift, low richness, small ΔM_{1-2} stack. The colour curves are partial contributions to the overall profile, the black solid line the fitted curve and the gray curves a random sample of parameters drawn from their posterior probabilities distributions 107

- 5.4 2D histograms depicted by curves at half-maximum and 1/4 maximum for comparison between different models. On the upper panel, it is shown the ΔM_{1-2} selected, large magnitude gap, high λ , low z stack. On the lower, everything the same, but with the low λ stack. 110
- 5.5 Posterior distributions for masses and concentrations of all stacks for ΔM_{1-2} , in the 3 parameter model. Each pair mass/concentration side by side represent a bin in richness and redshift, with colours distinguishing between magnitude gaps. 111
- 5.6 Masses and concentrations for the 2 lower redshift bins, using 5 and 3 parameters. The gray lines in the background are indications of the slope of the Duffy $c - M$ relation Duffy et al. [2008] 112
- 5.7 Posterior distributions for masses and concentrations of all stacks for ΔM_{1-2} , in the 3 parameter model. 114
- 5.8 Results for the 3 main tracers of system mass: the M_{200} from weak lensing measurements, the average redMaPPer richness $\bar{\lambda}$ for each stacks, and the average luminosity $\bar{\lambda}$, also from the redMaPPer catalogue. 115
- 5.9 Plot for all objects, magnitude gap ΔM_{1-2} by i-band luminosity by redMaPPer. 116
- 5.10 The $c - M$ relation of Khosroshahi et al. [2007], **Left:** caption from the original: Comparison between the mass concentration in fossils and non-fossil groups and clusters. Three fossils with resolved temperature profile and two isolated OLEGs (diamonds) are compared with non-fossil clusters (open squares) from Pratt and Arnaud [2005]. The expected values of the dark matter concentration and its variation with the halo mass from the numerical studies of Dolag et al. [2004] and Bullock et al. [2001] also are presented. The reasonable agreement between the non-fossils mass concentration from Pratt and Arnaud [2005] with the dark matter concentration from the study of Dolag et al. [2004] suggest that the excess concentration in fossils is due to their dark matter concentrations. In low mass end, two recent estimates (90%confidence) for the concentration of NGC 6482, after accounting for the baryonic matter (see Humphrey et al. [2006] for details) are also shown (blue) which again lie above the numerical expectations.**Right:** The superimposed points from this work. 117
- 5.11 The probability distribution for the miscentered fraction is given by the distribution of correctly centred probabilities as calculated by the redMaPPer. The picture shows this distribution for the whole ensemble, but each stack has its own distribution calculated. 118
- 5.12 The probability distribution for the miscentered fraction is given by the distribution of correctly centred probabilities as calculated by the redMaPPer. The picture shows this distribution for the whole ensemble, but each stack has its own distribution calculated. 119

List of Tables

- 1.1 Measurements for Λ CDM cosmology by current CMB experiments. [Hinshaw et al., 2013, Planck Collaboration et al., 2015] Other model parameters suppressed for clarity 33
- 1.2 Sub-horizon sized matter overdensities evolution with time in different epochs. 40
- 2.1 Parameters of the bias equation as a function of $y = \log(\Delta)$ 52
- 4.1 Number of systems in each stack by ΔM_{1-2} . 96
- 4.2 Number of systems in each stack by ΔM_{1-4} . 96
- 4.3 Priors used with the MCMC. When absent, the method is equivalent to a δ_D prior on the exact value. 100
- 5.1 Marginalised median values for the parameters with 16th and 84th percentiles, together with averages in z , λ and L . M_{200} in $10^{13}M_{\odot}$, M_0 in $10^{11}M_{\odot}$, and L in $10^{10}L_{\odot}$, for the 3 models (up: Full,mid: $\sigma_{off} = 0.42h$,low: and $M_0 = 0$) 108
- 5.2 Marginalised median values for the parameters with 16th and 84th percentiles, together with averages in z , λ and L . M_{200} in $10^{13}M_{\odot}$, M_0 in $10^{11}M_{\odot}$, and L in $10^{10}L_{\odot}$, for the 3 models (up: Full,mid: $\sigma_{off} = 0.42h$,low: and $M_0 = 0$) 109
- 5.3 Comparison between quantiles out of different models, showing no significant difference 111
- 5.4 Probabilities for the parameters between two different magnitude gaps ΔM_{1-2} calculated by integrating the distribution of differences of random draws from the Markov chains, using the 3-parameter ($\sigma_{off} = 0.42h$ Mpc, no CG baryonic component) model. 113
- 5.5 Probabilities for rejecting one of the 4 null-hypotheses given that it is true of each set of concentration differences for each of the sets of concentration differences. 115

Acknowledgements

To my mother and brother, who took part on this entire journey to now,

To my father, who first inspired me to look to the stars,

To my beloved partner, Nathalia, for all the love and care and company and inspiration,

To my friends, Juca, Gabriel, Venom, Fair, Marô, Sher, Lyla, Suzana, Fernanda, Aline, Camilla, Joyce, Arthur, Catarina, Audrey, Geeh, Mandi, Amanda, Adriana, Lissa, Rafael Campos, Gustavo, José Thuorst, Thiago 'Zero', Thiago 'Capeta', Andrea and so many others for making my life an endless stream of fruitful discoveries and experiences,

To my coworker-friends Mirian, Nathália, Rogério, and Raniere for their company, council, care, and providing for a strong scientific environment.

To my advisor Prof. E. Cypriano, for the patience and guidance in these first steps,

To the professors I had the joy to learn from, both in IF and IAG at the University of São Paulo,

To the Brazilian people, who, hereby represented by CAPES and CNPq, entrusted me "to forward the search into the mysteries and marvellous simplicities of this strange and beautiful Universe, our home."

-[Misner et al., 1973]

*This work is dedicated to Évora,
and to each and every one
who flee from meaninglessness
even at unspeakable costs.*

Part I

Theory

Introduction

THE ROLE OF SYSTEMS OF GALAXIES, in both the massive clusters and in small groups, is becoming increasingly important in many fields of astrophysics. As some of the greatest gravitationally bound structures in the universe, they play a fundamental role both in testing new theories of gravity [Jain et al., 2013] and cosmology [Weinberg et al., 2013]. As enormous dynamical structures made mostly of Dark Matter, they can be used as "natural particle accelerators" in the case of merging clusters, testing possible dark matter self-interaction properties [Kahlhoefer et al., 2014]. In galactic astronomy, they provide insights into the evolution of galaxies [Dressler, 1984] and, through gravitational lensing, become natural telescopes to galaxies that would remain unseen with current technology [Zitrin et al., 2015, Tanvir et al., 2009]. In this context, the present work investigates properties of a particular subset of groups and clusters, those in which the central galaxy seems to be an overly dominant component in the central region of the system. The most extreme of those systems, usually called "fossils" are oftentimes thought to represent a relatively undisturbed sample of the structures in the universe - if that is the case, they could prove to be peculiarly interesting, as they would carry valuable information about the overall background evolution and conditions in earlier times in the universe. To carry out this investigation, we have measured the masses and radial mass distributions of galaxy systems through weak gravitational lensing and, together with photometric data, we have compared the magnitude gap - that is, the difference in magnitudes between the central galaxy (CG) and the brightest or

third brightest galaxy in the central region except for the CG - to the measured quantities and derived observables such as mass concentration and mass-to-luminosity ratios to search for any scaling relations.

The role of this work is, however, two-fold: as a masters' thesis, it must and will summarise the last two years work on the project and its results. Additionally, as a guide for future students, we will try to present the contents in a useful, self-contained as possible manner without turning it into a full scale review of the subjects presented, which would diminish the focus of the work.

In the following sections, we establish a stage in which the evolution of galaxies and galaxy systems take place. The second chapter will deal with the fundamental aspects of the evolution, dynamical properties and observables of galaxy clusters. The third will discuss the main technique used, which is Weak Gravitational Lensing. In the fourth chapter, we present the data used for our investigation, and chapters 5 and 6 will contain the respective results and discussion. Furthermore, a perspective outlook is offered in the final chapter.

1.1 *The Cosmological Scenario*

AS OF THIS WRITING a hundred years have passed since the discovery of the cornerstone of modern cosmology, which is Einstein's Theory of Gravity (ETG) ¹. It was only in the past two decades, however, owing to the revolutionary role of modern instrumentation - both in space and ground telescopes [[Weinberg et al., 2013](#)] -, that Cosmology has bloomed into its current form.

ETG is a *metric theory of gravity*, that is, one in which the effects of gravitation are explained as geometric properties of space-time. The main *heuristic* argument (but not fundamental property [[Fock, 1955/2015](#)]) of the theory is that a suitable change in geometry can account for gravitational acceleration: free-falling astronauts inside a space capsule, for example, cannot distinguish their movement in a gravitational field or empty space, except for minute tidal forces. Changes in geometry can be quantified as changes in the measurement of distances in small ds lengths or,

¹ To understand the reluctance of the author in calling the theory as "*General Relativity*", please refer to:

V. Fock. *The Theory of Space, Time and Gravitation*. Elsevier Science, 1955/2015. ISBN 9781483184906

more generally, by observing the change in *parallel transport*: in Euclidean space, transporting continuously a vector along a closed trajectory maintaining its orientation locally will bring the vector back to itself, with no change. The same is not true if the space is *curved*. Tests of ETG, from its effects on time and the bending of light, to parallel transport of angular momentum [Everitt et al., 2011, Will, 2014] have been tested extensively resulting in a resounding success.

By requiring that the theory is a *field theory* solely on the metric tensor² $g_{\mu\nu}$, with second order partial differential equations of motion, it can be shown that we are lead almost uniquely to

$$R_{\mu\nu} - \frac{1}{2}g_{\mu\nu}R = \frac{8\pi G}{c^4}T_{\mu\nu} - \Lambda g_{\mu\nu}, \quad (1.1)$$

where $R_{\mu\nu} = R_{\mu\rho\nu}^{\rho}$ ³ and $R = R_{\mu}^{\mu}$ are the Ricci Tensor and scalar, respectively, measuring the deviation of the volume of a geodesic ball in the curved manifold. $T_{\mu\nu}$ is the stress-energy(-momentum) tensor, that is, the collection of 4-momentum fluxes p_{μ} passing through a surface of constant x_{ν} , with $\mu, \nu = 0, 1, 2, 3$ being the usual time and space dimensions. These 16 equations⁴ are then non-linear, since the field equations propagate through the very same space-time metric it governs.

In addition to the field equations, we must specify the matter/energy content of the universe. To be useful, a cosmological model should be easy to describe - that means it should have symmetries or special properties that reduce the complexity of the equations [Ellis and van Elst, 1999]. One such usual choice for matter description is that of a mixture of fluids with physically motivated equations of states. Let us then consider a congruence of fluid particles world lines, having timelike 4-velocities⁵ $u^{\alpha}u_{\alpha} = -1$, under the effect of their own gravity. The time derivative of any tensor is given by $\dot{A} = A_{;\nu}u^{\nu}$. The motion of fluid particles can then be divided into distinct effects as⁶:

- expansion/contractions of volume, which are given by divergences of u^{α} , as $\theta := u^{\alpha}_{;\alpha}$,
- distortions in shape without change of volume which are trace free and orthogonal to u^{α} which is defined by the symmetric

² The metric tensor contains the recipe for measuring distances along lines, by $ds^2 = g_{\mu\nu}dx^{\mu}dx^{\nu}$, where we use the conventional Einstein notation: any indices repeated above and below are summed. So

$$g_{\mu\nu}dx^{\mu}dx^{\nu} := \sum_{\mu=0}^3 \sum_{\nu=0}^3 g_{\mu\nu}dx^{\mu}dx^{\nu}.$$

³ $R_{\mu\rho\nu}^{\alpha}$ is the Riemann Tensor, quantifying the local deviation of the manifold from an isometry of the Euclidean space.

⁴ 10 of which will be linearly independent only, as we require that the metric is symmetric $g_{\mu\nu} = g_{\nu\mu}$

⁵ in $c = 1$ units, which will help us make the equations more understandable - we can then return to $[c] = \text{km} \cdot \text{s}^{-1}$ with dimensional analysis in the end.

⁶ G. F. R. Ellis, R. Maartens, and M. A. H. MacCallum. *Relativistic Cosmology*. March 2012

tensor,

$$\sigma_{\mu\nu} := u_{(\mu;\nu)} - \frac{1}{3}\theta h_{\mu\nu} - \dot{u}_{(\mu}u_{\nu)},$$

where $u_{(\mu;\nu)} = (u_{\mu;\nu} + u_{\nu;\mu})/2$ and $h_{\mu\nu} = g_{\mu\nu} - u_{\mu}u_{\nu}$.

- rotation and vorticity, without change in shape which are anti-symmetric and given by $\omega_{\mu\nu} := u_{[\mu;\nu]} - \dot{u}_{[\mu}u_{\nu]}$ with $u_{[\mu;\nu]} = (u_{\mu;\nu} - u_{\nu;\mu})/2$, and
- acceleration due to non-gravitational forces, like pressure gradients, given by the time derivative of the 4-velocity $\dot{u}_{\mu} = u_{\mu;\nu}u^{\nu}$.

The covariant derivative of the 4-velocity can now be written as

$$u_{\mu;\nu} = \sigma_{\mu\nu} + \omega_{\mu\nu} + \frac{1}{3}h_{\mu\nu} + \dot{u}_{\mu}u_{\nu}. \quad (1.2)$$

The Riemann curvature tensor can be defined as:

$$u_{;\nu\beta}^{\alpha}u_{\mu} - u_{;\beta\nu}^{\alpha}u_{\mu} =: R_{\mu\beta\nu}^{\alpha}. \quad (1.3)$$

Now, contracting the expression above with $\alpha = \beta$ and multiplying by $u^{\mu}u^{\nu}$ we have the scalar equation

$$\theta_{;\nu}u^{\nu} - u_{;\nu\alpha}^{\alpha}u^{\nu} = R_{\mu\nu}u^{\mu}u^{\nu},$$

which gives us the *Ricci identity*:

$$\dot{\theta} - \dot{u}_{;\alpha}^{\alpha} + 2(\sigma^2 - \omega^2) + \frac{1}{3}\theta^2 = R_{\mu\nu}u^{\mu}u^{\nu}, \quad (1.4)$$

where σ and ω are the traces of their respective tensors. Now, the stress-energy tensor of a perfect fluid in thermodynamic equilibrium is given by:

$$T_{\mu\nu} = \left(\rho + \frac{p}{c^2}\right)u_{\mu}u_{\nu} + pg_{\mu\nu}, \quad (1.5)$$

where ρ is the matter energy density in the fluid and p is the isotropic pressure, and the field equations can be rewritten as [Hawking and Ellis, 1973]

$$R_{\mu\nu} = \kappa \left(T_{\mu\nu} - \frac{1}{2}Tg_{\mu\nu} \right) - \Lambda g_{\mu\nu},$$

where again T is the trace T_{α}^{α} and $\kappa = 8\pi G/c^4$. Now, contracting this with $u^{\mu}u^{\nu}$, using the perfect fluid stress-energy, one finds

$$R_{\mu\nu}u^{\mu}u^{\nu} = \frac{c^4\kappa}{2} \left(\rho + 3\frac{p}{c^2} \right) - \Lambda,$$

which, using equation 1.4 we can write:

$$\dot{\theta} - \dot{u}_{;\alpha}^{\alpha} + 2(\sigma^2 - \omega^2) + \frac{1}{3}\theta^2 = \frac{c^4\kappa}{2} \left(\rho + 3\frac{p}{c^2} \right) - \Lambda, \quad (1.6)$$

which is the *Raychaudhuri's Equation*, which is essentially the relativistic law of gravitational dynamics [Ellis, 2007]. In order to proceed with our model, we consider the *Cosmological Principle* which states that our outlook of and place in the cosmos should probably be a *common* one. More formally, that means that the properties of the universe in a sufficiently large scale should look the same for any observer at any particular point, and that we expect that *fundamental observers*, i.e., imagined observers which follow the local mean motion of matter, will experience an equivalent history of the Universe. In this case, the distortion in shape and the vorticity are zero. Now, if we at first consider only gravitational interactions, $u_{;\mu}^{\mu} = 0$, these assumptions will lead us to the Friedmann-Lemaitre model, with a Robertson-Walker metric (FLRW) as we see next. In order to implement the model, we can write the expansion as a function of the linear scale expansion by:

$$\theta = \frac{(d^3l)}{d^3l} = 3\frac{\dot{a}}{a},$$

where a is a normalised linear scale factor l/l_0 such that the volume V scale as $V \sim l^3$. Then, using 1.6 we arrive at:

$$3\frac{\ddot{a}}{a} = -\frac{c^4\kappa}{2} \left(\rho + 3\frac{p}{c^2} \right) + \Lambda. \quad (1.7)$$

The physical meaning of this *acceleration equation* is straightforward: a *change of rate* of the expansion or contraction of a small ball of radius l , relative to its size, is proportional to minus the energy density plus (3 times) the pressure, plus a

constant. Since the scale a is defined as positive, if the constant Λ is zero, the rate of expansion must be decreasing (or the rate of contraction, increasing). Without the constant Λ , this is a quantitative statement which states that *gravity is attractive*.

Now, it is clear that a static universe ($\dot{a} = \ddot{a} = 0$) must have $\Lambda > 0$, and therefore be unstable, because if we introduce a perturbation $l \rightarrow l + \delta l$ to a larger value, the matter density ρ increases, while Λ stays constant. Then $\ddot{a} > 0$ and the universe expands to infinity. Similarly, $l - \delta l$ will imply in $\ddot{a} < 0$ and the universe will collapse. So, *the universe should be either expanding or contracting, but not static*. From the first half of the twentieth century and on, however, evidence that the universe was expanding began accumulating [Slipher, 1917, Hubble, 1929, Sandage, 1958].

Turning back to our argument, if we use the conservation equation for fluids considering the expansion term, we have:

$$\begin{aligned} \dot{\rho} + \left(\rho + \frac{p}{c^2} \right) \theta &= 0 \\ \dot{\rho} a^2 + \underbrace{3\rho\dot{a}a}_{2\dot{\rho}a + \rho\dot{a}a} + 3\frac{p}{c^2}\dot{a}a &= 0 \\ (\dot{\rho}a^2) &= -a\dot{a} \left(\rho + 3\frac{p}{c^2} \right). \end{aligned} \quad (1.8)$$

Then, multiplying equation 1.7 by $\dot{a}a$, and substituting with 1.8 we finally arrive at

$$3\dot{a}^2 - c^4\kappa\rho a^2 - \Lambda a^2 = \text{const.} \quad (1.9)$$

This is the *Friedmann equation*, which governs the time evolution of FLRW universes. The constant term in the right hand side is a measure of the local curvature of space - that is, a 3-dimensional equal-time slice of the 4-dimensional manifold. Due to our assumption of homogeneity the curvature of space must be the same everywhere. Therefore, aspects of the global geometry of space-time can be constrained by its value. A positive curvature ("*spherical*") everywhere will lead to a closed universe, whereas for zero ("*flat*") or a negative ("*hyperbolic*") spatial curvature, the topology can be either compact or infinite [Lachieze-Rey and Luminet, 1995].⁷

⁷ Euclidean space is flat, simply connected and infinite. A 3-torus is also (locally) flat, but multiply connected, finite and compact.

The Friedmann equation can be written in the most usual form as

$$\left(\frac{\dot{a}}{a}\right)^2 = -\frac{8\pi G}{3}(\rho) + \frac{\Lambda c^2}{3} - \frac{Kc^2}{a^2}, \quad (1.10)$$

where K (not to be confused with κ) is the constant of 1.9. For any time-slice of the universe, K/a^2 will give the spatial curvature.

If we choose a coordinate system in which any observer that sees an isotropic universe has constant space coordinate values, we can see that the left-hand side of the equation is the rate of expansion at a time t per unit distance. Since the distance from an observer to an object is $r = a(t)x$, the rate of change in the distance is $\dot{r} = \dot{a}x + a\dot{x} = (\dot{a}/a)r + a\dot{x}$. Here, \dot{x} can be understood as a *peculiar velocity* of the object relative to the local isotropic frame and $(\dot{a}/a)r$ is the rate of recession of the isotropic observer frame and the isotropic object frame. In fact, the quantity $H(t) = (\dot{a}/a)$ can be directly measured if we assume that deviations from local mean motion should be randomly distributed, and measure the rate of recession of distant objects.

1.2 *The Standard Cosmological Model*

The above derivation gave us an equation to evaluate the dynamics of the background evolution of the universe. To employ it, we must now consider the contents making up the stress-energy tensor, which will be defined as fluids with some physically motivated equation of state ($p = \rho w$), and relate to present values. The scale factor a can be normalised to one at the present time, and for further convenience, we will define the present value of the Hubble factor $H(t)$ as $H(t_0) := H_0$, which is usually represented as $100h\text{km} \cdot \text{s}^{-1} \cdot \text{Mpc}^{-1}$ where h , or sometimes h_{100} is called the reduced Hubble constant. It is many times convenient to calculate quantities in Hubble constant independent units to compare results between different works.

For each type of content, the density can be written as a function of cosmological time as [Weinberg, 2008]

$$\rho \propto a^{-3(1+w)}. \quad (1.11)$$

For matter, dark or not, $w \approx 0$ and the density at a particular slice of time can be written as $\rho_m(t) = \rho_{m,0}/a^3$ respective to the current ρ_0 density. For radiation, we have $w = 1/3$ and then, $\rho_r = \rho_{\gamma,0}/a^4$ since not only the electromagnetic field density decreases but also the wavelengths (and hence photon energies) are changed due to gravitational effects [Weinberg, 2008]. Finally, we can, for Λ , define a density $\rho_\Lambda := \Lambda c^2/a^0$ which is constant.

The Friedmann equation is now, then:

$$H^2(t) = \frac{8\pi G\rho(t)}{3} - \frac{Kc^2}{a^2}, \quad (1.12)$$

with⁸

$$\rho(t) = \rho_r(t) + \rho_m(t) + \rho_\Lambda(t).$$

If space curvature $K = 0$ we have the critical density of the universe at time t given by:

$$\rho_{crit} = \frac{3H^2(t)}{8\pi G}. \quad (1.13)$$

It is useful to redefine the densities of contents as a fraction of the critical density, so that we can describe the contents of the universe in *density fractions*, as the behaviour of the solution will depend on these. For any fraction χ we can define

$$\Omega_\chi(t) := \frac{\rho_\chi(t)}{\rho_{crit}(t)}. \quad (1.14)$$

Even then, if we define a present time "curvature density" as

$$\Omega_K := -\frac{Kc^2}{H^2} := 1 - \Omega_M - \Omega_\gamma - \Omega_\Lambda, \quad (1.15)$$

we can rewrite the Friedmann equation as a function of current densities as:

$$H^2(t) = H_0^2 \left(\Omega_\Lambda + \frac{\Omega_k}{a^2} + \frac{\Omega_m}{a^3} + \frac{\Omega_r}{a^4} \right). \quad (1.16)$$

Since $H^2 = \dot{a}/a$, this is a first-order non-linear equation on $a(t)$, which can be solved algebraically for simple cases and numerically in general.

Until now, we have not discussed the nature of the Λ factor in the EFEs. There was no reason, at first, that the equations should

⁸ Usually, the mass and radiation densities can be further divided into physical components:

$$\rho_m = \rho_c + \rho_b$$

$$\rho_r = \rho_\gamma + \rho_\nu,$$

where ρ_c is the density of Cold Dark Matter, ρ_b is the density of baryons, ρ_γ is the density of photons, and ρ_ν is the density of neutrinos.

contain the constant Λ , but it also does not spoil "covariant conservation".⁹ Λ can be understood either as a dynamical property of empty space-time, as a part of the Einstein tensor (the left hand side of 1.1) or a universal vacuum density, as a part of the right-hand side. In this latter case, we can see that it acts as a constant density uniform fluid with negative pressure since $\rho_\Lambda \propto a^0$ implies that $p_\Lambda = -\rho_\Lambda/3$. Also, through the Raychaudhuri equation (specially, in its "Friedmann equation" form), it is clear that Λ violates the *strong energy condition* if the universe is expanding acceleratingly, since $\kappa'/2(\rho + 3p/c^2) - \Lambda < 0$. The same is thought to happen in the earliest times, during *inflation*, where the universe undergoes exponential expansion.

Recent experiments have been measuring the partial fractions of Dark Energy (DE), Dark Matter (DM), Baryonic Matter with increasing precision, arriving in a picture that is most consistent with a universe ruled by ETG with zero curvature and dominated by DE and DM [Smoot, 1999, Hinshaw et al., 2013, Planck Collaboration et al., 2015]. These elements combine to form the *Standard Model of Cosmology*, known as Λ CDM, a universe dominated by Dark Energy(Λ) and Cold (that is, non-relativistic) Dark Matter (CDM), which has been extremely successful in explaining the structure and evolution of the cosmos. Baryonic matter, the only fraction which currently has a micro-physical description, contributes only with $\sim 4\%$ of the total energy density. Some of the state-of-the-art measurements of the relevant parameters are in table 1.1

Parameter	WMAP9	Planck 2015	Parameter	Concordance
$\Omega_b h^2$	0.02264(50)	0.02230(14)	Ω_m	0.3
$\Omega_c h^2$	0.1138(45)	0.1188(10)	Ω_Λ	0.7
Ω_Λ	0.721(25)	0.6911(62)	Ω_K	0
Ω_K	$-0.37_{-(42)}^{+(44)}$	$-0.052_{-(55)}^{+(49)}$	H_0	70
H_0	70.0(2.2)	67.26(98)		

1.3 Measuring Very Large Distances

It has been shown by [Ehlers et al., 1968] and generalised to approximations by [Stoeger et al., 1995] that if all free falling

⁹ Covariant conservation, that is

$$(T^{\mu\nu})_{;\mu} = 0$$

$$\left(R_{\mu\nu} - \frac{1}{2}Rg_{\mu\nu} + \Lambda g_{\mu\nu}\right)_{;\mu} = 0$$

does not amount to energy or energy-momentum conservation. Since energy is defined as a scalar quantity that is conserved as a result of the time-translational invariance of the laws of physics, conservation of energy must be defined along timelike vector fields. Killing vector fields are those who satisfy the equation $\xi_{\mu;\nu} + \xi_{\nu;\mu} = 0$, and are the generator of symmetries of the metric. While there are metrics which have such timelike/null Killing fields, the Robertson-Walker metric that arises from the cosmological principle *does not*:

S. W. Hawking and G. F. R. Ellis. *The Large-scale Structure of Space-time*. 1973; and C. W. Misner, K. S. Thorne, and J. A. Wheeler. *Gravitation*. 1973

Table 1.1: Measurements for Λ CDM cosmology by current CMB experiments.[Hinshaw et al., 2013, Planck Collaboration et al., 2015] Other model parameters suppressed for clarity

observers observe nearly isotropic background radiation, then the metric describing the background evolution of the largest scales is the Robertson-Walker metric:

$$ds^2 = -c^2 dt^2 + a^2(t) dl^2, \quad (1.17)$$

where dl is the line element of space, which can be written in *comoving spherical coordinates* as

$$dl^2 = \frac{dr^2}{1 - Kr^2} + r^2 d\theta^2 + r^2 \sin^2 \theta d\phi^2. \quad (1.18)$$

For photons, we can write without loss of generality a radial null geodesic as

$$ds^2 = 0 = -c^2 dt^2 - a^2(t) \frac{dr^2}{1 - kr^2}. \quad (1.19)$$

Now, since the value of Kr^2 can be absorbed into r^2 with a change of coordinates, only 3 special values of K have physical significance, namely $\{0, 1, -1\}$, representing flat, spherical and hyperbolic geometries respectively. These cases will lead to different mathematical analyses as we see in what follows.

Now, as r is a comoving coordinate, the total distance d_c is constant. The total length travelled by the photon can be calculated then as

$$\int_{t_e}^{t_0} \frac{cdt}{a(t)} = \int_0^{d_c} \frac{dr}{\sqrt{1 - kr^2}} = \begin{cases} \arcsin d_c & \text{if}(k = 1), \\ d_c & \text{if}(k = 0), \\ \operatorname{arcsinh} d_c & \text{if}(k = -1). \end{cases} \quad (1.20)$$

where t_e is the time of emission and t_0 is the current age of the universe, in which $a(t_0) = 1$. Since The physical distance between comoving observers is $d = a(t)d_c$, the current distance is equal to the comoving distance - it will be less than that in the past, and greater in the future.

Since the FLRW universe space is not time translation invariant, the photon will not conserve its energy along the path.¹⁰ The wavelength of the photon will be directly proportional to the scale factor: $\lambda_0/\lambda_e = a(t_0)/a(t_e)$ which is usually expressed as the redshift $z = 1/a(t_e) - 1$, which is the measured change in

¹⁰ This is a direct consequence of the Noether's theorem.[Noether, 1918]

frequency divided by the original frequency and can be directly observed from discrete line spectra.

In terms of redshift, the Friedmann equation can be written, by direct substitution of $a \rightarrow 1 + z$ as:

$$\begin{aligned} H(z) &= H_0 \sqrt{\Omega_\Lambda + \Omega_k(1+z)^2 + \Omega_m(1+z)^3 + \Omega_r(1+z)^4} \\ &= H_0 E(z) \end{aligned} \quad (1.21)$$

For a photon emitted at a time t_e and observed at a time t_a the comoving distance between objects at redshifts z_1, z_2 can be written, since $H(z)dt = adz$, as:

$$\begin{aligned} \left. \begin{array}{l} \arcsin d_c \quad , \text{ or} \\ d_c \quad , \text{ or} \\ \operatorname{arcsinh} d_c \end{array} \right\} &= c \int_{t_e}^{t_a} \frac{dt}{a(t)} \\ &= c \int_{z_1}^{z_2} \frac{dz}{H(z)} \\ &= \frac{c}{H_0} \int_{z_1}^{z_2} \frac{dz}{E(z)}, \end{aligned} \quad (1.22)$$

where $d_H = \frac{c}{H_0}$ is called the *Hubble horizon*, or the radius of the Hubble sphere. In terms of Ω_k, H_0 and c , we can write then:

$$d_c(z_1, z_2) = \frac{c}{H_0} \left\{ \begin{array}{l} \frac{1}{\sqrt{\Omega_k}} \sin \left[\sqrt{\Omega_k} d_{c,0}(z_1, z_2) \right] \quad , \text{ or} \\ d_{c,0}(z_1, z_2) \quad , \text{ or} \\ \frac{1}{\sqrt{|\Omega_k|}} \sinh \left[\sqrt{|\Omega_k|} d_{c,0}(z_1, z_2) \right] \end{array} \right. \quad (1.23)$$

Neither physical nor comoving distances can be directly measured, however. To do so, we must rely on standard rulers or standard candles, by using relations that employ either angular distances or the reduction in luminosity of distant objects. In Euclidean space, the relations are $d_A = r/\theta$, for an object of known size r with an angular diameter θ and $d_L = 10^{\frac{m-M}{5}+1}$, for an object of absolute magnitude M and apparent magnitude m with $d_A = d_L = d_c$. However, as a result of the curvature of

space-time, these equalities do not hold in FLRW universes. The angular distance between two different redshifts will be stretched by the relative expansion between them:

$$d_A(z_1, z_2) = d_c(z_1, z_2) \frac{a_2}{a_1} = d_c(z_1, z_2) \frac{1+z_1}{1+z_2}, \quad (1.24)$$

whereas luminosity distance, due to flux conservation, will be related to the angular distance and the comoving distance by [Ellis, 1971]:

$$d_L(0, z) = (1+z)^2 d_A(0, z) = (1+z) d_c, \quad (1.25)$$

which is the *Etherington's reciprocity relation* and is valid for any pseudo-riemannian description of space-time, regardless of the theory of gravity. These measures of distances in cosmology will be necessary to not only determine the distance of clusters and background objects for gravitational lensing latter in this work, but also to calculate absolute magnitudes. Using the luminosity distance, the difference between absolute and apparent magnitude can be written as

$$DM = 5 \log [d_L(z) 10^5 \text{Mpc}^{-1}] \quad (1.26)$$

1.4 *The Big Bang*

The expansion of space, when backwards extrapolated to very early times will lead us to the idea that the universe was once very hot and dense [Dodelson and Efstathiou, 2004]. In fact, one can show that for small enough ρ_Λ , the geodesics of our fluid congruence will be incomplete in the time coordinate, in other words, they cannot be extended beyond a certain proper-time or affine parameter. This is what is called a *time-like singularity* in the past, in which the curvature diverges for all points of space [Hawking and Penrose, 1970].

Either with or without singularities, it is now known that the early universe was dense and hot. The main observations that support this are:

- the Cosmic Microwave Background (CMB) [Smoot, 1999, Hinshaw et al., 2013, Planck Collaboration et al., 2015], which

is the *relic* thermal emission of matter,

- the abundance of primordial elements [Steigman, 2007] created during the first minutes, and
- the observation of the near isotropic recession of distant objects from small to very large redshifts (Hubble's Law) e.g. [Riess et al., 1998].

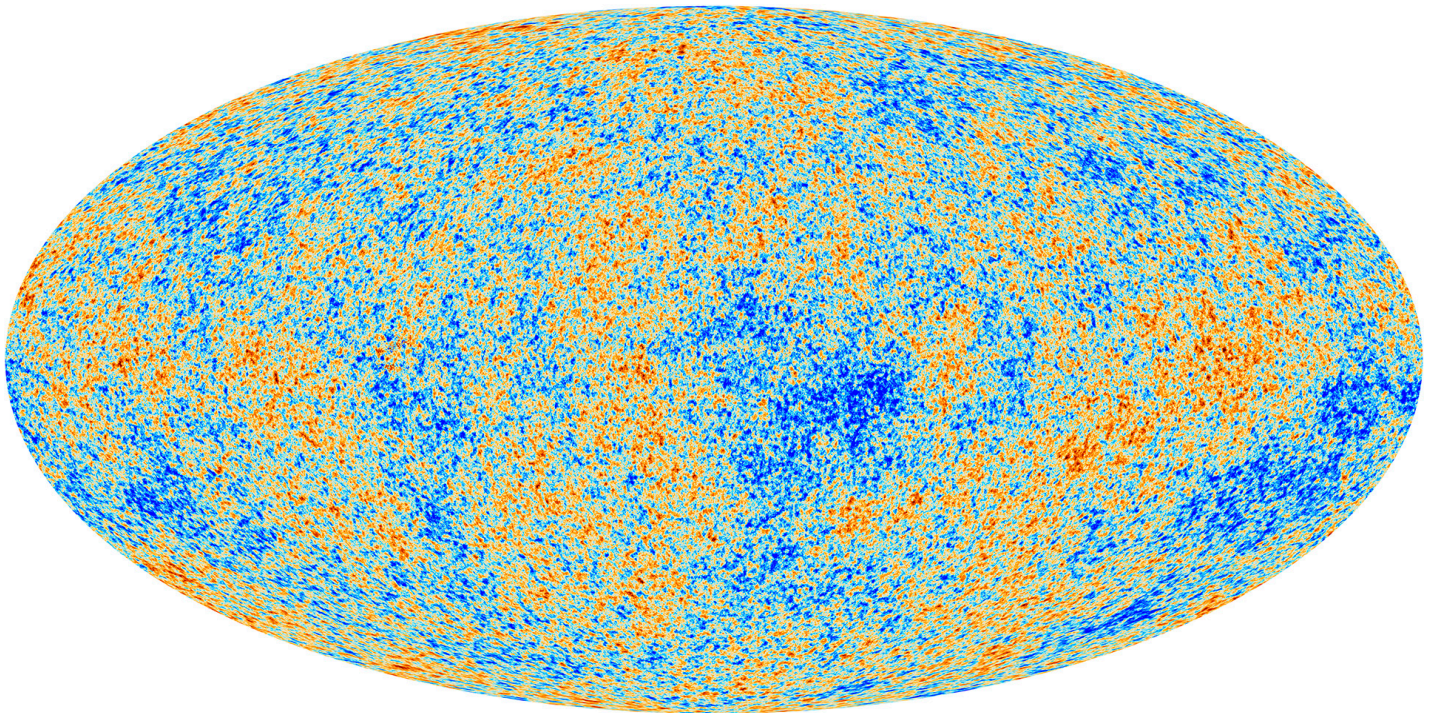


Figure 1.1: The all sky measurements of temperature deviations from the average of the Cosmic Microwave Background [Planck Collaboration et al., 2015].

The earliest phases of the Big Bang are still subject to much speculation. Although the oldest relic from the beginning directly detected is the CMB at redshift $z = 1108$, $t \approx 380000$ years, confidence in ETG allows us to formulate models of evolution of of much earlier times.

In most currently discussed models, the universe begins as homogeneous quantum vacuum. At some point, a phase transition caused the universe to enter an exponentially accelerated expansion. Vacuum fluctuations then, under the rapid change of the underlying potential, became real particles and density fluctuations slightly deviating from the background homogeneity.¹¹

As temperature, density and pressure decreased, the Electromagnetic and Weak interactions decoupled, and baryon physics arose as currently understood in collider experiments.

¹¹ Several processes and most of the underlying physical theory at this point are still poorly understood, but are extensively discussed in literature [Baumann, 2009, Sakharov, 1991].

Further on, at $t = 10^{-4}$ s, quarks condensed into hadrons. Neutrinos decoupled at about 1s and between the first and third minutes from the start, primordial nucleosynthesis created the primordial elements [Alpher et al., 1948]

From the end of the inflation to 10^4 years, the dynamics of the expansion are dominated by radiation content, because the a^{-4} term in the equation explodes. This is the *radiation era* and using the Friedmann equation 1.9 with all other densities being zero, we find that $a \propto \sqrt{t}$. After equipartition ($\Omega_m(t_{eq}) = \Omega_r(t_{eq})$), matter density became the dominant factor and expansion accelerated to $a \propto t^{2/3}$. The mean free path of the photon was small, as they constantly scattered off the free electrons and protons of the hydrogen/helium plasma.

Eventually, the universe cooled to the point that the plasma condensed into neutral atoms, an epoch called *recombination*. Shortly after recombination, the photon mean free path became larger than the Hubble length, and photons travelled freely without interacting with matter. For this reason, recombination is closely associated with the last scattering surface, which is the name for the last time at which the photons in the cosmic microwave background interacted with matter.¹²

¹² these two events are distinct, and in a universe with different values for the baryon-to-photon ratio and matter density, recombination and photon decoupling need not have occurred at the same epoch.[Padmanabhan, 1993]

1.5 Evolution of the Large Scale Structure of the Universe

Small deviations from homogeneity can be studied by assuming a FLRW background and introducing local perturbations to the density field. As in the earliest times, Ω_Λ is negligible, we consider $\Lambda = 0$ for now. Deviations of a global average density can be written as

$$1 + \delta(\vec{x}) = \frac{\rho(\vec{x})}{\bar{\rho}}, \quad (1.27)$$

where δ is called the *density contrast* with respect to the background average density $\bar{\rho}$. For now, we will consider linear perturbation, in which $\delta \ll 1$. Let us start with a simple case. A region with an overdensity $\delta(\vec{x})$ of radius $r < d_H$, in an otherwise flat Λ CDM background, has a deviation in expansion

of $\theta = 3H \rightarrow 3H + \delta\theta$. During matter domination and using energy conservation 1.8 and the Raychaudhuri equation 1.6 for dark matter only, as in the acceleration equation 1.7, leads to the background equations at zeroth order and at first order to:

$$\begin{aligned}\dot{\delta} + \delta\theta &= 0, \\ \delta\dot{\theta} + 2H\delta\theta &= -4\pi G\bar{\rho}\delta.\end{aligned}$$

Eliminating $\delta\theta$ we have then:

$$\ddot{\delta} + 2H\dot{\delta} - 4\pi G\bar{\rho}_m\delta = 0, \quad (1.28)$$

which is an equation that governs the evolution of local matter overdensities δ with background density $\bar{\rho}$.

The introduction of perturbations directly to the equations of motion as such is not actually compatible with ETG, but only with the Newtonian limit [Ellis et al., 2012]. That this Newtonian approximation works can be deceptively simple because its validity depends on certain gauge issues (or, more precisely, on our ability to write gauge-invariant gravitational potentials [Bardeen, 1980] in ETG, which are presented in clear form by Peacock [2003] in its section 1.2. Rigorous approaches can be read on Ellis et al. [2012] or Dodelson and Efstathiou [2004]

To work out some simple results, let us examine equation 1.28 by introducing the definition of Ω_m so that we have

$$\ddot{\delta} + 2H\dot{\delta} - \frac{3}{2}\Omega_m H^2\delta = 0. \quad (1.29)$$

Using the scale factor for a matter-dominated universe, this equation can be solved to $\delta(t) = \delta_+ t^{2/3} + \delta_- t^{-1}$ where $\delta_+ t^{2/3}$ is called the *growing mode*, since the density contrast with it grows with time (and eventually, collapses into visible structures). The evolution of the density perturbations can be written by a separation of variables as

$$\delta(\vec{x}, t) = D_+(t)\delta(\vec{x}, 0) \quad (1.30)$$

where D_+ is called the *Growth Function* and is given, in the matter dominated era, as a function of the scale factor a

by [Dodelson and Efstathiou, 2004]

$$D_+(a) \propto H(a) \int_0^a \frac{da'}{(a'H(a'))^3} \quad (1.31)$$

and can be used normalised to $D_+(1) = 1$ for practical purposes. To account for radiation, which is not dominant after equipartition but still relevant before recombination, the argument can be completed with a change of variables from t to $y = a/a_{eq}$, which together with the Friedmann equation gives us the *Mészáros equation* [Meszaros, 1974, Dodelson and Efstathiou, 2004]:

$$\delta'' + \frac{2+3y}{2y(1+y)}\delta' - \frac{3}{2y(1+y)}\delta = 0. \quad (1.32)$$

This equation has two closed analytic solutions, the growing mode of which is $\delta(y) = y + 2/3$. Another mode is dominant if $y \ll 1$, which is $\delta \propto \ln y$. In this case, which we can extend to full radiation dominated era, and the latency in response of the density contrast due to the rapid expansion is called the *Mészáros effect* [Peacock, 2003] - a large overdensity (with size greater than d_H) that had been growing, enters the Hubble horizon and becomes nearly frozen (growing only logarithmically) before matter domination arrives.

Table 1.2: Sub-horizon sized matter overdensities evolution with time in different epochs.

Era	Ω	$H(t)$	$\delta(t)$
Radiation	$\Omega_m, \Omega_\Lambda \approx 0$	$\frac{1}{2t}$	$C_1 \ln t$
Matter	$\Omega_r, \Omega_\Lambda \approx 0$	$\frac{2}{3t}$	$C_+ t^{2/3} + C_- t^{-1}$
Λ	$\Omega_m, \Omega_r \approx 0$	$\sqrt{\frac{\Lambda}{3}}$	$C_1 + C_2 e^{-2\sqrt{\frac{\Lambda}{3}}t}$

For modes larger than the horizon d_H , Newtonian approximation breaks down, and we have to return to the full field equations. There are many ways to define covariant potentials, analogues to the Newtonian potential Φ . Following the path of Dodelson and Efstathiou [2004] we can write:

$$3H \left(\dot{\Phi} + H\Phi \right) = 4\pi G a^2 \rho_m \delta \left[1 + \frac{4}{3y} \right]. \quad (1.33)$$

This equation can be solved in the potentials and yields constant solutions for either matter domination or radiation domination,

the latter being up to 10 times greater than the first [Dodelson and Efstathiou, 2004]. In both cases, using known relations for H and ρ we arrive at $\delta \propto a^2$ for $a \ll a_{eq}$ and $\delta \propto a$ for $a_{eq} \ll a$. In essence, this shows that large modes will always grow.

Finally, to consider the effect of baryons - which are only relevant in sub-horizon evolution, since collisional effects are local, equation 1.28 must be changed to include pressure. This will result in

$$\ddot{\delta} + 2H\dot{\delta} + (c_s^2\nabla^2 - 4\pi G\bar{\rho}_m)\delta = 0. \quad (1.34)$$

where $c_s = \sqrt{\partial p / \partial \rho}$ is the *sound speed* of the baryon fluid. This equation can be understood classically as $\ddot{\delta} - [\text{Pressure} - \text{Gravity}]\delta = 0$, which is Newton's 2nd Law. The solutions for equation 1.34 will depend on a particular scale, since the gravitational forces of small overdensities cannot overcome the pressure of the baryons. This is the *Jeans Length* and is expressed as:

$$\lambda_j = c_s \sqrt{\frac{\pi}{G\rho}} \quad (1.35)$$

For a $\lambda > \lambda_j$ the structure will collapse, otherwise it oscillates due to pressure.

1.6 *The Role of Galaxies in Cosmology*

At the end of the first stages of cosmic evolution, the inhomogeneities contain the information that will shape the observed large scale structure of the universe. This structure is mostly isotropic and homogeneous in the largest scales, but its configuration displays measurable statistical properties that can be observed in the CMB, galaxy positions and clustering. It is clear then that assessing this statistical information offers knowledge about not only the objects themselves but about the universe and the physical laws on the whole [Weinberg et al., 2013].

The universe we see at night, on the other hand, displays a rich structure (Fig: 1.2), with field galaxies, groups, clusters and super-clusters of galaxies, filaments and large empty voids. To compare these observational results with the theory we use statistical

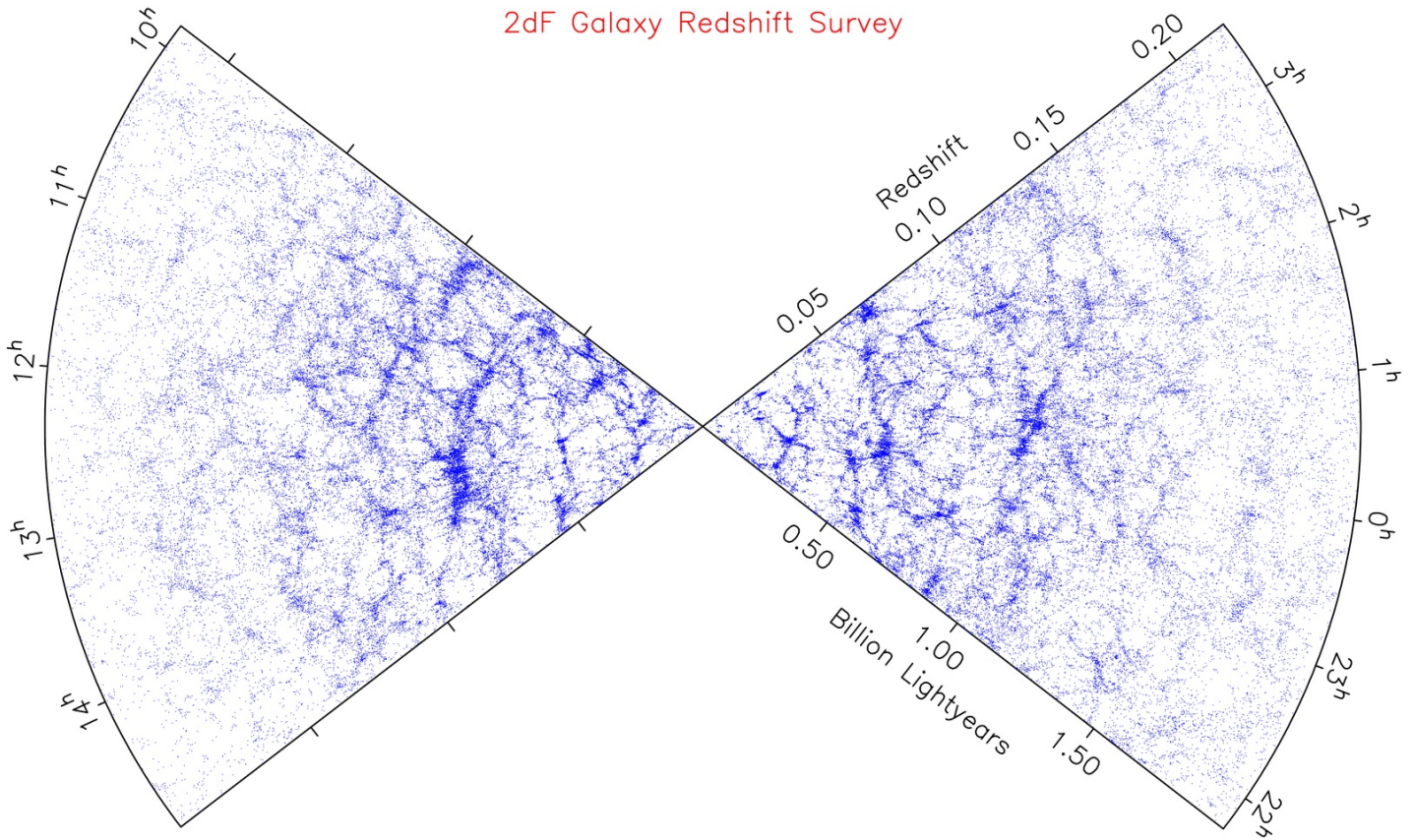


Figure 1.2: Distribution of galaxies of the 2dF Galaxy Survey [Colless et al., 2001].

methods over populations of features in observations, such as preferred scales in the CMB map, or number counts per interval of cluster mass, among others [Weinberg et al., 2013, Lima and Hu, 2005]. To make sense from the theory to observations, simulations, even though based in Newtonian physics and approximations for finite volumes, have been very successful to reproduce these statistical features of the large scales [Springel et al., 2005, Vogelsberger et al., 2014, Klypin et al., 2011].¹³

¹³ Simulations are, in essence, methods for solving the differential equations to calculate the theoretical predictions.

Usually, one starts with the full-version perturbed EFEs together with the Boltzmann equation for the evolution of the fluids up to a certain redshift. Setting the initial conditions is problematic, since current models based on ETG will definitely fail when energy density reaches Planck-scale levels (about $t = 10^{-43}$). In these so called *Einstein-Boltzmann solver* codes, such as CAMB [Lewis and Challinor, 2002] one sets initial conditions after Inflation, using well-grounded assumptions.

The statistics of the density field is encoded by n -point

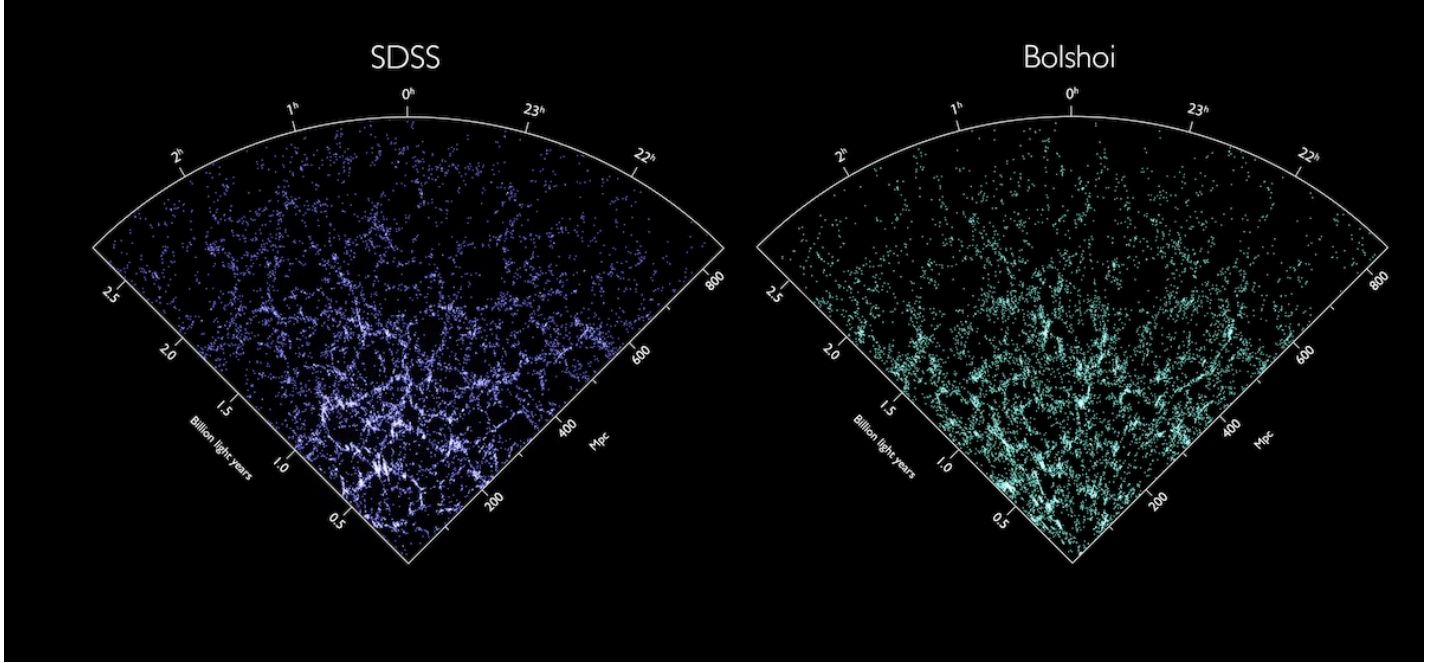


Figure 1.3: A comparison between the Bolshoi simulation and SDSS observation of the nearby universe. Sources: *Nina McCurdy/University of California, Santa Cruz; Ralf Käbberle and Risa Wechsler/Stanford University; Sloan Digital Sky Survey; Michael Bush/University of Zurich*

correlation functions.

$$\xi(r) = \langle \delta(\vec{x})\delta(\vec{x} + \vec{r}) \rangle \quad (1.36)$$

where $\xi(r)$ depends only on the distance between two points due to the statistical homogeneity and isotropy.

The density contrast can be written as an inverse Fourier transform

$$\delta(x) = \int \frac{d^3k}{(2\pi)^3} \tilde{\delta}(k) e^{i\vec{k}\cdot\vec{x}} \quad (1.37)$$

So defining the *power spectrum*¹⁴ as

$$\langle \tilde{\delta}(\vec{k})\tilde{\delta}^*(\vec{k}') \rangle := (2\pi)^3 \delta_D^3(\vec{k} - \vec{k}') P(k) \quad (1.39)$$

where δ_D^3 is the *Dirac distribution*, we can write the two-point correlation function as the Fourier transform of the power spectrum

$$\begin{aligned} \xi(r) &= \int \frac{d^3k}{(2\pi)^3} P(k) e^{i\vec{k}\cdot\vec{r}} \\ &= \frac{1}{2\pi^2} \int dk k^2 P(kr) \frac{\sin(kr)}{kr} \end{aligned} \quad (1.40)$$

The most appealing reason to write the quantities in terms of Fourier space variables is that due to translational invariance

¹⁴ It is also usual to define also the dimensionless quantity

$$\Delta_k^2 := \frac{k^3 P(k)}{2\pi^2} \quad (1.38)$$

which measures power per logarithmic scale.

(which follows from homogeneity) we characterise the statistics of random fields as preferred scales, which readily show up in power spectra.

Up to now, we have seen how the universe evolves and how this stage is set for galaxies and galaxy clusters to act. It is then time to move to non-linear scales of evolution¹⁵, where both simplified models [Peebles, 1984, Zel'dovich, 1970] and simulations [Kravtsov and Borgani, 2012] can be used, usually providing complementary insights to understand the evolution of the large scale structure. This final stage of collapse and formation of structures will be studied in the next chapter, as it closely relates to the dynamics and observables of galaxy systems, which is most important to our application in this work.

¹⁵ which is characterised by $\Delta_k > 1$

Dynamics and Properties of Galaxy Systems

THE PHYSICAL PROPERTIES OF GALAXY SYSTEMS are, because of their complex configurations not only difficult to resolve, but also convoluted. More than being an assemble of "particle galaxies" bound by gravitational interactions, member galaxies play an intricate dance, exchanging both matter content and energy, with multiple mergers of galaxies at the centre and accretion of other nearby formed associations. Feedback due to collisional processes of baryonic matter and other nonlinear physical processes, also contribute, with the gas and the star-formation also playing significant roles on final observables¹. It is crucial to understand the relationships implicated by these behaviours to correctly understand the landscape of galaxy system observables and therefore we proceed first into their formation history directly from the previous chapter, and then, on to discuss the role of the large-scale structure in their configurations. To the end of this chapter, we assess the multiple probes of cluster and group physics to place this work relative to the framework of extragalactic astronomy and cosmology.

¹ P. Schneider. *Extragalactic Astronomy and Cosmology*. 2006

2.1 From Overdensities to Groups and Clusters

The linear theory of evolution of density perturbation breaks down after at some point. We are then forced into using simpler models for nonlinear evolution or, concomitantly, numerical simulations [Kravtsov and Borgani, 2012]. Despite its apparent oversimplification, an overdense sphere will is a very useful model,

which behaves as a small closed universe with a modified matter density due to the initial perturbation. Here, there is no need for this perturbation to be uniform, as the Poisson's equation guarantees that the evolution of any spherically symmetric perturbation is the same [Peacock, 2003].

Far into the matter-dominated era, an overdense region can be described then by a Friedman equation with a different, enhanced local density, so that we can parametrise the solution by its proper radius and time as functions of the development angle $\phi = H_0 \eta \sqrt{\Omega_m - 1}$, where η is the conformal time as [Gunn and Gott, 1972]:

$$\begin{aligned} t(\phi) &= A(1 - \cos \phi) \\ r(\phi) &= B(\phi - \sin \phi), \end{aligned} \quad (2.1)$$

in which A and B are connected by $A^3 = GMB^2$. Expanding these relations to fifth order in ϕ gives $r(t)$ for small t as²:

$$r(t) \approx \frac{A}{2} \left(\frac{6t}{B} \right)^{\frac{2}{3}} \left[1 - \frac{1}{20} \left(\frac{6t}{B} \right)^{\frac{2}{3}} \right]. \quad (2.2)$$

Then, the density perturbation within the sphere will be

$$\delta \approx \frac{3}{20} \left(\frac{6t}{B} \right)^{\frac{2}{3}}. \quad (2.3)$$

Now we can examine the properties of the solution by looking at solutions with particular values for ϕ :

- if $\phi = \pi$, the radius is at maximum, and the overdensity detaches itself from the background evolution and turns around to collapse. At this point, the density contrast is $\delta_{tr} = 9\pi^2/16 \approx 5.55$. Using just linear theory, we would find that $\delta_{tr,lin} \approx 1.06$,
- at $\phi = 2\pi$, $r = 0$, which is an idealisation of collapse. This occurs when $\delta_{col,lin} = (3/20)(12\pi)^{2/3} \approx 1.686$.

This idealisation, however, differs substantially from reality as dissipation will act and convert the kinetic energy of collapse into random motion. By using the virial theorem, we can postulate an equilibrium at $r_{vir} = r_{tr}/2$, which occurs at $\phi = 3\pi/2$. By this

² it is not surprising that, at leading order $r \propto t^{2/3}$, which is just Einstein de-Sitter universe, where $r \propto a \propto t^{2/3}$

time, the density will have increased by a factor of 2^3 while the background density will have decreased by a factor of 2^2 , since $\rho \propto a^{-3}$ and $a \propto t^{2/3}$. The overdensity in the region will be

$$\frac{\rho}{\bar{\rho}} = 1 + \delta_{vir} = 1 + \delta_{tr} \times 8 \times 4 \approx 178. \quad (2.4)$$

As a conservative threshold, a higher density contrast of $\Delta_c = 200$ is defined as the region inside collapsed systems. This defines a truncation radius and the enclosed mass of a collapsed region as

$$r_{200} = \left(\frac{3M_{200}}{4\pi\Delta_c\bar{\rho}_m} \right)^{1/3}. \quad (2.5)$$

Although the $\Delta_c \approx 178$ is a physically derived relation, the self-similarity of the matter density profile makes the radius definition somewhat arbitrary. By including the full Λ CDM it has been shown that a more physically meaningful radius for virialised systems is the one which has a contrast of $\Delta_c \sim 330$, which is smaller than the r_{200} defined by $\Delta_c = 200$. Since most literature still uses 200, it is useful to maintain it for comparing results, although transformations are pretty straightforward [Johnston et al., 2007].

2.2 The Role of Cosmology in Galaxy Systems

After the collapse, overdense regions tend asymptotically to virial equilibrium, due to increase in entropy by dissipation. Smaller objects form first and can merge into larger objects, that again, if left undisturbed, tend to virialise. This characterises what is called the *hierarchical scenario* of structure evolution [Peebles, 1984]. Despite this complex landscape, dark matter particle simulations have been shown to display a characteristic shape (fig 2.1) for radial matter density distributions characterised by the logarithmic slope steepening with increasing radius (e.g. Navarro et al. [1996], Dubinski and Carlberg [1991]).

The density profiles obtained from simulations can be parametrised in a variety of ways, one of the most commonly of which is the *NFW profile*, given by:

$$\rho_{NFW}(r) = \frac{4\rho_s}{x(1+x)^2}, \quad x = r/r_s, \quad (2.6)$$

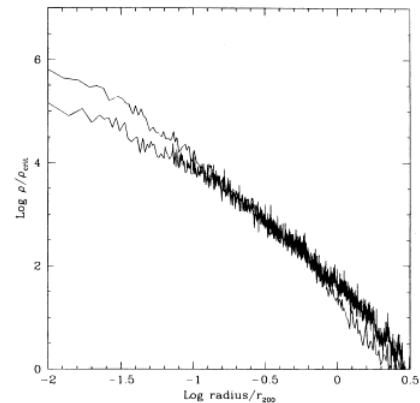


Figure 2.1: Results from simulations showing the characteristic steepening slope of dark matter density profiles. Source: Navarro et al. [1996]

³ Other commonly listed profiles are the Einasto profile, given by:

$$\rho_E(r) = \rho_s \exp \left[\frac{2}{\alpha} (1 - x^\alpha) \right], \quad x = r/r_s.$$

and the BMO[Baltz et al., 2009] profile, a modification of the NFW profile that incorporates a polynomial, smooth, truncation in outer regions

$$\rho_{BMO}(r) = \frac{4\rho_s}{x(1+x)^2} \left(\frac{y^2}{1+y^2} \right)^n,$$

where $y = r/r_t$ is a new truncation radius parameter and n is another truncation parameter. This is not even remotely an inclusive list of profile parametrisations, as there are many others.

where r_s is the characteristic radius, where the logarithm slope of the radial density curve changes from -2 to -3 at a given scale radius.³

The self-similar shape of radial density profiles has proven to be very general, being virtually independent of the shape of the power spectrum and background cosmology [Katz, 1991, Navarro et al., 1997], a feature usually called *universality*. However, a derivation from physical principles of this universal shape is still an open problem.

The universality of density profiles suggests that a useful tool to study the matter distribution in the universe is to substitute the nearly smooth field of densities (or equivalently, density contrasts) by a collection of individual *dark matter halos*. In this ansatz, these halos contain *all* matter, and therefore the density distribution is represented by an interpolation of halos scattered throughout space [Cooray and Sheth, 2002]. This substitution from matter distribution to halos is depicted in figure 2.2.

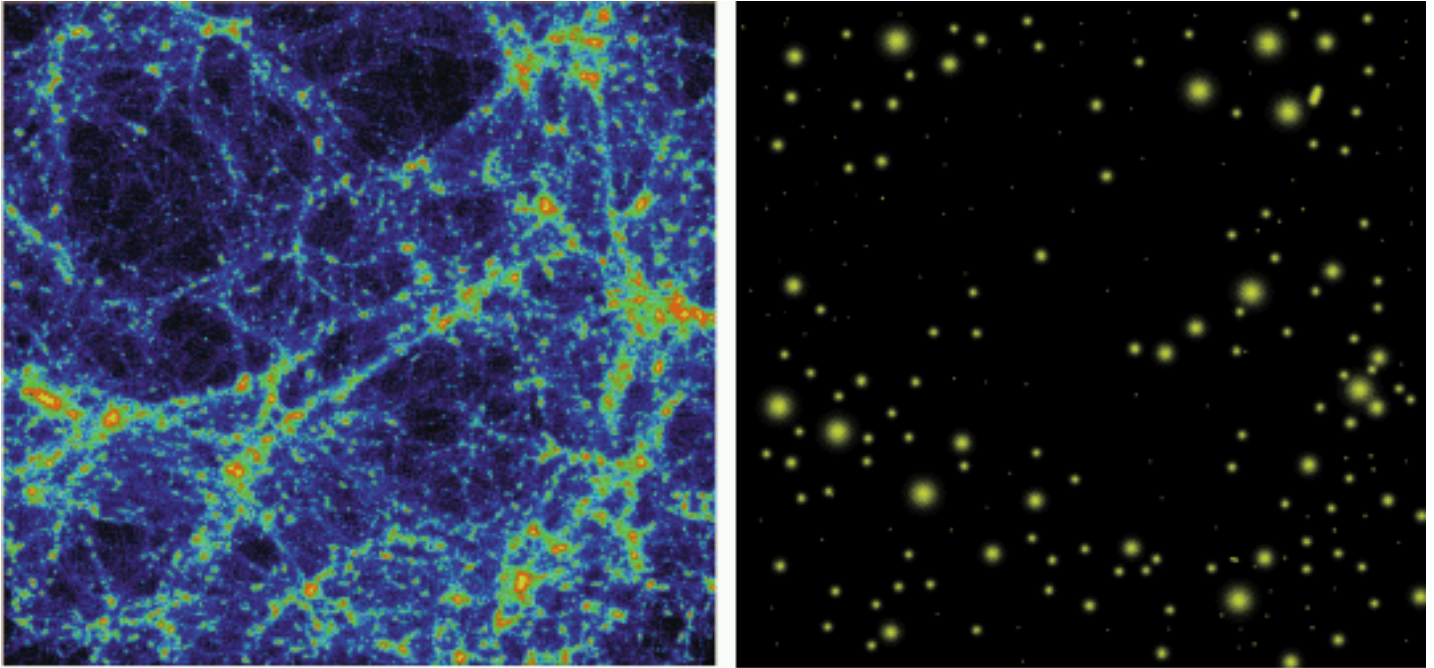


Figure 2.2: The complex, smooth, distribution of matter after the growth of structure in the universe can be understood as an interpolation of spherically collapsed halos. Source: Cooray and Sheth [2002]

To characterise particular cosmological models then, either simulations or simple models can be used to derive a prediction for the number density of collapsed halos of mass in an interval $[M, M + dM]$. This is called the *mass function*, and is one of the central probes of cosmology [Weinberg et al., 2013]. The mass

function is important not only to investigate cosmological models, as it is more sensitive than background evolution [Lima and Hu, 2005], but also important to quantify effects of the large scale structure in the neighbourhood⁴ of clusters, as we will see towards the end of this section.

⁴ Scales from $\sim 1\text{Mpc}/h$ to $\sim 10\text{Mpc}/h$

As a first ingredient to the mass function, we must define the variance of the linear density contrast to our collapse threshold δ_c in order to quantify the fraction of collapsed halos per mass. For a given density contrast field $\delta(\vec{x})$ we can filter to halos using a window function $W(\vec{x}, R)$, normalised to unity to get a smoothed field

$$\delta(\vec{x}; R) = \int \delta W(\vec{x} + \vec{x}'; R) d^3x'. \quad (2.7)$$

This filter defines an enclosed mass $M := c_f \bar{\rho} R^3$ where c_f is some constant used to normalise the filter. Now, in Fourier space this convolution integral becomes a product $\delta(k; R) = \delta(k) \tilde{W}(kR)$. Using then a top hat model for the filter, we can write the filtered variance of the field as a function of filter radius R as

$$\sigma_R^2 = \overbrace{\langle \delta^2(\vec{x}; R) \rangle}^{\propto \xi(R)} = \frac{1}{2\pi^2} \int_0^\infty dk k^2 P(k) \left| \tilde{W}(\vec{k}, R) \right|^2, \quad (2.8)$$

where now \tilde{W} is specifically the transform of the top hat function.⁵

If we then transform the into a mass scale by

$$R = \left(\frac{3M}{4\pi\rho_c} \right)^{1/3}, \quad (2.10)$$

where $\rho_c = \bar{\rho}_m \delta_c$ is the density of the collapsed halo we can use the mass variance $\sigma^2(M)$ to calculate the mass function as a function of density peak height relative to the variance $\nu = \delta_c/\sigma(M)$. The first statistical model for mass function was developed by Press and Schechter [1974], in which the main underlying idea is that the probability that $\delta_M > \delta_c$ at a given time is the equal to the fraction of mass contained in halos with mass greater than M at that time. Using that the distribution

⁵

$$\begin{aligned} \tilde{W}(\vec{k}, R) &= \int_{\mathbb{R}} d^3x W(x, R) e^{-i\vec{k}\cdot\vec{x}} \\ \tilde{W}(\vec{k}, R) &= \frac{3}{(kR)^3} [\sin(kR) - (kR) \cos(kR)] \end{aligned} \quad (2.9)$$

of density perturbations is a Gaussian random field, the fraction of fluctuations above the threshold δ_c correspond to collapsed regions and is given by

$$F(M) = \frac{1}{\sqrt{2\pi}\sigma(M)} \int_{\delta_c}^{\infty} d\delta \exp\left[-\frac{\delta^2}{2\sigma^2(M)}\right] = \frac{1}{2} \operatorname{erfc}\left[\frac{\nu^2}{2}\right], \quad (2.11)$$

where $\operatorname{erfc}(x) = 1 - \operatorname{erf}(x)$ is the complementary error function.

This result is, however, problematic. Since $\lim_{x \rightarrow 0} \operatorname{erfc}(x) = 1$ and $\lim_{x \rightarrow \infty} \operatorname{erfc}(x) = 0$, this model predicts that never more than $1/2$ of all matter in the universe is inside collapsed regions. The fraction of dark matter in halos above M then must be multiplied by an additional "fudge factor" of 2 in order to ensure that every particle ends up as part of some halo with $M > 0$. This is because underdense regions can be enclosed within larger overdense regions, giving them a finite probability of being included in some larger collapsed object.

Now, the number of halos with masses in the range $[M, M + dM]$ per comoving volume at a time t $n(M, t)$ can be written as

$$n(M, t) = \frac{dn}{dM} = M \frac{dn}{d \ln M} \quad (2.12)$$

Using the formalism idea that $\frac{\partial F}{\partial M} dM$ is equal to the fraction of mass locked up in halos with masses in the range $[M, M + dM]$ we find that

$$n(M, t) dM = \frac{\bar{\rho}}{M} \frac{\partial F}{\partial M} dM \quad (2.13)$$

$$= \underbrace{\frac{\bar{\rho}_m}{2}}_{\text{fudge}} \frac{\partial}{\partial M} \frac{1}{2} \operatorname{erfc}\left[\frac{\nu^2}{2}\right] dM \quad (2.14)$$

$$= \sqrt{\frac{2}{\pi}} \frac{\bar{\rho}_m}{M^2} \nu \exp\left[-\frac{\nu^2}{2}\right] \left| \frac{d \ln \sigma_M^{-1}}{d \ln M} \right| dM, \quad (2.15)$$

which is the PS mass function.

If we rewrite the mass function as

$$\frac{dn}{d \ln M} = \frac{\bar{\rho}_m}{M} \frac{d \ln \sigma^{-1}}{d \ln M} f(\nu), \quad (2.16)$$

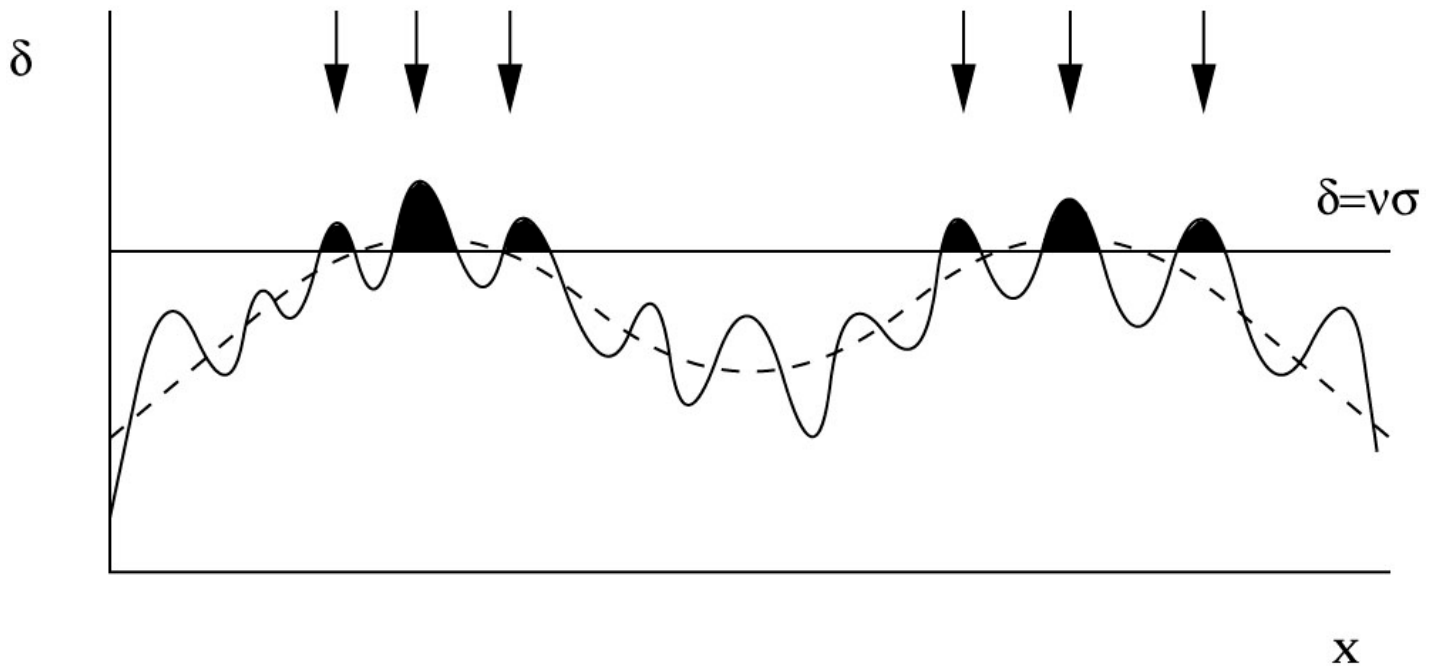
we can recognise that the *multiplicity function* $f(\nu) = \sqrt{2/\pi\nu}e^{-\nu^2/2}$ encodes the characteristic shape of the Press-Schechter mass function.

Further advancements have been made since this first model and today, numerical simulations give us accurate estimates for mass functions from specific cosmological models, using the original PS multiplicity function as a guide for creating parametric functions which are then fitted to the simulations results, which can in turn be compared to cluster counting in surveys [Tinker et al., 2008] to test new cosmological models. ⁶

The relationship between the density of collapsed halos is not equivalent to the density distribution of matter, however. As it can be seen in figure 2.3, the so called *long-wavelength modes* of the density distribution interfere in spatial location, providing a higher local average $\bar{\rho}_m$ and thus enhancing the density of halos with respect to the density of matter. For that reason, collapsed objects, be them galaxies, groups or clusters, are *biased* tracers of the underlying matter distribution. In regions with a higher count of objects, the underlying matter density distribution will have a higher value than expected by a simple proportion as $\delta_m \propto \delta_h$ would suggest. This can be understood under the *peak-background split*, which we develop succinctly below.

⁶ The Tinker mass function, which will be used in this work, is parametrised as

$$f(\sigma) = A \left[\left(\frac{\sigma}{b} \right)^{-a} + 1 \right] e^{-c/\sigma^2}. \tag{2.17}$$



At first order, we expect that this *bias* in measuring mass

Figure 2.3: Regions with higher density due to long modes tend to form more collapsed structures due to a higher local average density, which influences the mass distribution around clusters. Source: Peacock [2003]

distribution due to a particular tracer is a linear function related to the height of the peak of the collapsed density perturbation [Cooray and Sheth, 2002].

For halos, if δ_h is the contrast of halo density⁷ in a small region, then:

⁷ Formally, δ_h is the density contrast of collapsed halos of mass m at redshift z_1 given a mass M in a comoving volume V at a redshift z_0 and is defined by

$$\delta_h(m, z_1 | M, V, z_0) := \frac{N(m, z_1 | M, V, z_0)}{n(m, z_1)V} - 1. \quad \delta_m = b_h(\nu)\delta_h. \quad (2.18)$$

A range with a higher local average density can be understood as a perturbation such that the local collapse overdensity is reduced as $\delta'_c = \delta_c - \epsilon$ so that now $\nu = \delta'/\sigma_M$. If we then expand the perturbed mass function 2.16 in a power series of ϵ we will have the number density modulated by

$$f' = f - \frac{df}{d\delta_c}\epsilon, \quad (2.19)$$

so that the bias will be directly related to the mass function as

$$b(\nu) = 1 - \frac{1}{\delta_c} \frac{d \ln f}{d \ln \nu}, \quad (2.20)$$

Finally, from simulations for the Tinker mass function, large scale bias is parametrised as

$$1 - A \frac{\nu^a}{\nu^a + \delta_c^a} + B\nu^b + C\nu^c, \quad (2.21)$$

where the values A, a, B, b, C , and c are given by table 2.1.

Table 2.1: Parameters of the bias equation as a function of $y = \log(\Delta)$

Param.	
A	$1 + 0.24y \exp[-(4/y)^4]$
a	$0.44y - 0.88$
B	0.183
b	1.5
C	$0.019 + 0.107y + 0.19 \exp[-(4/y)^4]$
c	2.4

Now we can finally estimate the effect of clustering in distorting the cluster mass radial profile due to presence of neighbouring overdense regions. To do so, we first define the halo-mass correlation function as

$$\xi_{hm}(r, M, z) := \langle \delta_h(x)\delta_m(x+r) \rangle, \quad (2.22)$$

that quantifies the excess matter density relative to the background at a distance r from the centre of a halo of mass M at a redshift z . Its natural estimator will be given then by

$$\xi_{hm}(r, M, z) = \frac{\overbrace{\rho_{1h}(r, M, z)}^{\rho_{NFW}}}{\bar{\rho}_m} + b^L(M, z)\xi_{mm}^L(r, z), \quad (2.23)$$

where we label b^L and ξ^L the linear bias and the linear mass correlation function.

The projected mass density due to the halo and the large scale structure can now be written as

$$\begin{aligned} \Sigma(r|M, z) &= \int dz \delta\rho = \int dz \bar{\rho}_m \xi_{hm}(r, M, z) \\ &= \int dz \rho_{1h} + \bar{\rho}_m b^L(M, z) \xi^L(r, z) \\ &= \Sigma_{1h}(r) + \Sigma_{2h}(r) \end{aligned} \quad (2.24)$$

where ρ_{1h} is the cluster profile own profile, called the 1-halo term and $\rho_{2h} = \bar{\rho}_M b^L(M, z) \xi^L(r, z)$ is the 2-halo term, that is, the contribution to the profile due to neighbouring halos.

2.3 The Environment of Galaxy Systems

The environment inside clusters and groups of galaxies differ substantially from the rest of the universe and that results in measurable effects not only on the aspects and types of galaxies that populate these overdense regions, but also on the dynamics of interactions between their contents. One first clear example of these effects is that the mixture of galaxy types inside of clusters is visibly different from the field: whereas about 70% of the galaxies are spirals in the field, clusters are dominated by ellipticals (Fig. 2.4).

We then turn our attention some aspects that determine the content and dynamics of galaxy clusters and groups, to help us understand their nature and then proceed to rank their observable quantities.

Galaxy clusters and groups are composed of matter in densities from 50 to 200 the average density of the universe. They have

For most of this section, we follow arguments from:

P. Schneider. *Extragalactic Astronomy and Cosmology*. 2006

Figure 2.4: The galaxy cluster Abell 2218 as imaged by Hubble, provides a display of the characteristic image of the environment of galaxy clusters, as well as their effect not only in the environment, but, as we will later see, on the images of background galaxies. The yellowish hue of elliptical galaxies and a dominant cD central galaxy shows how the galaxy population of galaxy clusters stand apart from that of galaxies of the field. The thin, distorted arcs are gravitationally lensed images of background galaxies, that we will see in [chapter 3](#). *Source: Image Credit: NASA, ESA, and Johan Richard (Caltech, USA)*



masses ranging from $10^{13}M_{\odot}$ to $10^{15}M_{\odot}$ and typical radii of around $1\text{Mpc}/h$. Most of their matter content can be divided into of 3 different components:

- galaxies, which, by comparing their luminosities and the typical star populations, can only account for a tiny fraction ($\sim 3\%$) of the mass, but are one of the main probes of the mass distribution, as they are expected to follow overall density, and are readily visible to ground-based telescopes in optical.
- intracluster medium (ICM), composed mostly of a diffuse plasma spread throughout the clusters, with very high temperature (in the range between 10^7 and 10^8K) and densities of the order of 10^{-3} particles/ cm^3 . The ICM is detected by X-ray thermal brehmsstrahlung emissions or by inverse Compton scattering of the Cosmic Background Radiation, which is called *Sunyaev-Zel'dovich* Effect (more on the next chapter).
- dark matter, which is indirectly inferred by the amount of mass

measured that cannot be accounted for with stars and the ICM and accounts for 80–85% of the total, and can be quantified by methods that investigate total mass through gravitational effects.

As clusters virialise they tend to appear more spherically symmetric and to have higher number densities of galaxies towards their centres. In these more *relaxed* clusters, the velocities of galaxies around the centre of mass commonly display a dispersion consistent to an isothermal distribution. In principle, this indicates that clusters may have relaxed thermodynamically. This, however, cannot be true, since two-body collisions of galaxies inside clusters have negligible dynamical impact, since the interaction time of the collision is small, due to the high velocity of the galaxies. However, Lynden-Bell [1967] demonstrated that large amplitude fluctuations in the gravitational field, as in galaxy formation or collisions, *can* drive a *quasi-relaxation* process that is much faster than the two-body relaxation time.⁸ Once the collapse of a cluster is complete, however, violent relaxation becomes ineffective, and the process must continue only through two-body interactions.

In another important effect shaping cluster environments, Chandrasekhar [1943] showed that massive objects moving through a distribution of lighter objects will be dragged by an alignment of these smaller ones behind it. This alignment, in its turn, takes place exactly because the larger object pulled (See Fig. 2.5) Originally thought on the case of stars, this is readily applicable to cluster galaxies, and can be roughly expressed as

$$\frac{d\vec{v}}{dt} \propto -\frac{M\rho\vec{v}}{|\vec{v}|^3}. \quad (2.27)$$

This effect is named *dynamical friction*. Being proportional to the mass, it is thought to cause galaxies plunge inwards, with more massive galaxies sinking into the cluster centre.

The observed galaxies in clusters and groups are strongly correlated in colour. In colour-magnitude diagrams, they will appear in a nearly horizontal line, called the *red sequence*. This red sequence is populated by the elliptic galaxies, displaying a very small scatter, and being very similar for every cluster at a given redshift. The red sequence is a powerful tool to identify cluster

⁸ This *violent relaxation* time is given as

$$t_{VR} = \sqrt{\left\langle \frac{\varepsilon^2}{(d\varepsilon/dt)^2} \right\rangle} \quad (2.25)$$

where ε is the energy per unit mass of the system. Using the virial relation, it can be shown that this time is of the order of the crossing time $t_{RV} \approx t_{cross} \approx 1/\sqrt{GR}$, unlike in the case of two-body relaxation, where

$$t_{relax} = t_{cross} \frac{N}{\ln N} \quad (2.26)$$

which is much larger than the age of the universe.

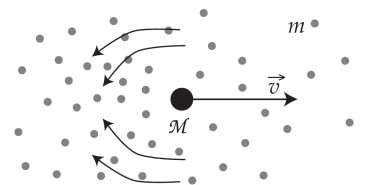


Figure 2.5: The principle of dynamical friction. The gravitational field of a galaxy of mass \mathcal{M} and velocity \vec{v} accelerates other smaller galaxies to its track, which then act as a force pulling the massive galaxy backwards. Source: [Ljima Neto, 2014]

of galaxies because it is generally easier to measure colours than redshifts of galaxies to assess their clustering. In addition, it can be used to constrain the redshift of the cluster, as used in [Rykoff et al., 2014] a red-sequence based cluster finding algorithm that is used in this work, and will be explained in chapter 4.

Regular galaxy clusters also have very bright central galaxies, normally called *Brightest Cluster Galaxies*, but here referred to as central galaxies (CG) only, since we will have central galaxies that are not the brightest in the system. Many of these central galaxies are cD-type galaxies, giant elliptic galaxies that differ from the rest of the elliptic population in several aspects. They have very extended stellar envelopes, that may exceed $R \sim 100h\text{kpc}$ and have broader luminosity profiles. Many (from a fourth to half) cD galaxies have multiple cores, which indicate recent merging of other galaxies, in what is fancifully called *galactic cannibalism* [Dubinski, 1998].

They also have larger axes roughly aligned to the same direction of the overall galaxy distribution in the cluster and even with respect to the larger scale structure, which cannot be attributed to rotation [Carter and Metcalfe, 1980].

Overall, the innermost regions of galaxy clusters is special, as the more extreme environment makes two-body collisions, that as said before are negligible for typical galaxies in outer regions, important. This argument, along with dynamical friction, are the cornerstones of the last section of this chapter, where we talk about *fossil clusters*, in which these processes are believed by some (e.g. Ponman et al. [1994], Jones et al. [2003]) to have led to overgrown central galaxies, in expense of their nearby, massive companions.

Turning now to the gas content of clusters, the ICM is sparse, but very hot, emitting brehmsstrahlung radiation on X-rays, with luminosities of the order of $L_X \sim 10^{43} - 10^{45}\text{erg/s}$ and constitute the greatest fraction of cluster baryons. Instead galaxies, which are almost non-collisional, the gas shows structure characteristic of fluid flows, specially when different clusters collide, as in the famous *Bullet cluster*. The separation of gas and dark matter profiles in these systems is today one of the most pressing arguments against modified theories of gravity to account



Figure 2.6: A typical massive cD galaxy with an active nucleus, M87. (Source: Raniere Menezes, IAG Telescope, OPD)

for the missing mass problem in galaxies and clusters [Clowe et al., 2006], as well as helping constrain dark matter models [Harvey et al., 2015].

Because the gas emits radiation with such an immense power, it was expected that the gas would cool and flow towards the centre of the cluster [Fabian, 1994, Croton et al., 2006]. These *cooling flows* have been inferred in the form of sharp central peaks in central emissivity, but they do not correspond to the total expected cooldown. The leading hypothesis for the prevention of massive cooling flows is the reheating of the gas due to the feedback provided by *Active Galactic Nuclei* (AGNs).⁹

Groups are the smaller systems of galaxy associations. They are composed of a few galaxy of a few galaxies of luminosity $L \sim L^*$ (see the next section) and comprise slightly more than half of nearby structures in the universe, being responsible for about 1% of the luminosity density of the universe.

2.4 Observables of Galaxy Systems

The main features that are physically relevant for galaxy cluster astrophysics are the total mass, total luminosity, and relaxation status whereas for cosmology, the number counts of clusters per mass interval is, as we have previously seen, of particular importance. Unfortunately, except for luminosity, none of these constitute a direct observable.

The characterisation of cluster luminosity is given by its distribution, which is can be described by the distribution of galaxy counts per luminosity interval, or the *luminosity function*. The luminosity function of galaxies¹⁰ do not differ qualitatively from galaxies in the field to those in systems, and can be represented by a Schechter function [Schechter, 1976], where $\Phi(L)dL$ represents the number of galaxies in a luminosity interval $[L, L + dL]$, as:

$$\Phi(L) = \left(\frac{\Phi^*}{L^*}\right) \left(\frac{L}{L^*}\right)^\alpha \exp\left(-\frac{L}{L^*}\right) \quad (2.28)$$

where L^* is a characteristic Luminosity above which the number of galaxies decreases exponentially, and Φ^* is the normalisation of

⁹ Active Galactic Nuclei are thought to be *supermassive black-holes*, which in turn are another prediction of ETG, as we have discussed in chapter 1.

¹⁰ analogous to the mass function for whole clusters

the distribution. The luminosity function can also be written in terms of magnitude as.

$$\Phi(M_\lambda) = (0.4 \ln 10) \Phi^* 10^{0.4(\alpha+1)(M_\lambda^* - M_\lambda)} \times \exp\left(-10^{(M_\lambda^* - M_\lambda)}\right) \quad (2.29)$$

where M_λ is the absolute magnitude of the galaxy at a filter around the frequency λ .

The total luminosity of the cluster can be then calculated as

$$L_{tot} = \int_0^\infty dL L \Phi(L) = \Phi^* L^* \Gamma(2 + \alpha) \quad (2.30)$$

where $\Gamma(x)$ is the gamma function $\Gamma(x) := \int_0^\infty t^{x-1} e^{-t} dt$.

Masses of clusters can be characterised by the radial density distribution, as shown before. These masses must always be measured by proxy, since they cannot be readily measured. Fortunately, a range of mass proxies exist such as the temperature of the intracluster medium plasma, displacement of the CMB spectrum due to the Sunyaev-Zel'dovich effect, luminosity and richness, which is the number of galaxies in the cluster, the velocity dispersion of member galaxies and finally, distortions of background galaxies due to gravity, which will be studied in detail on [chapter 3](#). We briefly describe other mass proxies here to place ourselves into that picture, and to draw some commentaries on the application.

The temperature of the intracluster gas strongly correlates with the total mass, because the depth of the gravitational potential is related to the mean kinetic energy of the gas particles, if we assume hydrostatic equilibrium. The mass enclosed inside a radius r is given as a function of the radial profiles of gas density and temperature as

$$M(r) = -\frac{k_B T r^2}{G \mu m_p} \left(\frac{d \ln \rho_g}{dr} + \frac{d \ln T}{dr} \right) \quad (2.31)$$

where k_B is the Boltzmann constant, $\mu \approx 0.63$ is the average mass of gas particle per units of proton mass m_p , and ρ_g is the density of the gas. In current practice, a mass-temperature relation is calibrated by weak lensing measurements to avoid lack of accuracy due to simplified assumptions, which do not take into

account a variety of other phenomena, such as the feedback due to AGNs in massive galaxies, that can bias the mass-temperature relation significantly.

The ICM gas temperature itself can be measured by X-ray spectroscopy, in space-based telescopes as Chandra and XMM-Newton¹¹ or through the observation of the Sunyaev-Zel'dovich effect, as the inverse Compton scattering by the ICM electrons pushes incoming CMB photons to higher energies. One of the advantages of this method is that it can probe and find clusters of galaxies to much greater distances, since the SZ effect is independent of redshift (as the CMB is further behind any structure in the universe). The gas is isothermal and is described by a β -model, temperature of the ICM is related to the shift of the CMB temperature and luminosity distance by

$$T_X \propto \left(\frac{\Delta T}{T} \right)_{CMB}^{4/3} d_L^{-4}. \quad (2.32)$$

where d_L is the luminosity distance (Eq. 1.25). The *velocity dispersion* of the galaxies provide another way to measure the mass of a galaxy cluster. Using the virial theorem, one can show that

$$M = \frac{3\pi R_G \sigma_v^2}{2G}, \quad (2.33)$$

where $R_G \sim 1\text{Mpc}$ is the *gravitational radius* and σ_v is the velocity dispersion, measured by comparing galaxy redshifts to the cluster overall redshift.

Both gas temperature and velocity dispersion models assume some sort of dynamical equilibrium. Another way to investigate the mass distribution in clusters is through the observation of the gravitational effects on the light of background galaxies. This method is called gravitational lensing and will be discussed in detail in the next chapter, as it will be put to use in part II.

The radial distribution of mass, galaxies, luminosity, and so on can only be directly investigated in the plane of the observation, not in the line of sight direction. Consequently, all quantities

¹¹ G.B. Lima Neto. *Astronomia Extragaláctica*. 2014

must be transformed to projected quantities as

$$\Sigma(R) = \int_{-\infty}^{+\infty} dz \rho(\sqrt{R^2 + z^2}) = 2 \int_R^{+\infty} \frac{dr \rho(r)}{\sqrt{r^2 - R^2}}. \quad (2.34)$$

The projected mass density can also be written as a differential mass density, which will be useful as it is directly observable by lensing, as

$$\Delta\Sigma(R) = \bar{\Sigma}(r < R) - \Sigma(R) \quad (2.35)$$

Where $\bar{\Sigma}(r < R)$ is the average density in a region inside R , that is

$$\begin{aligned} \bar{\Sigma}(r < R) &= \frac{\int_0^R 2\pi r dr \Sigma(r)}{\int_0^R r dr} \\ &= \frac{2}{R^2} \int_0^R dr r \Sigma(r) \end{aligned} \quad (2.36)$$

In practice, today, gravitational lensing is used to calibrate scaling relations between either gas properties or luminosity to cluster masses. Since the cost of direct spectroscopy is prohibitive, this allows us to study a greater number of systems to use in the determination of the mass function.

The measurement of luminosity and masses are also combined as M/L ratios. Since it is known that reddish K-stars that populate elliptic galaxies have mass-to-light ratios of the order $(M/L)_K \sim 3(M_\odot/L_\odot)$, it is interesting to compare to the mass-to-light ratio of these galaxies. The result, known as early as 1933 [Zwicky, 1933] is that the mass-to-light ratios in clusters is

$$\left(\frac{M}{L}\right) \sim 300h \left(\frac{M_\odot}{L_\odot}\right), \quad (2.37)$$

which displays a discrepancy of around two magnitudes. This missing¹² mass problem originated the idea of dark matter, an ingredient today considered crucial to explain the large scale structure of the universe and many derivative effects observed in modern surveys.

¹² *missing*, perhaps in the sense of *missing an explanation*, since it is an excess, not a lack of mass.

2.5 *Magnitude Gaps and Fossil Systems*

We now turn to study in particular one aspect of galaxy systems, the luminosity dominance of the central galaxies in systems, which will be the main focus of our application. It has been known for some time that central galaxies in groups and clusters are significantly different from other galaxies in both their morphological aspects and their scaling relations [von der Linden et al., 2007]. First, they differ in that they do not normally fit into the luminosity function of their own clusters, in the Schechter model. Also, they have different M/L ratios, metallicities, and other scaling relations from typical elliptic galaxies, even when in comparison to those of the same scale.

The relationship between the central galaxy and their parent systems is, in turn, important to understand evolutionary effects on galaxies and the origins of galaxy groups and clusters. In this context, the dominance of the CG, most of the times quantified by the difference in magnitude of the (usually brightest) CG to the second brightest in the central region, that is defined by some fraction of r_{200} , has been suggested as an indicator of the relaxation of the system, because it is thought that larger *magnitude gaps* identify systems that had more time for the CG to cannibalise the L^* galaxies in the inner region.

The first identification of a group where the central galaxy was overly dominant was made by Ponman et al. [1994], when they suggested that the system RX J1340.6+4018 was possibly the relic of a former group of galaxies. At first, it was thought to consist of a single galaxy with an extended X-ray halo, but it was later shown [Jones et al., 2000] to be actually a group of about $N \sim 10$ galaxies, out of which the central galaxy accounts for about $\sim 70\%$ of the total optical luminosity, being thus consistent with it being the merger product of the missing L^* galaxies around it.

A formal, empirical definition was given afterwards by [Jones et al., 2003] for such *fossil groups*, and is expressed by

- a high luminosity in X-rays $L_X \geq 0.25 \times 10^{42} \text{erg s}^{-1}$,
- an absolute magnitude gap between the central, usually most luminous galaxy and the second brightest galaxy greater than

$\Delta M_{1-2} = M_{BCG} - M_{2BG} \leq -2$ within half the projected r_{200} radius.

With this definition, the number of such systems is very small (about $\sim 2\%$ of all systems), and only a handful of them have been studied in detail - at first, only groups. In time, however, larger systems were discovered [Cypriano et al., 2006] and have been called as fossil clusters, by analogy.

Using simulations, from which halo formation and evolution can be traced, Dariush et al. [2007] observed that systems with larger magnitude gaps form earlier, on average, lending support to the fossil hypothesis. By earlier here, it is meant that the system has reached the current mass sooner than the average of all halos: these simulations show that fossil groups accreted on average only 1 further galaxy since $z = 1$, compared to the average of 3 for other groups [von Benda-Beckmann et al., 2008, D'Onghia et al., 2005]. The argument is then that because their mass has been assembled before, they have had more time to virialise, with inner cluster dynamics dominating evolution whereas systems that remained accreting mass had external sources for more L^* galaxies.

Another argument for an early formation epoch for these groups is based on observations of these systems, although rare, including through X-ray scaling relations [Khosroshahi et al., 2007] and morphological studies of their central galaxies [Khosroshahi et al., 2006]. Putting all these together into a coherent picture for the overall population, FGs have been repeatedly suggested (e.g. Harrison et al. [2012], Dariush et al. [2010], Khosroshahi et al. [2007] and many others) to be more relaxed systems and, as such [Mantz et al., 2015], to provide unique clues on the history of cosmic mass assembly, the interaction between baryonic matter and host dark matter halos, and to carry information from structure formation at early epochs of the universe.

Dariush et al. [2010] has also proposed to modify the criterion for the optical selection of fossil groups to $\Delta M_{1-4} \leq -2.5$, finding it to be a more efficient probe of identifying early-formed halos than the conventional definition. The idea that fossil systems (FSs) represent early formed unperturbed systems is not uncontroversial, however. Random draws from Schechter luminosity function with a lower number of galaxies have a

higher probability of selecting larger magnitude gaps in the bright end [Hearin et al., 2013], so that the displayed effect could be of statistical nature [Proctor et al., 2011]. Paranjape and Sheth [2012] employed extreme value statistics to show that the distribution of galaxy groups as a function of magnitude gap can be consistent with the distribution resulting from a set of random draws from a global luminosity function, implying that the group mass is only related to the magnitude gap through mutual covariance with richness. [Mulchaey and Zabludoff, 1999], analysing NGC 1132, have suggested that fossil groups may consist of *failed groups*, that is, local overdensities in which other bright galaxies never formed. The masses and M/L ratios of the central galaxies of FSs are also usually too large to be explained as end points of compact group evolution driven just by dynamical friction [Voevodkin et al., 2010]. The basic merger interpretation, however, remains viable, as previously discussed here, in the context of simulations.

Furthermore, the luminosity function of the first fossil group [Jones et al., 2000] and the conclusion that it resides in a sparse environment, was suggested by [D'Onghia and Lake, 2004] to pose a problem for the cold dark matter models, since they did not have as much substructure as expected for such massive systems. On the other hand, simulations have shown that the luminosity function of three FGs, including the first identified by Ponman et al. [1994], RX J1340.6 + 4018, are consistent with Λ CDM predictions. Finally, in contrast to considering FSs as peculiar systems, another possibility that has been speculated is that groups and clusters may go into a fossil phase in their lives, with an absence of significant mergers, with enough time for relaxation [von Benda-Beckmann et al., 2008]. A bright galaxy, or a group, may then sink to the inner region of the system and the object will return to appear as a normal group or cluster of galaxies. Dariush et al. [2010] find that the mass assembly history is similar by these two methods, on average. About 90% of fossil groups which were identified according to both criteria in earlier epochs become non fossils after 4Gyr and the fossil phase persists for ~ 1 Gyr. Using semi-analytic models based on the Millennium simulation [Springel et al., 2005], Gozaliasl et al. [2014] have

shown that 80% of groups ($13 < \log M_{200} < 14$ in M_{\odot}) that would classify as fossil at redshift $z = 1$ lose their large magnitude gaps, but that 40% of the clusters ($\log M_{200} > 14$ in M_{\odot}), on the other hand, retained large gaps.

Proper statistical comparisons between populations of observed fossil systems and other, typical galaxy associations are still in their infancy since the low number of fossil systems and their lower representation on the existing X-ray surveys do not provide enough statistics. In any case, fossil systems are relatively rare.

[Dariush et al. \[2010\]](#) has reported that using the $\Delta M_{1-2} \leq -2$, the fraction of fossil systems is 2% in observations and 2.1% in simulations. Using $\Delta M_{1-4} \leq -2.5$, 6.2% and 5.1% are fossils, in observation and simulation respectively.

Currently, the state of affairs about the true nature of FSs, if they are or not physically singular systems with earlier accretion histories, remain undecided. In these terms, our work places itself as another step in the study of these systems in order to assess if they consist of a separate statistical population.

In a final commentary, particular to this work, we note that despite the fact that the original definition of FSs include an X-ray threshold, there is interest in the study of systems selected on optical criterion alone, the *optical fossil candidates* [[Dariush et al., 2007](#)], since the scaling relations of the X-ray gas have been shown to be in concordance with the overall population of galaxy clusters and groups. This is the approach we take: to characterise and compare the magnitude gap to the mass, mass concentrations, and M/L ratios, by using gravitational lensing over a population of ~ 1500 systems. We also do not simply divide the population into fossil and non fossil optical candidates since the low number count of fossil candidates would handicap the cross-correlation weak lensing technique we adopt to maximise our lensing signal (more details in [chapter 3](#) and [chapter 4](#)).

3

Gravitational Lensing

GRAVITATIONAL LENSING is the name given to the deflection of light rays by gravity. It is one of the best understood and most remarkable effects of ETG, and was among the first empirical tests performed to validate it. The idea that gravity should act on light precedes Einstein's work by more than a century by Soldner [1804], and is related to the description of light as a stream of luminous particles. Adopting this point of view, together with the equivalence principle, Einstein re-derived the deflection angle for light particles approaching a gravitation source with a given impact parameter.

However, after the discovery of the full field equations (Eq. 1.1) it was perceived that the total observed deflection angle should actually be twice the classical result - this factor of two is a result of properties of the curvature of the lorentzian manifold.¹ This offered a prototypical scenario to test the new theory of gravity against the old Newtonian paradigm. In 1919 a solar eclipse provided the perfect opportunity: the knowledge of the position of stars in the sky was sufficiently precise to detect the predicted deflection [Dyson et al., 1920] and the result supported Einstein's theoretical results.

The specific subject of gravitational lensing was, however, to remain relatively quiet in the next decades. After a running discussion among Eddington [1920], Chwolson [1924] and Einstein [1936] it was thought that the phenomena would be an occurrence too rare to observe - considering only chance alignment of stars. Zwicky, however, pointed that entire galaxies could display visible effects on other farther galaxies behind.

¹ Using the Schwarzschild metric with r_s being the characteristic radius and a light ray with impact parameter b . The equation for the total deflection angle is:

$$\hat{\alpha} = \int \frac{dr}{r^2 \sqrt{\frac{1}{b^2} - \left(1 - \frac{r_s}{r}\right) \frac{1}{r^2}}}, \quad (3.1)$$

which yields

$$\hat{\alpha} \approx \frac{2r_s}{b} = \frac{4GM}{c^2 b}. \quad (3.2)$$

The two-fold factor actually is tied to another effect correctly addressed by the theory, the precession of orbits. Both are due to the non-conservation of the Laplace-Runge-Lenz vector in ETG.

Furthermore, having calculated the masses of Virgo and Coma clusters to be higher than previously thought by no less than 2 orders of magnitude [Zwicky, 1933], he argued that the deflection of light of distant galaxies could provide not only tests of ETG but also allow the determination of cluster masses. Finally, Zwicky calculated the lensing probability and concluded that about one percent of distant galaxies should be significantly distorted [Zwicky, 1937]. Nonetheless, his predictions would wait several more decades until adequate observational technologies brought Gravitational Lensing back to the spotlight.

In 1964 Sjur Refsdal derived the main equations of the lensing formalism, and showed a method to estimate the Hubble constant H_0 [Refsdal, 1964a,b] - by measuring the time delay between two different lensed images of the same object. With the subsequent discovery of quasars [Schmidt, 1963], it was proposed that gravitational lensing by galaxies could be used together with these distant, extremely bright objects to probe the masses of galaxies, and realise Refsdal's ideas. Finally, only fifteen years later, came the first observation of a doubly lensed quasar, by Walsh et al. [1979] (Fig. 3.1).

The coming of the age for cluster astrophysics, on the other hand came in the late 70's and early 80's. With that Narayan et al. [1984] explored in detail the possibility of clusters acting as powerful lenses. Finally, [Lynds and Petrosian, 1986] and Soucail et al. [1987] independently discovered images of "giant arcs", which have shown to be strongly distorted images of distant background galaxies near the core of foreground galaxy clusters. This was immediately interpreted by Paczynski [1987] as the effect of gravitational lensing - what would be confirmed by the measurement of the redshift of the arc in Abell 370 [Soucail et al., 1988].

The construction of the Hubble Telescope, the advances in ground telescopes, and with these the ability to precisely measure galaxy shapes in astronomical images all paved the way for the systematic use of Gravitational Lensing not only as an observation of ETG effects but also as a tool to measure characteristics of galaxy clusters, the search for very high redshift galaxies and even exoplanets - a great variety of results, in the same fashion

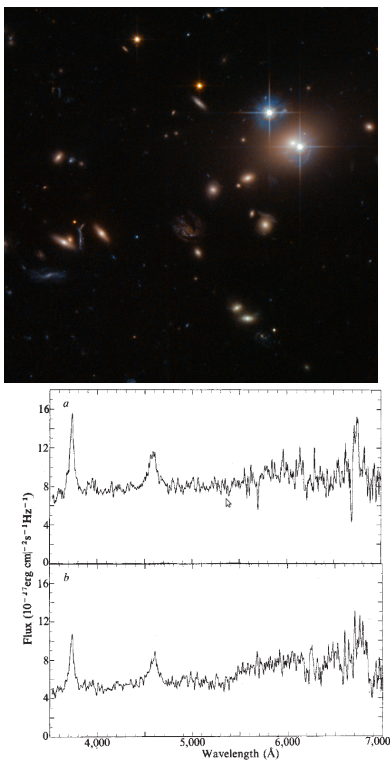


Figure 3.1: Upper: The double quasar QSO0957 + 561 depicted by the Hubble Space Telescope in the upper right area of the image as the "star like" objects with diffraction rays. The reddish light between them is the foreground deflector galaxy. Their spectra matches as an object at redshift $z = 1.413$, with the deflector at $z = 0.355$. The separation is of about $6''$. Source: ESO/NASA. Lower: Reproduction of the spectra of each component, from Walsh et al. [1979]

as spectroscopy went from a hint of the quantum nature of the atomic structure to a basic technique to investigate properties of baryonic matter.

3.1 General Lensing Theory

Since the environment of galaxy clusters have small curvatures, ETG in such vicinities can be approximated by linearisation. Then the deflection due to a spatially extended mass can be written simply as a vector sum over point masses. In the continuum limit, this sum becomes an integral over the spatial density distribution $\rho(\vec{x})$. Now, if the deflection is small we can approximate the gravitational potential along the deflected trajectory by the potential along the undeflected trajectory.² Using a system of coordinates in the plane of the sky $\vec{\xi} - \vec{\xi}' = \vec{b}$ and the redshift in the line-of-sight z , deflection angle will be given then by a sum of the contributions of each point:

$$\vec{\alpha}(\vec{\xi}) = \frac{4G}{c^2} \int dm = \frac{4G}{c^2} \int \rho dV \quad (3.3)$$

$$\vec{\alpha}(\vec{\xi}) = \frac{4G}{c^2} \int d^2\xi' \int dz \rho(\vec{\xi}', z) \frac{\vec{b}}{|\vec{b}|^2}, \vec{b} \equiv \vec{\xi} - \xi'. \quad (3.4)$$

In which the first integral is calculated over the plane - in practical situations, a large enough area - and the second throughout the line of sight up to the source object redshift. In the limit of a *thin lens*³, where the distances between the source, lens, and observer are much larger than the size of the deflector, we can use the projected mass density

$$\Sigma(\vec{\xi}) = \int \rho(\vec{\xi}, z) dz, \quad (3.5)$$

so that the deflection can be rewritten as:

$$\vec{\alpha} = \frac{4G}{c^2} \int \frac{(\vec{\xi} - \vec{\xi}') \Sigma(\vec{\xi}')}{|\vec{\xi} - \vec{\xi}'|^2} d^2\xi'. \quad (3.6)$$

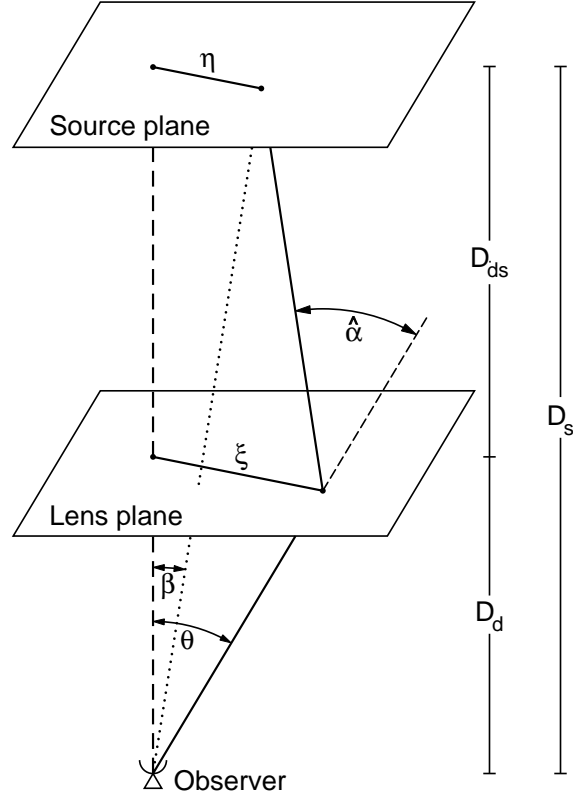
With the relationship between the deflection angle and the deflector mass distribution built from the theory, what remains is a purely (pseudo-riemannian) geometrical problem. The typical

² (...)as in the Born approximation in quantum mechanics.

³ In the context of cluster lenses, this condition holds very generally, a cluster of galaxies has a scale of few Mpc, whereas the distances of lens systems and their lensed sources are considerable fractions of the Hubble length cH_0 , which is about 4.3Gpc.

situation considered in lensed systems has a deflector at a certain redshift z_d , a set of sources with redshifts z_s . The source and lens planes are defined as planes perpendicular to the optical axis of the observer (the dashed line in the figure). If $\vec{\eta}$ is the two-dimensional position of the source relatively to this axis, then we can write

Figure 3.2: Gravitational lens geometry. In the thin lens approximation we can consider that all the change in direction of the light rays takes place in a specific plane. Here, all distances used must specifically be angular diameter distances, since the large scale structure of space-time is not euclidean. Source: [Bartelmann and Schneider, 2001]



$$\vec{\eta} = \frac{D_s}{D_d} \vec{\xi} - D_{ds} \vec{\hat{\alpha}}(\vec{\xi}), \quad (3.7)$$

which, using angular coordinates $\vec{\eta} = D_s \vec{\beta}$ and $\xi = D_d \vec{\theta}$ can be written as:

$$\vec{\beta} = \vec{\theta} - \frac{D_{ds}}{D_s} \vec{\hat{\alpha}}(D_d \vec{\theta}). \quad (3.8)$$

This is the so-called *lens equation* for the system and can be understood as saying that an object which would be observed at a "true" position in the sky $\vec{\beta} = (\beta_1, \beta_2)$ in its source plane will be seen at another position $\vec{\theta} = (\theta_1, \theta_2)$ in an "image" plane according to the deflection given by $\vec{\hat{\alpha}}$ and the given ratio of angular diameter distances.

In the original case of star images being displaced due to the gravity of the Sun, we had both $\vec{\beta}$ and $\vec{\theta}$, since the angular separation of the sun and the stars vary with time. However, deep object configurations do not change significantly and then neither $\vec{\beta}$ nor $\vec{\alpha}$ can be directly observed as $\vec{\theta}$, D_d , and D_{ds} can. So we seem then to have reached an insurmountable dead-end.

The solution to this problem comes - in very different ways - by using the lens equation multiple times and constraining them all together to make such system solvable. The constrain itself comes, as we will see, from the fact that there can be reasonable assumptions about the sources and the deflector.

To proceed, it is useful to define a function that depends on just the distances of the deflector and some source, called the *critical surface density of the lens* as

$$\Sigma_{cr} := \frac{c^2 D_s}{4\pi G D_{ds} D_d}. \quad (3.9)$$

One of the main reasons behind this definition is that it can be proven that arrangements of lens-source pairs in which the projected surface density surpasses this critical value, the lens equation will display multiple solutions⁴. Then, when the lens equation displays multiple solutions, a single source will be displayed in multiple images around the lens.

⁴ Note that $\Sigma > \Sigma_{cr}$ is a *sufficient* but not *necessary* condition for multiple solutions:

P. Schneider, J. Ehlers, and E. E. Falco. *Gravitational Lenses*. 1992

Rewriting the angle equation with the critical density, we have:

$$\kappa(\vec{\theta}) = \frac{\Sigma(D_d \vec{\theta})}{\Sigma_{cr}}. \quad (3.10)$$

Inserted to the deflection angle equation, this yields:

$$\vec{\alpha}(\vec{\theta}) = \frac{1}{\pi} \int d^2\theta' \frac{(\vec{\theta} - \vec{\theta}')\kappa(\vec{\theta}')}{|\vec{\theta} - \vec{\theta}'|^2},$$

which suggests introducing a $2D$ gravitational potential ψ for which

$$\nabla^2\psi = 2\kappa \quad (3.11)$$

holds. This describes a line-of-sight integrated two-dimensional "Newtonian" potential, rescaled by Σ_{cr} , called the lensing potential, such that now $\vec{\alpha}(\vec{\theta}) = \vec{\nabla}\psi(\vec{\theta})$ and $\kappa(\vec{\theta}) = \frac{1}{2}\nabla^2\psi(\vec{\theta})$.

The lens equation together with the density-deflection relations define a surjective mapping from the image plane $\vec{\theta}$ onto the source plane $\vec{\beta}$. The shape of the images of extended objects will differ from the shape of their respective sources because the deflection of light ray bundles is locally differential. We can then investigate these local properties of this mapping in small neighbourhoods through the Jacobian matrix, given by:

$$A_{ij} = \frac{\partial \beta_i}{\partial \theta_j} = \delta_{ij} - \frac{\partial \alpha_i}{\partial \theta_j} = \delta_{ij} - \frac{\partial^2 \psi}{\partial \theta_i \partial \theta_j}. \quad (3.12)$$

Evaluating each term in the Jacobian we can write the transformation matrix explicitly as:

$$A = \begin{bmatrix} 1 - \kappa - \gamma_1 & -\gamma_2 \\ -\gamma_2 & 1 - \kappa + \gamma_1 \end{bmatrix}, \quad (3.13)$$

where we introduced:

$$\gamma_1 = \frac{1}{2} \left(\frac{\partial^2 \psi}{\partial \theta_1^2} - \frac{\partial^2 \psi}{\partial \theta_2^2} \right) \quad (3.14)$$

$$\gamma_2 = \frac{\partial^2 \psi}{\partial \theta_1 \partial \theta_2}. \quad (3.15)$$

The reason why we introduced γ is simply because the transformation A can now be expressed as two observationally different effects.

If we combine γ_1 and γ_2 into a complex quantity $\gamma = \sqrt{\gamma_1^2 + \gamma_2^2} e^{2\phi i}$ we can then write:

$$A = (1 - \kappa) \begin{bmatrix} 1 & 0 \\ 0 & 1 \end{bmatrix} - |\gamma| \begin{bmatrix} \cos 2\phi & \sin 2\phi \\ \sin 2\phi & -\cos 2\phi \end{bmatrix}. \quad (3.16)$$

5

The local distortion of the images can now be understood as a *convergence* part κ , that gives us how much an image is enlarged or diminished in area, and the traceless *shear* γ , which quantifies how much an image is laterally distorted.

There are two remarks that should be made about the local properties of the lensing transformations:

	< 0	> 0
κ		
$\text{Re}[\gamma]$		
$\text{Im}[\gamma]$		

Figure 3.3: The effects of the two components of the lensing transformation. κ changes the size of images while γ distorts images laterally. (Source: Wikipedia)

⁵ where ϕ is the angle between the shear frame and one coordinate axis

- the shear γ is *not* a vector, due to its transformation properties under rotations: the components of the shear are mapped onto themselves (an identity transformation) with a half-rotation. The reason for this behaviour due to it being the traceless part of the jacobian matrix (3.16). Hence, the shear is actually a 2-spinor.
- the convergence κ preserves surface luminosity, due to the *theorem of conservation of étendue*, which can be better understood in Hamiltonian optics as an analogue of Liouville's theorem.⁶

The ratio between the solid angles of a local neighbourhood in the image plane and its respective "original" source distribution is given by:

$$\mu = \frac{\theta \, d\theta}{\beta \, d\beta} = \frac{1}{\det A} = \frac{1}{(1 - \kappa)^2 - |\gamma|^2}, \quad (3.17)$$

and is called the *magnification*. There may be regions in a configuration where this determinant is zero, which will correspond to a *critical* curve in the plane of images, and a respective *caustic* in the source plane. This suggests there are areas which have infinite magnification, which evidently cannot be true, which is due to approximations taken in this derivation. Still, in such cases, dramatic arcs and even ring images of background objects appear.⁷

When such effects of distortion and multiple imaging is present, we call this *Strong Gravitational Lensing* and the method for determining masses of deflectors usually involves reconstructions of the source based on the likelihood of the multiple images or giant arcs displayed being mapped to some original configuration - this solves our "dead-end" by enabling multiple uses of the lensing equation for each. The counterpart, *Weak Gravitational Lensing*, refers to situations where light rays from distance sources is just slightly distorted in a coherent fashion. In these configurations, the effect is quantifiable through a statistical measure of shapes of background objects which provide an estimator for γ as well as κ , the former we will see in the next section.

⁶ P. Schneider, J. Ehlers, and E. E. Falco. *Gravitational Lenses*. 1992

⁷ A nice example is that presented by an isothermal sphere mass distribution. Using the an isothermal mass distribution [Schneider, 2006] we have:

$$\Sigma(\xi) = \frac{\sigma_v^2}{2G\xi},$$

which yields

$$\kappa(\theta) = \frac{\theta_E}{2\theta},$$

with

$$\theta_E = 4\pi \left(\frac{\sigma_v}{c} \right)^2 \frac{D_{ds}}{D_s},$$

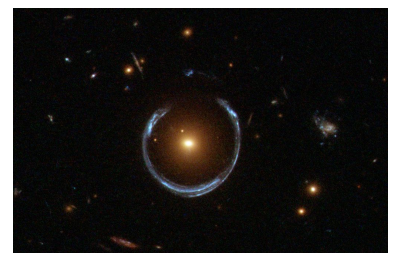
where θ_E is called the *Einstein radius* of the lens. In this case, we have:

$$|\vec{\alpha}| = \theta_E$$

$$\psi(\vec{\theta}) = \theta_E \theta$$

$$\mu(\vec{\theta}) = \frac{\theta}{\theta - \theta_E},$$

so that when $\theta \approx \theta_E$, $\beta \approx 0$, and the magnification is very large as we can see in the incredibly near-perfect alignment below:



Source: NASA

More recently, the number counts of background objects has been also used for mass profile measurements. Since the effect of a gravitational lens is to spread out the image of the background sources, from this alone you would expect a decrease in the projected number density of background galaxies. However, since magnification, as we have seen, enhances the flux of background objects you would expect an increase of objects in images - which are limited by flux. The interplay between these effects can be modelled in comparison to undeflected fields in regions away from cluster centres to determine projected mass distributions, in a way that defeats the mass-sheet degeneracy, as the magnification is immune to such invariance. It is in this way that weak lensing can provide an estimator for κ .

Finally, as a note, the study the region in-between the strong and weak regimes - the *flexions* - has also been employed as a complimentary technique to bridge and combine strong and weak lensing for a deeper, more complete analysis of mass distributions through lensing effects.

For strong Lensing, magnification and flexions the reader is recommended to [Merten \[2010, 2008\]](#), [Meylan et al. \[2006\]](#) and others, as we now draw our attention to weak lensing shear analysis, which will be our main tool in the application.

3.2 *Weak Gravitational Lensing*

While the presence of any amount of matter density deflects the path of light rays passing around it, this effect will rarely present itself as the giant arcs and multiple images usually associated with gravitational lensing. Most regions in the sky are very slightly affected by foreground mass distributions, being deeply into the weak lensing regime, in which the deflection is impossible to quantify by a single background source. Fortunately, even in such cases, the presence of the foreground mass can be detected, by way of a systematic alignment of background sources around the lensing mass. Weak gravitational lensing will be then an intrinsically statistical measurement, which overcomes the subtlety of the effect by combining a large number of individual measurements.

In regions that $\kappa, \gamma \ll 1$, the Jacobian of the lensing transformation - and by it an estimator for Σ - can be mapped by observing the combined effect of the shear γ on the distribution of projected ellipticities of background galaxies: as the shapes of a collection of source galaxies will be dominated by their nearly random distributed unlensed shapes, coherent distortions can single out and quantify lensing effects.

Even if galaxy shapes are not perfect ellipses, their ellipticities can be measured by finding best-fit elliptical models to the sources, or by measuring the second moments of the image about centroids. For a given image, if the distribution of surface brightness in a small neighbourhood around a source is given by a function $I(\vec{\theta})$, the centroid of the object can be estimated by the average of the distribution

$$\langle \vec{\theta} \rangle = \frac{\int d^2\theta I(\vec{\theta}) \vec{\theta}}{\int d^2\theta I(\vec{\theta})}, \quad (3.18)$$

whereas the second moment tensor is given by

$$Q_{ij} = \frac{\int d^2\theta I(\vec{\theta}) (\theta_i - \langle \theta_i \rangle) (\theta_j - \langle \theta_j \rangle)}{\int d^2\theta I(\vec{\theta})}. \quad (3.19)$$

If we then define the ellipticity of the object as⁸

$$\epsilon := \frac{Q_{11} - Q_{22} + 2iQ_{12}}{Q_{11} + Q_{22} + 2\sqrt{Q_{11}Q_{22} - Q_{12}^2}}, \quad (3.20)$$

we can write then the second moment tensor of the unlensed source with the observed tensor Q and the transformation A as

$$Q^s = AQA^T = AQA, \quad (3.21)$$

which gives us the original ellipticities of the source as

$$\epsilon^s = \begin{cases} \frac{\epsilon - g}{1 - g^*\epsilon}, & |g| \leq 1 \\ \frac{1 - g\epsilon^*}{\epsilon^* - g^*}, & |g| > 1 \end{cases}$$

⁸ Ellipticities are usually defined by the ratio

$$\epsilon := 1 - q = 1 - \frac{b}{a},$$

where b/a is the axis ratio of the ellipse. In gravitational lensing it is customary to define quantity

$$\epsilon := \frac{1 - q}{1 + q} e^{2i\phi},$$

where ϕ is the same we have seen before in the shear definition - ellipticity, as shear, is transformed into itself by a half-rotation. Joining this with the elliptical parameters

$$\begin{aligned} Q_{11} &= a^2 \cos^2 \phi + b^2 \sin^2 \phi \\ Q_{22} &= a^2 \sin^2 \phi + b^2 \cos^2 \phi \\ Q_{12} &= (a^2 - b^2) \sin \phi \cos \phi, \end{aligned}$$

gives the ellipticity definition a practical meaning.

with the *reduced complex shear* g given by

$$g(\vec{\theta}) = \frac{\gamma(\vec{\theta})}{1 - \kappa(\vec{\theta})}. \quad (3.22)$$

Now, the ellipticity expression can be inverted to give

$$\epsilon = \begin{cases} \frac{\epsilon^s + g}{1 + g^* \epsilon^s}, & |g| \leq 1 \\ \frac{1 + g \epsilon^{s*}}{\epsilon^{s*} + g^*}, & |g| > 1 \end{cases}. \quad (3.23)$$

If we consider many galaxies in a small neighbourhood of the image, using our ansatz that the intrinsic ellipticity ϵ^s is randomly distributed we have $\langle \epsilon^s \rangle = 0$, so, the averaged measured ellipticity should amount to

$$\langle \epsilon \rangle = \begin{cases} g, & |g| \leq 1 \\ \frac{1}{g^*}, & |g| > 1 \end{cases}. \quad (3.24)$$

So, in the weak lensing limit the averaged ellipticities in a small region provides an estimator for the local reduced shear g . However, g is a single quantity, but κ and γ are two and κ is the quantity most directly related to the mass distribution, through $\Sigma = \kappa \Sigma_{cr}$. Any transformation of the form

$$\begin{aligned} 1 - \kappa' &= \lambda(1 - \kappa) \\ \gamma' &= \lambda\gamma \end{aligned}$$

leaves g unaltered. This is the so called *mass-sheet degeneracy*, because it amounts to the fact that a sheet of uniform surface density does not produce any lensing effects. This is a serious problem to the calculation of masses of individual clusters and can be dealt with in some ways, the most straightforward of them is to consider magnification effects. Since the quantity

$$\mu = \frac{1}{(1 - \kappa)^2 - |\gamma|^2}$$

is *not* invariant through the aforementioned transformation, it can be used to calibrate the shear/convergence-reduced shear relation.

Another useful way to constrain the degeneracy, used in cluster surveys and in this work, is to assume a spherical distribution of the lens mass, this immediately breaks the degeneracy by introducing a model for the line-of-sight mass distribution, with a one-to-one correspondence between κ and γ .

3.3 Parametric Modelling

The universality we previously discussed of the halo mass profile provides us a method to use gravitational lensing to investigate observables of galaxy systems. An axisymmetric matter distribution can be described by a radial function $\Sigma(\vec{\theta}) = \Sigma(\theta)$ so that the deflection angle yields

$$\begin{aligned}\vec{\alpha}(\vec{\theta}) &= \frac{\vec{\theta}}{\theta^2} 2 \int_0^\theta d\theta' \theta' \kappa(\theta') \\ \hat{\alpha}(\vec{\xi}) &= \frac{\vec{\xi}}{\xi^2} \frac{4G}{c^2} 2\pi \int_0^\xi d\xi' \xi' \Sigma(\xi') \\ &= \frac{4GM(< \xi)}{c^2 \xi} \frac{\vec{\xi}}{\xi},\end{aligned}$$

where $M(< \xi)$ is the total mass enclosed inside radius ξ .⁹ Since all directions $\vec{\beta}$, $\vec{\theta}$, and $\hat{\alpha}$ are collinear we can write the lens equation with scalars

$$\beta = \theta - \alpha(\theta), \quad (3.25)$$

where the deflection angle is given by

$$\alpha(\theta) = \frac{m(< \theta)}{\theta} = \bar{\kappa}(< \theta)\theta, \quad (3.26)$$

where again $m(< \theta)$ is the dimensionless mass enclosed inside the radius θ and $\bar{\kappa}(< \theta)$ is the averaged convergence in the same region. The Jacobian matrix can be then calculated rewriting the lens equation as

$$\vec{\beta} = \left[1 - \bar{\kappa}(< |\vec{\theta}|) \right] \vec{\theta}, \quad (3.27)$$

⁹ This is, in some approximated way, a direct consequence of Birkhoff's Theorem: spherical solutions can be seen as point masses with at a large enough distance.

then applying the definition (eq. 3.16) we arrive at

$$A(\theta) = [1 - \bar{\kappa}(< \theta)] \mathbb{1} - \frac{1}{\theta} \frac{d\bar{\kappa}}{d\theta} \begin{bmatrix} \theta_1^2 & \theta_1\theta_2 \\ \theta_1\theta_2 & \theta_2^2 \end{bmatrix}. \quad (3.28)$$

If we now transform θ into a polar coordinate system around the centre of the distribution, we can write $\vec{\theta} = \theta(\cos \phi, \sin \phi)$ which, together with the former presentation of the jacobian matrix in eq. 3.16 yields:

$$\gamma(\theta) = (\bar{\kappa}(< \theta) - \kappa(\theta)) e^{2\phi i} \quad (3.29)$$

It is easy to see that whenever a given ellipticity γ is rotated by ϕ the result amounts to a multiplication $\gamma e^{-2\phi i}$, so we can define a polar coordinate system for the ellipticities such that $\gamma_p := \gamma e^{-2\phi i}$. Like the Cartesian ellipticity, the polar ellipticity admits a separation in two components which are the tangential γ_t and cross γ_\times components that can be calculated by:

$$\gamma_t = -\Re[\gamma_p] = -[\gamma_1 \cos(2\phi) + \gamma_2 \sin(2\phi)] \quad (3.30)$$

$$\gamma_\times = -\Im[\gamma_p] = -[\gamma_1 \sin(2\phi) - \gamma_2 \cos(2\phi)] \quad (3.31)$$

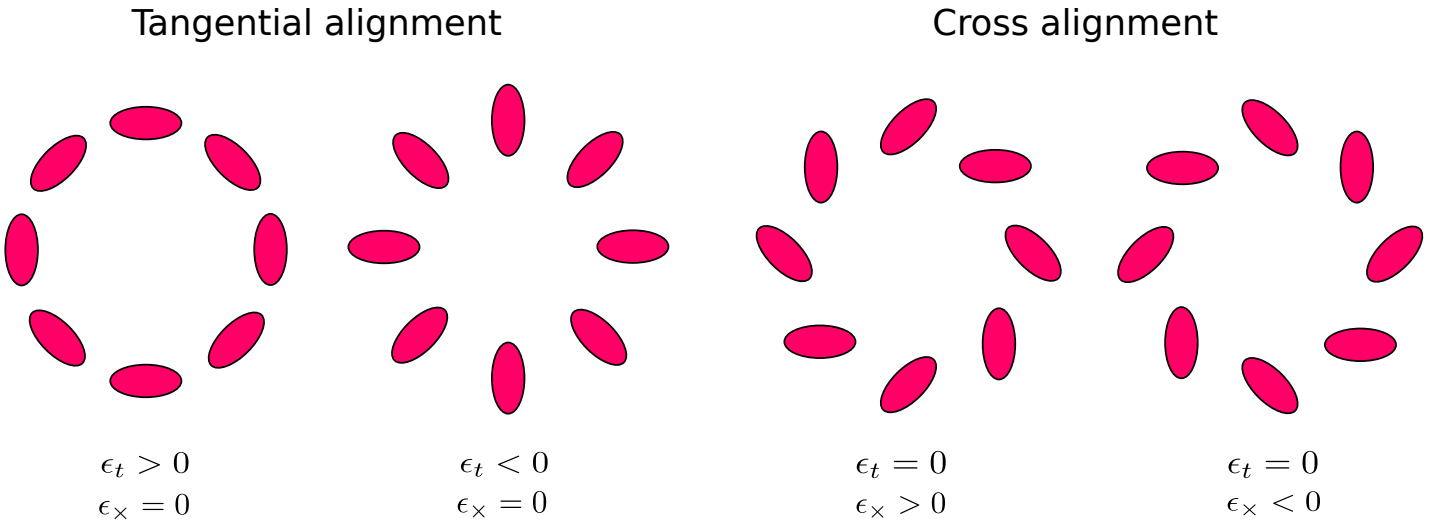


Figure 3.4: Considering a spherical symmetry, we can write the ellipticity of an object as a sum of a tangential component and a cross component. *Source: Mirian Caštejon Molina*

The negative sign in the above equation can be understood as follows: consider a circular mass distribution and a point on the θ_1 axis outside the Einstein radius. The image of a circular source will be mapped into a stretched image along the θ_2 axis.

In this case, $\phi = 0$, the shear is real and negative and in order to have tangential shear positive, and thus to define the tangential component according to intuitive understanding, this minus sign is introduced. Owing to the spherical symmetry, we expect only the tangential projection of γ_t effects from gravitational lensing, whereas γ_\times can be used to investigate possible systematic effects.

Now, using that

$$\gamma(\theta) = \bar{\kappa}(< \theta) - \kappa(\theta), \quad (3.32)$$

we can rewrite this equation as a more convenient form:

$$\Sigma_{cr}\gamma_t(\theta) = \bar{\Sigma}(< \theta) - \Sigma(\theta), \quad (3.33)$$

which will suit better to practical cases when we combine clusters into stacked halos, because since each lens-source pair z_d and z_s is well determined, we can use the left hand side of the equation (in the limit that $\gamma \sim g$) as data and treat the right hand side as model.

Effectively, we will have many sources for gravitational signals: a source point contribution due to baryonic mass concentration of the central galaxy, the halo profile, effects due to the miscentering of the profile, and a contribution from the large scale structure of the universe. The proper treatment for each of these effects will be discussed in detail in the [chapter 4](#), but all of them will always be modelled into a surface distribution Σ and into effect by the equation above (3.33).

Part II

Application

Methodology

WE FINALLY ARRIVE AT THE PRACTICAL implementation of our acquired knowledge of galaxy systems and gravitational lensing - specifically on the aspect of dominance of the central galaxy with respect to the other galaxies in the central region. The main goal of this work is look for correlations between the *magnitude gap* and other physical observables of galaxy systems available with our data, described below: the system mass, NFW concentration parameter, luminosities, and mass-to-light ratios.

In order to measure the mass distribution of the systems, we employ weak gravitational lensing shear measurements, as discussed in the section *Parametric Modelling* of [chapter 3](#). The effect of weak gravitational lensing is, however, subtle and dominated by the noise of intrinsic ellipticities. In fact, the typical intrinsic ellipticity of galaxy images is of order $\epsilon \sim 0.3$. To achieve a useful measurement of γ on the scales we need then, that of one magnitude lower or less, we must achieve a high number of galaxies per image area to use as background sources, and average their tangential ellipticities in radial bins to estimate the distribution of the shear, raising our signal above the noise from intrinsic ellipticity dispersion.

It has been shown [[Bartelmann and Schneider, 2001](#), [van Waerbeke, 2000](#)] that the noise of weak lensing measurements scales as the inverse of \sqrt{N} , with N representing the number of galaxies with measured ellipticities:

$$\sigma_{\epsilon}^2 \propto \frac{\langle \epsilon^s (\epsilon^s)^* \rangle}{N}. \quad (4.1)$$

On the other hand, the observables we want to correlate to

probe aspects of the history of mass assembly of clusters and groups are also subject to large intrinsic scatters. To improve our situation in both fronts we can add signal from different systems to calculate average properties that are relevant to particular populations, which may lower the average signal per cluster but can also remove biases due to the triaxiality of clusters relative to the line of sight, and contamination by the large scale structure.

The approach taken by this work to cope with these recurrent SNR in lensing studies is to combine subsets of galaxy systems into modelled halos, to increase the number of galaxies used as source, and average out effects of projection, alignments and intrinsic scatters. This method is usually called *stacking* or *cross-correlation lensing* [Johnston et al., 2007], and this chapter describes both the data used, and the steps to be taken in both preparing and applying this method into the necessary details.

The results of any preliminary calculations will be displayed along this chapter, whereas the main results for the measured shear, masses, mass concentrations and M/L ratios will be left to the [chapter 5](#) since they constitute the main objective of this work.

4.1 *Data*

The data used in this work comes primarily from two different surveys: the SDSS DR8 redMaPPer catalogue of galaxy clusters by Rykoff et al. [2014] and the CFHT Stripe-82 survey [Moraes et al., 2014]. The Stripe-82 is an equatorial region about 2° wide in the latitude direction between $-40^\circ < \text{RA} < 60^\circ$ which has been extensively investigated by not only SDSS, providing spectroscopy, but also several other surveys, such as Viero et al. [2014], LaMassa et al. [2013], Durret et al. [2014]. The cs82 was specifically designed to take profit of the synergies in this abundance of data.

The main goal of the cs82 collaboration was to measure *cosmic shear*, a large scale structure effect of gravitational lensing that can be used to map the distribution of matter in the universe, and as described in the last section of [chapter 1](#), constrain cosmological parameters. Together with the cluster catalogue provided by

redMaPPer, it can also be used to study a large number of galaxy systems at once.

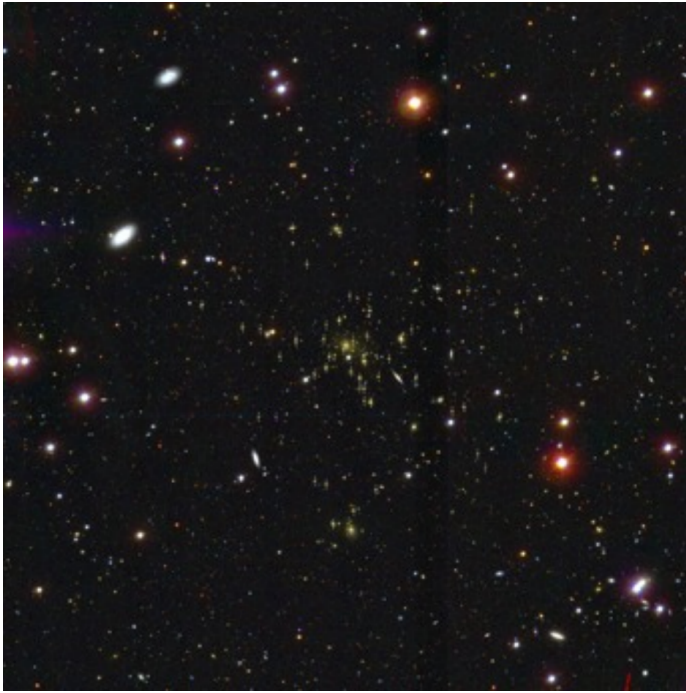


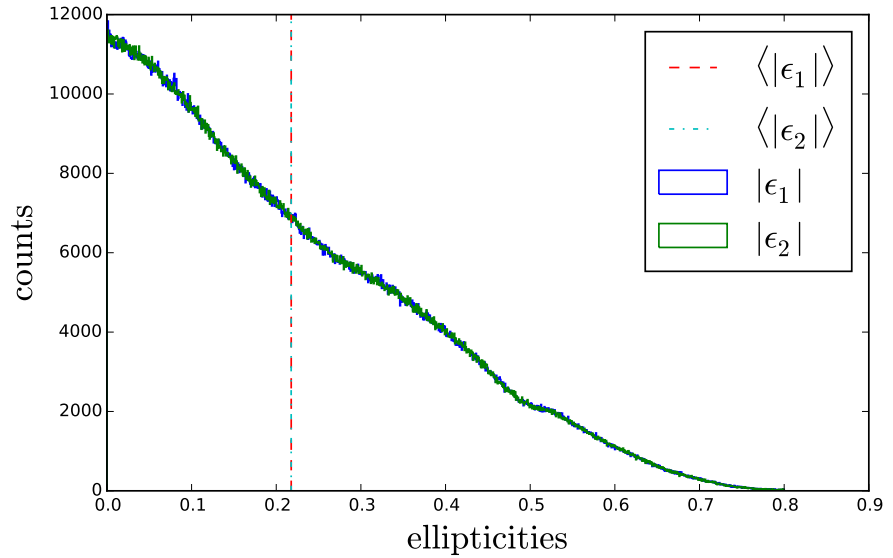
Figure 4.1: The galaxies in the centre of this optical image are an example of galaxy cluster as imaged by SDSS, displaying the characteristic yellowish hue of elliptical galaxies. *Source: SDSS / Alexie Leauthaud CS82 presentation*

The cs82 by itself consists of 173 images in the CFHT y' (\sim SDSS i) band, with the MegaCam instrument a 1deg^2 field of view camera with $21,000 \times 21,000$ pixels, resulting in an angular scale of 0.187arcsec/pixel . The completeness magnitude limit achieved was $m_i < 24$, with a median seeing of $\sim 0.6''$. The total effective area after masking and de-overlapping the images corresponds to about 124deg^2 of the sky. The classification and measurements of shapes of objects has been done by the LensFit algorithm [Miller et al., 2007, Kitching et al., 2008, Miller et al., 2013], and the details of the calibration and its systematics are discussed in Erben et al. [2013]. In this work, all objects with magnitudes $i_{AB} < 23.5$, $w > 0$ and FITCLASS = 0¹ are used. This magnitude is defined as a safe limit to guarantee homogeneity for all the 173 tiles. Together, this criteria results in a total of 4,450,478 galaxies, and the average galaxy density per image area is $\sim 10\text{gal/arcmin}^2$.

The photometric redshifts for the galaxies to be used in weak lensing analysis cannot be taken from the cs82 directly, as it consists of a single band survey, but were then taken from crossing data tables from other surveys: Reis et al. [2012], and

¹ FITCLASS is a star/galaxy identification parameter where 0 corresponds to galaxies and 1 corresponds to stars.

Figure 4.2: Distribution of ellipticities in the x, y coordinate frame of the CS82 survey, as determined by LensFit. The dashed line is the average in both ellipticity directions.



one provided by the cs82 based on [Brammer et al. \[2008\]](#).

The **red-sequence Matched-filter Probabilistic Percolation (redMaPPer)** algorithm for cluster finding, on the other hand, is a photometric cluster finding algorithm based on the optimised richness estimator λ of [Rykoff et al. \[2012\]](#), which is designed to have minimum scatter with cluster masses. The redMaPPer algorithm, a descendant of the maxBCG algorithm [[Koester et al., 2007](#)], identifies galaxy clusters as overdensities of *red-sequence galaxies* around central galaxy candidates. At first, it uses learning techniques on spectroscopic training sets to characterise the evolution of the red sequence as a function of redshift. The algorithm then uses the resulting red sequence model, together with a radial scale filter and a luminosity function filter based on the Schechter function (eq. 2.28) to estimate the probability that any given galaxy belongs to any given cluster. The cluster richness is defined as the sum of the probabilities of galaxies considered, as the expected value of the number of galaxies in the cluster,

$$\lambda := \sum_i p_i. \quad (4.2)$$

In addition, by identifying a red-sequence for each cluster, it can estimate cluster photometric redshifts by simultaneous fitting all possible member galaxies to its red-sequence model. The radial scale filter also defines a percolation radius r_c that is related to the

obtained richness λ by

$$r_c = 1\text{Mpc} \times \left(\frac{\lambda}{100} \right)^\beta, \quad (4.3)$$

with $\beta = 0.2$ [Rykoff et al., 2014, 2012].

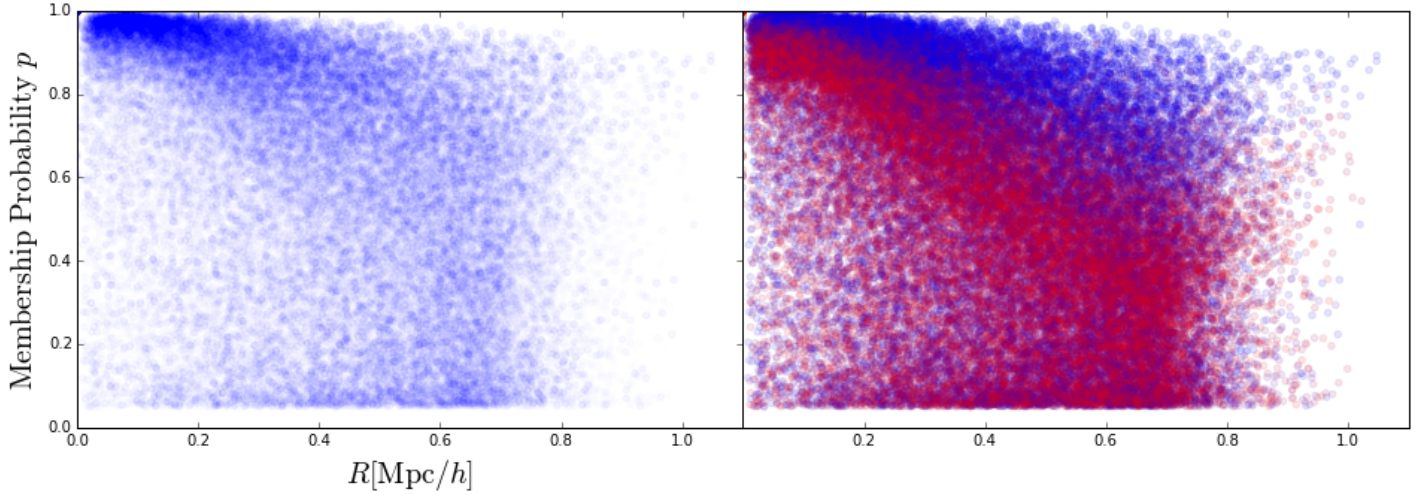


Figure 4.3: Probability mass function for all galaxies identified by redMaPPer as possible members of a system, by radius. We can see that outer radii galaxies have a wider distribution. In the left panel, point transparency was adjusted to reflect galaxy brightness, so that fainter galaxies appear as faint points (in log scale). On the right, the blue/red points indicate lower/higher cluster redshifts respectively. At high redshifts, probabilities tend to be lower.

Although the authors emphasise that the r_c is not directly related to the virial radius, we use it to define the central region of the system as $r < r_c/2$, which translates into about $\sim r_{200}/3$ [Rykoff et al., 2012]. This is a more inclusive definition, since it defines less volume to draw nearby galaxies to compute magnitude differences, however that smaller region will also diminish significantly the population with $\Delta M > 0$, where the central galaxy is not the brightest (cf. Fig. 4.4).

4.2 Absolute Magnitude Calculations

To describe our whole procedure carefully, we start at the very first first step: to calculate absolute magnitudes for each galaxy from the redMaPPer catalogue. Since the redMaPPer galaxy magnitude data were already de-reddened, we can calculate the absolute magnitudes through the Distance Modulus μ as a function of the luminosity distance (eq 1.25):

$$\mu = 5 \log \left(\frac{D_L}{10\text{pc}} \right) = m_i - M_i - k_i, \quad (4.4)$$

where the K-correction, given by O'Mill et al. [2011] for the

band i filter magnitude, using the other filters g , r , and the redshift z is:

$$k_i = [0.538(g - r) - 0.075]z + [-0.027(g - r) - 0.120], \quad (4.5)$$

To estimate the uncertainties, we follow simple uncertainty propagation ²

² which results in

$$\frac{dk_i}{dg} = 0.538z - 0.027$$

$$\frac{dk_i}{dr} = -0.538z + 0.027$$

$$\frac{dk_i}{dz} = 0.538(g - r) - 0.075$$

$$\delta_{k_i}^2 = \left(\delta_g \frac{dk_i}{dg} \right)^2 + \left(\delta_r \frac{dk_i}{dr} \right)^2 + \left(\delta_z \frac{dk_i}{dz} \right)^2 \quad (4.6)$$

The uncertainty of the distance modulus is likewise given by:

$$\delta_\mu = \delta_z \frac{d\mu}{dz}$$

For which we use a numerical derivative process to calculate $\frac{d\mu}{dz}$. Finally, with

$$\delta_{M_i}^2 = \delta_\mu^2 + \delta_{k_i}^2,$$

the absolute magnitude results are ready.

4.3 Estimation of Magnitude Gaps

In possession of the absolute magnitudes, we turn to the estimation of the magnitude gaps. Here, we must start by two important remarks that will shape this discussion: first the redMaPPer algorithm does not always identify the central galaxy as the brightest. Hence, we refer to the central galaxy as CG, instead to the literature usual BCG, and the magnitude gaps are calculated with respect to the brightest non-centre galaxy ($\Delta M_{1-2} := M_{CG} - M_{BNCG}$) or the third brightest non-centre galaxy ($\Delta M_{1-4} := M_{CG} - M_{3BNCG}$)³, depending of the adopted selection criterion.⁴

³ These will lead to *negative* gaps for usual cases, where the central galaxy is the brightest, and positive for those which it is not.

⁴ As previously stated, we restrict our calculation of magnitude gaps to the inner region of the group/cluster as defined by a circle with $r < 1/2R_c$, the effect of the inner region defining radius is discussed at the end of this section.

Secondly, the probabilistic nature of the redMaPPer catalogue puts an obstacle to our direct assessment of the cluster magnitude gap: since we do not know with certainty which galaxies are and which are not system members, we cannot directly calculate the magnitude gap by just subtracting the central and BNCG and 3BNCG absolute magnitudes, subject only to instrumental error.

We can, however, calculate *expected values* of magnitude gaps, by simply computing the *probability mass distribution* of the galaxy catalogue of each system. To do so, we have employed two different methods: first, a computational bootstrapping, creating copies of each cluster that reproduced cluster probability mass function, and second, the direct calculation of probabilities for possible magnitude gap values.

To calculate these expected values computationally, we can, for each cluster, create a number of realisations to obtain the expected magnitude differences. We then order galaxies in each copy by increasing magnitude, and select the first and third as the BNCG and 3BNCG for each copy. The expected value of the magnitude gap is given by the weighted average of the n realisations.

$$E(\Delta M_{1-2(4)}) = \frac{\sum_n [M_{CG} - M_{(3)BNCG,n}] w_n}{\sum_n w_n}, \quad (4.7)$$

where the weights are given by

$$w_n = \frac{1}{(\delta \Delta M_n)^2}, \quad (4.8)$$

and the uncertainty due to uncertainties in magnitude measurements is

$$\langle \delta \Delta M \rangle = \frac{1}{\sqrt{\sum_i w_i}}. \quad (4.9)$$

with $\delta \Delta M_i = \sqrt{\delta M_{cg}^2 + \delta M_{gal}^2}$.

The error due to the uncertainty of memberships, likewise, can be estimated by calculating the weighted standard deviation of the mean of the n realisations.

We have calculated $\Delta M_{1-2(4)}$ and the respective probability distributions through the bootstrap method by using 2000 realisations, after checking for convergence by inspecting the successive results as a function of n . However, this Monte Carlo approach has proven to be excessively time-consuming and because of that not easily adaptable. While looking for a faster way to calculate these values we have derived exact probability calculations which can be used to obtain the expected values.⁵

First, consider a table of all galaxies inside the inner region of the system except the central, with N redMaPPer-identified

⁵ In practice, the bootstrapping method helped us check the validity of the calculations both to the expected values and the variances.

possible members, so that their membership probabilities are given by $\vec{p} = p_1, p_2, p_3 \dots$ as ordered by decreasing brightness (increasing absolute magnitude). Then, the probability of the first galaxy to be the brightest in this group is just p_1 as no other galaxy can possibly be brighter than it, So that $p_1 = P_1$ is also the probability of the magnitude gap ΔM_{1-2} to be $M_{CG} - M_1$. Now, for the second galaxy we need to ensure that the first is not present $(1 - p_1)$ and that the second is, that is, $(1 - p_1)p_2$. By simple iteration, the probability of the n -th galaxy of being the BNCG is given by:

$$P_n = p_n \prod_{i=2}^{n-1} (1 - p_i). \quad (4.10)$$

Now, for ΔM_{1-4} , the reasoning is just slightly more complicated. The first possible galaxy to be counted is the one with probability p_3 ; for it to be the third brightest in this set, all before must be galaxies of the system and also itself, so the probability is $P_3 = p_1 p_2 p_3$. The fourth galaxy will be the third brightest with the remaining probability $(1 - P_3)$ and its own probability of being a member p_4 , that is $P_4 = (1 - P_3)p_4$. The fifth will follow suit: the remaining probability is now $(1 - P_3 - P_4)$ and its own p_5 . So the general formula will be

$$P_n = p_n \left(1 - \sum_{i=3}^n P_i \right). \quad (4.11)$$

Collecting these results the expected values are the sum weighted by individual probabilities for each possible gap:

$$E [\Delta M_{1,2(4)}] = M_{CG} - \sum_{n=1(3)}^N P_n M_n, \quad (4.12)$$

and the errors adopted follow directly from the definition of the variance also,

$$\text{Var} [\Delta M_{1,2(4)}] = E [(\Delta M_{1,2(4)})^2] - [E (\Delta M_{1,2(4)})]^2. \quad (4.13)$$

These calculations were successfully compared to the bootstrapping approach, and resulted in total fractions of

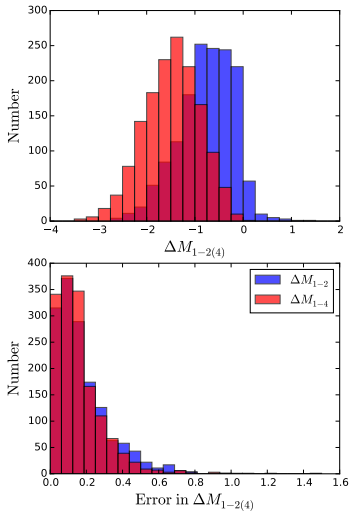


Figure 4.4: Distributions for the calculated magnitude gaps and errors for ΔM_{1-2} and ΔM_{1-4} .

$\sim 1.6(2.4)\%$ clusters as optical fossil candidates according to $\Delta M_{1-2(4)}$ (Fig. 4.4). On the other hand, $7.3(0.13)\%$ of the systems had positive $\Delta M_{1-2(4)}$ values, that raises the question on whether these systems have been incorrectly centred by the algorithm or if these brighter non-CG galaxies were incorrectly classified as highly probable cluster members.

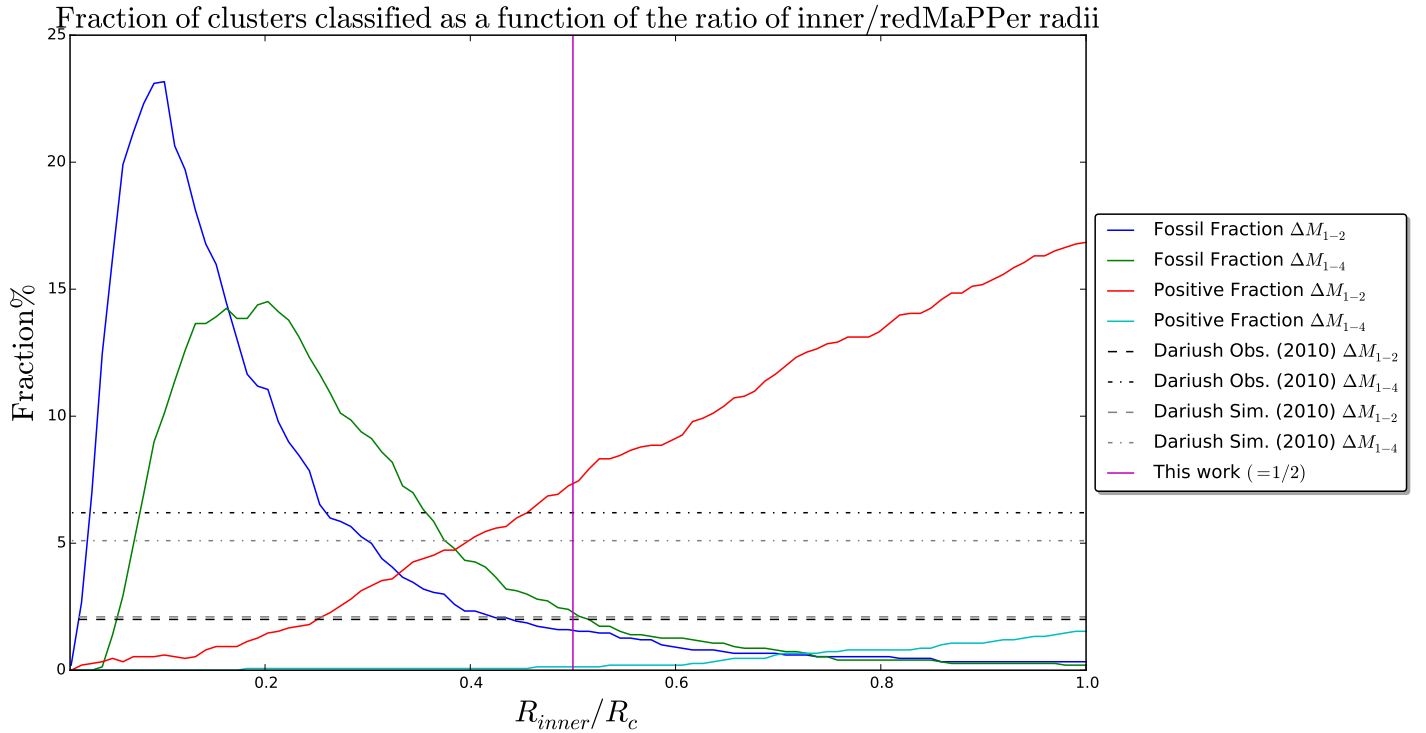


Figure 4.5: Fractions of clusters by particular magnitude gaps. Positive magnitude gaps generally increase with radius, whereas for the fossil fraction increases with smaller radii, which justifies calling smaller radius a less strict definition.

To assess the effect of the definition of the inner radius, we have calculated the fraction of the clusters classified as fossils with both ΔM_{1-2} and ΔM_{1-4} criteria, and the calculated fractions by [Dariush et al. \[2010\]](#) both from observations and simulations and the the fraction of clusters with a positive magnitude gap, which may include systems where the CG was misidentified. Because of this, we opt to not use the positive gap clusters in further analysis of this work.

4.4 Parametric Modelling of Mass Distributions

The NFW profile (eq. 2.6) can be written as a function of two parameters, the concentration c_N and the mass M_c for a given

redshift z by first rewriting it into

$$\rho_{NFW}(r) = \frac{\delta_{NFW} \rho_{crit}(z)}{(r/r_s)(1 + r/r_s)^2}, \quad (4.14)$$

where we recall that the critical density of the universe at a certain redshift is given by $\rho_{crit} = \frac{3H^2(z)}{8\pi G}$, and we have defined the scale radius as $r_s = r_c/c_N$.

Then, the δ_{NFW} parameter can be related to the cluster overdensity Δ_c and the concentration by:

$$\delta_{NFW} = \frac{\Delta_c}{3} \frac{c_N^3}{\ln(1 + c_N) - c_N/(1 + c_N)}, \quad (4.15)$$

and finally the scale radius is given by proxy, as the collapsed radius as a function of the mass and redshift by

$$r_c(z, M_c) = \left[\frac{3M_c}{4\pi \Delta_c \rho_{crit}(z)} \right]^{\frac{1}{3}}. \quad (4.16)$$

For this work, the usual $\Delta_c = 200$ has been used to facilitate comparison to the existing literature and the masses and concentrations so defined are referred to as M_{200} and c_{200} , respectively.

The projected mass density will be given by 2.34, for which the NFW profile yields analytic solutions [Wright and Brainerd, 2000]. For a given collapsed mass, concentration, and redshift, we have

$$\Sigma_{NFW}(r|M_c, c_N, z) = 2r_s \delta_{NFW} M_{200} \Sigma_{X,NFW}(r/r_s) \quad (4.17)$$

where the shape of the profile $\Sigma_{X,NFW}$ in terms of the rescaled dimensionless radius is given by

$$\Sigma_{X,NFW}(x) = \begin{cases} \frac{1}{(x^2-1)} \left[1 - \frac{2}{\sqrt{1-x^2}} \operatorname{arctanh} \sqrt{\frac{1-x}{1+x}} \right] & (x < 1) \\ \frac{1}{3} & (x = 1) \\ \frac{1}{(x^2-1)} \left[1 - \frac{2}{\sqrt{x^2-1}} \operatorname{arctan} \sqrt{\frac{x-1}{1+x}} \right] & (x > 1) \end{cases} \quad (4.18)$$

4.5 *The Effect of Miscentering*

When using parametric profiles to model a combination of spherically symmetric matter distributions, it is important to evaluate the correct centre position of the profiles. It is known that some fraction of the CGs may be offset from the true centre of the gravitational potential it inhabits [Girardi et al., 1997, Krempec-Krygier and Krygier, 1999], and also that cluster finder algorithms may identify a wrong galaxy as the CG [Johnston et al., 2007]. When we combine several clusters, the effect of this *miscentering* is to produce lower levels of shear in the inner radii, as some centres will be at a radius $R > 0$, and their shear maps will shuffle the ensemble average, which may bias the results towards lower masses [Johnston et al., 2007].

If the $2D$ offset in the lens plane of a single profile is given by R_{off} , the azimuthally averaged surface profile will be given by a shift of the centre and an integral around the correct centre as [Yang et al., 2006]:

$$\Sigma^{off}(R|R_{off}) = \frac{1}{2\pi} \int_0^{2\pi} d\theta \Sigma \left(\sqrt{R^2 + R_{off}^2 - 2RR_{off}\cos(\theta)} \right). \quad (4.19)$$

There will be, however, a distribution of profile offsets when combined in cross-correlation lensing. The distribution of these offsets have been analysed by Johnston and can be modelled as

$$P(R_{off}) = \frac{R_{off}}{\sigma_{off}^2} \exp \left[-\frac{1}{2} \left(\frac{R_{off}}{\sigma_{off}} \right)^2 \right], \quad (4.20)$$

where the parameter σ_{off} is the peak of the distribution.

The resulting mean surface mass profile for miscentered combinations of clusters can be written then as

$$\Sigma^s(R) = \int_0^\infty dR_{off} P(R_{off}) \Sigma^{off}(R|R_{off}). \quad (4.21)$$

Since this work will deal with likelihood fits of this profile using MCMC - which calculates many candidates for model parameters and compares to the data, it is worthy to spend some

time considering the computational cost of calculating the model for a set of parameters into some radial bins, since the model will be calculated over and over many times.

The expression above, when combined with the differential surface mass density $\Delta\Sigma$ contains a triple integral

$$\begin{aligned} \Delta\Sigma(R|M, c_N, z) = & \\ & \frac{1}{\pi R^2} \int_0^R \int_0^\infty \int_0^{2\pi} r dr dR_{off} d\theta P(R_{off}) \Sigma \left(\sqrt{r^2 + r_{off}^2 - 2r r_{off} \cos(\theta)} \right) \\ & - \int_0^\infty \int_0^{2\pi} dR_{off} d\theta P(R_{off}) \Sigma \left(\sqrt{r^2 + r_{off}^2 - 2r r_{off} \cos(\theta)} \right), \quad (4.22) \end{aligned}$$

which has to be calculated for each point on the parameter space that the MCMC evaluates times the number of radial bins, so it can be interesting to transform this into a look-up table to speed up calculations. This can be done by using the previously defined rescaled radius $x = r/r_s$ to define the rescaled off-centring parameter as $\xi_{off} = \sigma_{off}/r_s$. We can then write

$$P_X(x_{off}) = \frac{x_{off}}{\xi_{off}^2} \exp \left[-\frac{1}{2} \left(\frac{x_{off}}{\xi_{off}} \right)^2 \right], \quad (4.23)$$

and with this and Σ_X , as, for example, defined in equation 4.18 we arrive at

$$\begin{aligned} \Delta\Sigma(R|M, c_N, z) = & \\ & \frac{2r_s \delta_{NFW} M_c}{\pi R^2} \int_0^x \int_0^\infty \int_0^{2\pi} x dx dx_{off} d\theta P_X(x_{off}) \Sigma_X \left(\sqrt{x^2 + x_{off}^2 - 2x x_{off} \cos(\theta)} \right) \\ & - \int_0^\infty \int_0^{2\pi} dx_{off} d\theta P_X(x_{off}) \Sigma_X \left(\sqrt{x^2 + x_{off}^2 - 2x x_{off} \cos(\theta)} \right), \quad (4.24) \end{aligned}$$

where the integrals can be pre-calculated as a function of x , saved and used through interpolation by FITPACK [Cline, 1974] or other high-performance interpolation library.

4.6 Contributions from the Large-Scale Structure

As previously argued, the NFW profile is expected to be a good representation of halo profiles only to a certain scale, at most $\sim 2\text{Mpc}/h$. To go to further out radii, the contribution of the large scale structure must to the mass profile be accounted for. We have already derived the 2-halo contribution as a function of the linear bias and the matter-matter two-point correlation function (eq. 2.24). Now we proceed to transform the radial matter density enhancement into a projected quantity, following the steps of Johnston et al. [2007].

First, the two halo mass profile term can be written as

$$\rho_{2h} = b(\nu) \overbrace{\Omega_m \rho_{c,0} (1+z)^3}^{\bar{\rho}_m(z)} \xi^L(r, z). \quad (4.25)$$

The matter-matter correlation function at redshift z can be written in terms of the growth function (eq. 1.31), σ_8 (eq. 2.8) and ξ_{mm} at redshift $z = 0$ as

$$\xi^L(r, z) = D(z)^2 \sigma_8^2 \xi_l [(1+z)r], \quad (4.26)$$

where $\xi_l(r)$ is the correlation function at redshift zero, that we calculate from the linear power spectrum as in eq. 1.40.

Now, to calculate the projected density, if we define

$$B(z, M) := b(z, M) \Omega_M \sigma_8^2 D(z)^2, \quad (4.27)$$

we can write the projected 2-halo term as

$$\Sigma_{2h}(R) = B(z, M) \Sigma_l(R), \quad (4.28)$$

where the projected mass profile due to the large scale structure is calculated as in the equation 2.34

$$\Sigma_l = (1+z)^2 \rho_{c,0} W((1+z)R), \quad (4.29)$$

with

$$W(R) := \int_{-\infty}^{\infty} dy \xi_l(\sqrt{y^2 + R^2}). \quad (4.30)$$

Again, it has proven useful to pre-calculate the function $W(R)$ to avoid repeating the integral when using the fitting procedure.

The source of our power spectrum for calculating the contributions from the large scale structure is CAMB, using the parameters given in table 1.1 by the Planck 2015 column.

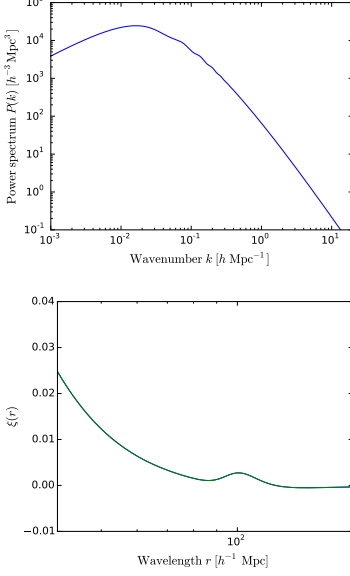


Figure 4.6: **Upper:** CAMB generated power spectrum at redshift zero used for this work, using Planck 2015 data. **Lower:** The respective matter-matter correlation function, zoomed into the characteristic acoustic oscillation peak.

4.7 The Full Model

It is argued [Gavazzi et al., 2007] that the baryonic mass of the central galaxy is not accounted for in the dark-matter halo. Although the contribution could be modelled in a number of ways, e.g. by using a de Vaucouleurs profile, its effects are only significant on very small scales, which cannot be properly constrained in weak-lensing only studies. Therefore, we have chosen to test a model the central mass as in Johnston et al. [2007] and Shan et al. [2015], as a point mass, with lensing signal

$$\Delta\Sigma_{CG}(R) = \frac{M_0}{\pi R^2}. \quad (4.31)$$

Collecting this together with those for the correctly centred profile, the miscentered profile and the contribution from the large scale structure, the surface mass density $\Delta\Sigma(R) = \Sigma_{crit}\gamma(R) = \bar{\Sigma}(r < R) - \Sigma(R)$ in a modelled halo of stacked systems with NFW profiles is given by the sum of their contributions:

$$\Delta\Sigma = \frac{M_0}{\pi R^2} + p_{cc}\Delta\Sigma_{NFW}(R) + (1-p_{cc})\Delta\Sigma_{NFW}^{off}(R) + \Delta\Sigma_{2ht}(R), \quad (4.32)$$

where the terms in the sum can be enumerated as:

- The baryonic component of central galaxy mass
- The NFW profile for the fraction of clusters correctly centred
- The miscentered NFW profile
- The large scale structure contribution.

This is a 5 parameter model, with M_0 , M_{200} , c_N , P_{cc} , and σ_{off} as adjustable parameters, where the last two are normally considered *nuisance parameters* and the M_0 can be either nuisance

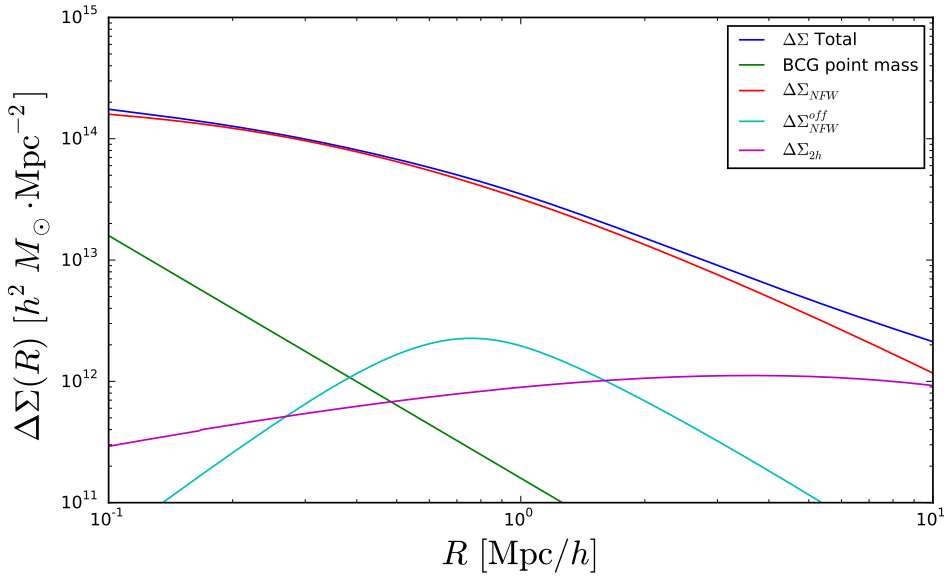


Figure 4.7: Test of the full model showing the individual contributions of the miscentered clusters, the correctly centred ones, the two-halo term, and the baryonic mass of the central galaxy.

or used to understand differences in the central galaxy of the systems.

To exemplify the contributions of each term to the final profile, we have plotted them for a typical set of clusters of mass $M_c = 10^{14}M_\odot$, $c_N = 3$, with $p_{cc} = 0.9$, $\sigma_{off} = 0.42/h\text{Mpc}$ and $M_0 = .5 \times 10^{12}M_\odot$ (Fig. 4.7) and, as validation, the results of its computational implementation were contrasted to examples in the literature [Ford et al., 2015, Johnston et al., 2007], yielding satisfactory results.

4.8 Signal Measurement

As we claimed in the first paragraphs of this chapter, in cross-correlation lensing analysis, the signal is measured out of many stacked systems and in order to have more homogeneous subgroups, we must define suitable groups of systems to stack. Since the cluster observables may depend on the redshift and the cluster mass profile is strongly correlated with richness, these are the two quantities that must be taken into account first. Then, we further subdivide these groups into final stacks based on magnitude gaps as we want to correlate populations of different gaps with the other observables we have access to.

We have, then, divided the full 1502 cluster sample into a total of 18 categories⁶, with 3 redshift divisions, $([0.15, 0.4], [0.4, 0.6],$

⁶ for each selection criterion: ΔM_{1-2} or ΔM_{1-2}

Table 4.1: Number of systems in each stack by ΔM_{1-2} .

	ΔM_{1-2}	$.15 < z < 0.4$	$.4 < z < .6$	$.6 < z < .75$
$\lambda > 30$	< -1.5	7	12	7
	$[-1.5, 0.75]$	19	37	61
	$[-0.75, 0]$	27	53	74
$\lambda < 30$	< -1.5	21	39	231
	$[-1.5, 0.75]$	64	134	181
	$[-0.75, 0]$	85	197	318

Table 4.2: Number of systems in each stack by ΔM_{1-4} .

	ΔM_{1-4}	$.15 < z < .4$	$.4 < z < .6$	$.6 < z < .75$
$\lambda > 30$	< -2	9	17	8
	$[-2, -1]$	33	59	92
	$[-1, 0]$	13	32	56
$\lambda < 30$	< -2	36	455	56
	$[-2, -1]$	109	233	340
	$[-1, 0]$	32	102	191

and $[0.6, 0.75]$) and two richness divisions ($30 < \lambda < 130$ and $15 < \lambda < 30$) and finally, each of these bins are further divided into 3 magnitude gap classes, taking into account both different methods previously suggested ($\Delta M_{1-2(4)}$ can be seen in figure 4.8 & table 4.1(4.2)). Due to the low number of systems when considering these many subdivisions, we could not separate fossils from each subgroup, so we relax the requirement to a smaller magnitude gap to have qualitative comparison of the physical observables against the size of the gap in general.

- For ΔM_{1-2} we have divided into $\Delta M_{1-2} < -1.5$ (High Delta), $-1.5 < \Delta M_{1-2} < 0.75$ (Medium Delta), and $-0.75 < \Delta M_{1-2} < 0$ (Low Delta).
- For ΔM_{1-4} we have divided into $\Delta M_{1-4} < -2$ (High Delta), $-2 < \Delta M_{1-4} < -1$ (Medium Delta), and $-1 < \Delta M_{1-4} < 0$ (Low Delta).

Having separated the stacks of objects, the weak lensing shear signal can be measured by averaging the tangential ellipticity in concentric rings around cluster centres. The averaged tangential ellipticities, however, do not trace the shear directly, but actually the reduced shear, as we have previously discussed (eq. 3.22). So, if e_{ij} is the ellipticity of the i -th galaxy around the j -th cluster, as shown by Mandelbaum [2006], a proper estimator for $\Delta\Sigma$ calculated from the weighted average of ellipticities and identical

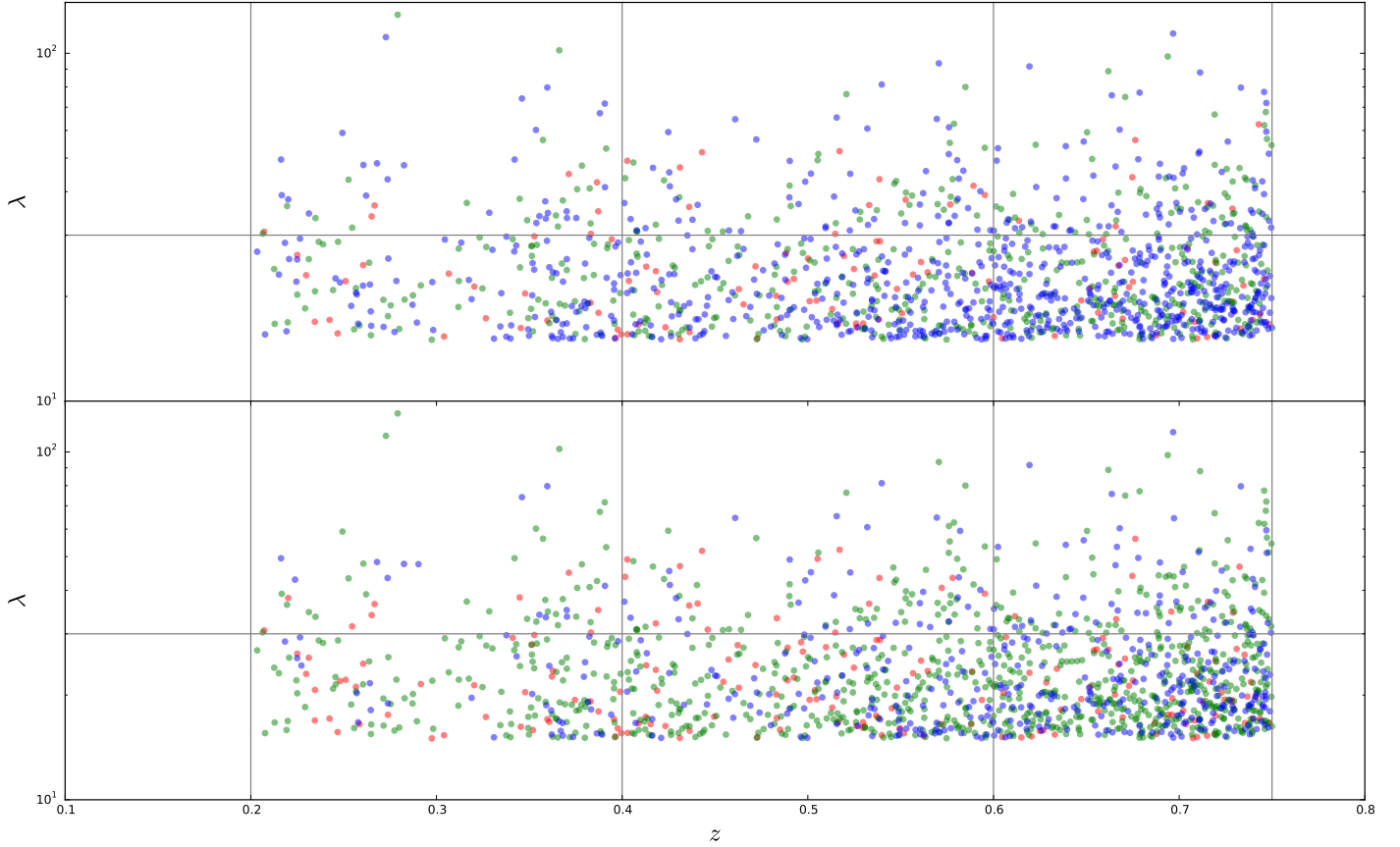


Figure 4.8: The division of the full sample into sub-samples of coherent richness and redshifts are then divided into classes of magnitude gaps. On the course of this work, we display consistently smaller gaps as blue, larger gaps as red and intermediate as green. Richness will always be higher in upper panels and redshift higher on the right.

halos has a second order contribution

$$\widehat{\Delta\Sigma} = \Delta\Sigma + \Delta\Sigma \Sigma \mathcal{L}_z \quad (4.33)$$

with

$$\mathcal{L}_z = \frac{\langle \Sigma_{crit}^{-3} \rangle}{\langle \Sigma_{crit}^{-2} \rangle} \quad (4.34)$$

however, as argued by [Ford et al., 2015] the effect of the second term is only barely noticeable, and only of $\sim 10\%$, in the innermost radii, because the weak lensing regime starts to break down and then the approximation $g \approx \gamma$ is no longer valid. As we do not have, in our data, enough signal to discriminate to that level, specially in the inner regions, we have chosen to estimate the signal from the data following a simpler model as Shan et al. [2015]:

$$\widehat{\Delta\Sigma} = \frac{\sum_{l,s} w_{l,s} e_t \Sigma_{crit;l,s}}{\sum_{l,s} w_{l,s}}. \quad (4.35)$$

⁷ Attention must be given to units. Since the angular distances will be given in Mpc and we want the result in solar masses, we use $G = 4.302 \times 10^{-9} M_{\odot}^{-1} (\text{km/s})^2 \text{Mpc}$ and $c = 3 \times 10^5 \text{km/s}$.

⁸ As suggested by a member of the collaboration in private communication.

with weights given by $w_{l,s} = w_s \Sigma_{crit;l,s}$ ⁷ where w_s is a Lensfit weight due to intrinsic and measurement quality scatter.

The procedure now is to first set apart a region of $10 \text{Mpc}/h$ around each cluster from which we draw background objects, defined by having a redshift $z_s > 1.1z_d + 0.15$ ⁸, then to calculate Σ_{crit} for each pair galaxy-background source. The ellipticities for each source are then transformed from the $e1 = \text{Dec}$, $e2 = -\text{RA}$ coordinate system into polar coordinates around the cluster centre, which gives us tangential and cross ellipticities of the sources.

We now have $\epsilon_t \Sigma_{crit}$ for each lens-source pair, and proceed to stack them combined into 6 logarithmically spaced annuli determined in physical radii. We have chosen the number of radial bins to be 6 by testing many configurations - most of the problems encountered while trying more radial bins is due to difficulty in innermost radii. The annuli that have been defined are those between the limits $\sim [0.11, 0.23, 0.48, 1.00, 2.09, 4.36, 9.12] h^{-1} \text{Mpc}$.

Each of these radial bins have its $\widehat{\Delta\Sigma}$ measured by eq. 4.35, which count as a single data point for the stack at the bin centre. The resulting galaxy densities show some decrease with radius, which could denote contamination at inner radii, or border effects. The effect of contamination by cluster or foreground galaxies as background should diminish the signal, as they are not affected by lensing by stack members. We have, however, tested deeper cuts, such as $z_s > 1.1z_d + 0.25$, all of which resulted only in weaker statistics.

We have also measured the $\widehat{\Delta\Sigma}_{\times}$ cross terms concomitantly to check for systematic errors, alignments and miscentering effects, as cross ellipticities are not expected from radial mass distributions [Schneider, 2006].

4.9 *Monte Carlo Markov Chain Fitting of the Signal*

After obtaining the data signal, as described above, we have turned to investigating the probability distribution of the model parameters that describe the data for each of the 36 stacks.

Generally, the posterior probability distribution of the parameters is proportional to the likelihood and the prior as

$$P(\Theta|\Delta\Sigma) \propto \mathcal{L}(\widehat{\Delta\Sigma}|\Theta; \bar{z}) \times P(\Theta), \quad (4.36)$$

where $\Theta = M_{200}, c_{200}, p_{cc}, \sigma_{off}, M_0$ are the parameters.

The parameters $M_c, c_N, M_0, \sigma_{off}$, and p_{cc} have been modelled to have multivariate Gaussian likelihoods for a given average redshift of the ensemble \bar{z} . It is computationally practical to use the logarithm of the likelihood (*log-likelihood*), which is given by

$$\ln [\mathcal{L}_{NFW}(M_c, c_N, \bar{z})] = -\frac{1}{2} \sum_i \frac{\left[\widehat{\Delta\Sigma}(R_i) - \Delta\Sigma_{NFW}^s(R_i | M_c, c_N, \bar{z}) \right]^2}{\sigma_{\Delta\Sigma_i}^2}. \quad (4.37)$$

To that we must add the logarithm of functions defining our priors. We have used flat, or uninformative, priors to constrain the space of parameters into acceptable values, which are given in table 4.3. The choice of flat priors, which differs from current practice on the literature [Johnston et al., 2007], was taken not only for simplicity, but also to investigate both the model and the data - in chapter 6, we discuss the future application of more restrictive priors.

These flat priors can be, in practice, implemented as functions that return zero inside the permissible interval and $-\infty^9$ outside, constraining the likelihood into these regions.

The logarithm of the posterior probability is then given by

$$\ln [P(\Theta|\Delta\Sigma)] = \ln \left[\mathcal{L}_{NFW}(\widehat{\Delta\Sigma}|\Theta; \bar{z}) \right] + \ln [P(\Theta)], \quad (4.38)$$

which can then be probed by Monte Carlo methods. We use as parameters for the masses $\log M_0$ and $\log M_c$, in practice, as they can span over more than two orders of magnitude, and this prevents some possible computational problems.

To minimise the effect of preconceptions, and to test these models in preparation for future surveys, we have employed three different models to fit the signal by defining the number of free parameters: one full model, leaving all the previously described 5 parameters free, one with $\sigma_{off} = 0.42h\text{Mpc}$, taken from Johnston et al. [2007]¹⁰, and the one with both σ_{off} as before and

⁹ Modern high-level programming languages, such as PYTHON 3 normally provide infinite constants that can be used safely.

¹⁰ Johnston et al. [2007] justifies the value for σ_{off} by simulations, taking into account misidentification of central galaxies by the maxBCG algorithm. Whether the same number is applicable to redMaPPer, a direct descendant of maxBCG, is questionable, but is not expected to largely differ in practice.

no baryonic mass of the central galaxy ($M_0 = 0$). Despite using several different models we will not, at this time, present model comparisons using full Bayesian evidences.

Finally, we note that these choices result in a total of 108 fits, but only modestly foreshadow future computational demands, where surveys will probe hundred thousands of clusters (e.g. [Benítez et al. \[2015\]](#)).

Table 4.3: Priors used with the MCMC. When absent, the method is equivalent to a δ_D prior on the exact value.

Parameter	Range
$\log(M_c)$	[10, 16]
$\log(M_0)$	[10, 14]
c_N	[0.1, 20]
p_{cc}	[0, 1]
σ_{off}	[0.1, 0.9]

To probe the posterior probability distributions of the parameters, we have employed `EMCEE` [[Foreman-Mackey et al., 2013](#)], which is a python implementation of [Goodman and Weare \[2010\]](#)'s Affine Invariant Markov chain Monte Carlo ensemble sampler. It defines a set of *walkers* that build Markov chains while updating the proposal distribution depending on results from each other. By doing so, the algorithm can be easily parallelised to improve performance and map the posterior likelihood with lesser steps.

The walkers have been initialised by random choice inside balls around "fiducial" values for each of the parameters. The choice of these values, however, do not compromise the method if we use large enough chains. These initial "fiducial" values were: $\log M_{200} = 14$, $c_{200} = 3$, $p_{cc} = .7$, $\sigma_{off} = .4$, and $\log M_0 = 11$, where the parameters were free, with balls defined as 10% of each value. We have used 256 walkers with 1000 steps, for a total of 256000 *chain links* in the parameter space for each fit. Using a Xeon processor with 12 cores and 32 GiB of RAM, each fit was performed in around 1800 seconds. This highlights the computational cost for future uses, even though there still is plenty of room for improvement in the code.

In order to define a region from the chain from which we draw the mapped likelihood sample, we must define a *burn-in* in the initial section of the chains, to get rid of any influence of the

choice of starting positions of the walkers. We have chosen to discard an overly conservative first 20% of the chains as *burn-in*, which was determined to be enough by inspecting the chains.

4.10 Luminosities

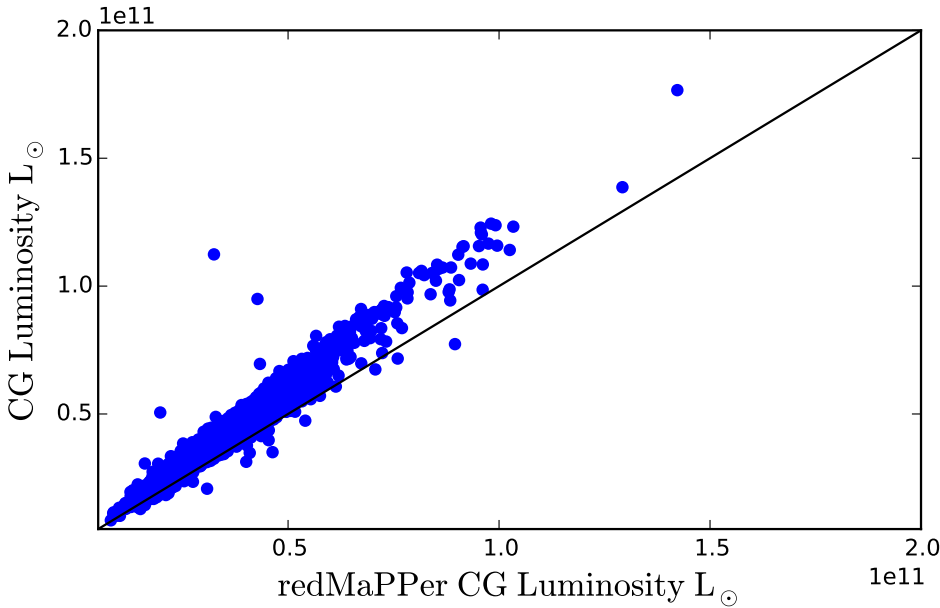


Figure 4.9: The difference between the redMaPPer calculated *i*-band luminosity and the ones calculated by our absolute *i* band magnitudes. The difference occurs because of different luminosity distances owing to different cosmological parameters. This comparison has been used to correct for full cluster luminosities.

Finally, we have attempted to use the luminosity information from the redMaPPer catalogue to add tests we could do to our data. However, measuring precise luminosities is a difficult task, because estimates will strongly depend on distance measures, which are dependent of cosmology. As a highlight of this, the luminosities used in this work, which come from the redMaPPer catalogue, have been compared to luminosities calculated by the absolute magnitudes by

$$L = 10^{-0.4(M_b - M_{b,\odot})} L_{\odot}. \quad (4.39)$$

using table 1.1, in the concordance column, for the cosmological parameters. It was found that they differ on a small multiplicative factor, for which different distance scales can be an explanation (Fig. 4.9). Consequently, the luminosities used in this work, as their derived quantities are to be used only in comparison between different stacks in this work, and not outside this scope.

Results and Discussions

THE RESULTS OF THE WORK PREVIOUSLY DESCRIBED are presented below, first the measurements of the radial averaged ellipticity profiles ($\Delta\Sigma$) and then the parameter posterior distribution estimation through MCMC. These results are divided first by magnitude gap determination method¹ and then into the redshift and richness bins as described in tables 4.1 & 4.2. We have kept the pattern of these tables using in both future tables and figures below the same placement: higher(lower) cells depict higher(lower) richness ensembles and from left to right, increasing redshift bins. As in figure 4.8, we have kept the colour code of larger magnitude gaps as red, medium magnitude gaps as green and small magnitude gaps as blue. After presenting the main parametric results, we discuss the investigation of relationships between obtained parameter distributions.

¹ Either ΔM_{1-2} or ΔM_{14}

5.1 Measurements

We have measured $\Delta\Sigma$ in the 6 previously described physical radial bins, ranging from the inner part of clusters in $\sim 100\text{kpc}$ to their vicinity, as far as $\sim 10\text{Mpc}$. The results are displayed in Figure 5.1 upper and lower panels for ΔM_{1-2} and ΔM_{1-4} respectively. From these plots, we see that not all radial shear measurements scale as the general shape of halo radial profiles we have described in the section *The role of Cosmology in Galaxy systems* of chapter 2, with a steepening slope from the centre to the outer radii. Instead, some radial profiles display drops or steep hikes in the inner radii as we see in some of the plots, specially those with high redshift systems.

Preliminary tests have suggested that this may happen due to three different factors: first, the lower number of background source galaxies in the inner radii, leading to worse statistics, even though they are expected to have greater signal [Schneider, 2006], chance alignments of some systems, from which effects may not cancel out sufficiently for the number of clusters used in the poorer stacks, and large miscentered fractions of the systems belonging to a stack.

The cross ellipticity components have been also measured to search for systematic errors and yielded satisfactory results, being compatible with zero in most cases. In case which it deviated from zero, always less than two sigma, it did not display any particular bias, what could be indicative of relevant systematic errors in the method [Schneider, 2006, Bartelmann and Schneider, 2001].

5.2 *Parameter Estimation*

We have performed the aforementioned MCMC exploration of the posterior distribution of the parameter space for the total of 36 (3 redshift, 2 richness bins, divided in three magnitude gap groups by ΔM_{1-2} or by ΔM_{1-4}) stacks in 3 different models (a total of 108 fits), as described in chapter 4, with 5, 4 and 3 parameters. This results in a large collection of data with a total of 432 multidimensional posteriors, each of them represented by a Markov chain with 204800 links, as a result of using the 256 walkers in 1000 steps and discarding the first 20% as burn-in².

We have calculated medians and the 16th and 84th percentiles level to represent best fit candidates and regions of 68% confidence, respectively, which represent more robust statistics than maximum likelihood estimators. These numbers and the averages for the redMaPPer catalogue-derived parameters (mean redshift, mean richness, mean luminosity for each stack) are displayed in full on the tables in the end of this section (Tables 5.1 & 5.2).

As there were no qualitative differences between the stacks as divided by ΔM_{1-2} or ΔM_{1-4} a priori, we will focus on ΔM_{1-2} in the next section to discuss the significance of our results. We also concentrate on the first two redshift bins, which results in

² as explained in chapter 4, we discard an initial fraction of the Markov chain as "burn-in" to delete any effects of the choice of initial position of the walkers

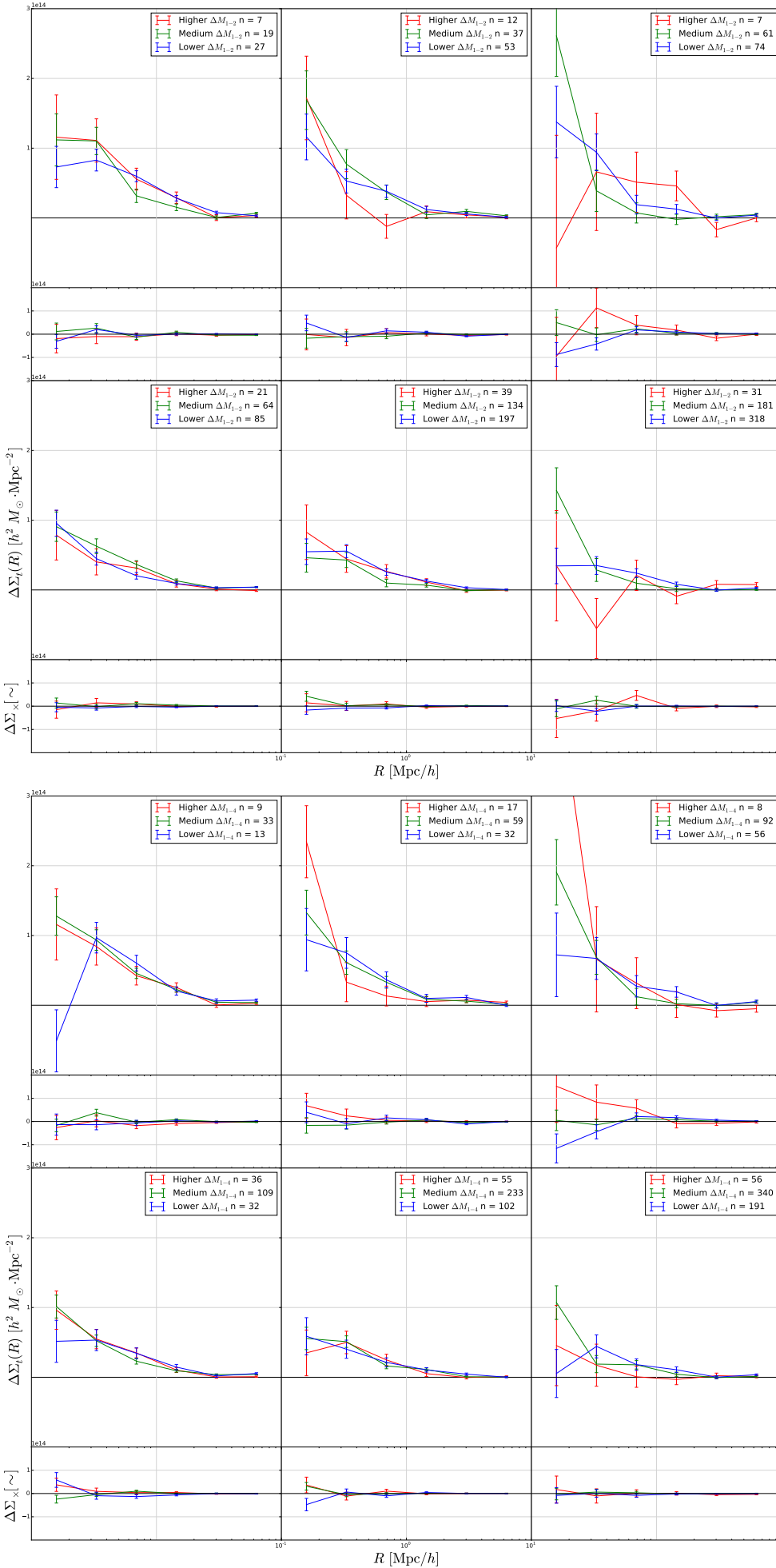


Figure 5.1: Results for the tangential shear in logarithmically spaced radial bins for the $\Delta M_{1-2(4)}$ defined stacks. From left to right, increasing redshift bins and from up to down, decreasing redMaPPer richness λ bins. The small lower panel in each of the 6 groups is the results for the cross shear. The 6 upper panels are ΔM_{1-2} , and the 6 lower ΔM_{1-4}

³ In fact, they become outliers when put together in the comparisons

discarding most of the systems, but as their background source counts are low, they result in less defined posteriors.³

Observing the distribution for masses and concentrations, more constrained models result in slightly better defined parameters, with narrower 68%CL regions. This is to be expected, as the information content of the data is divided between adjusted parameters.

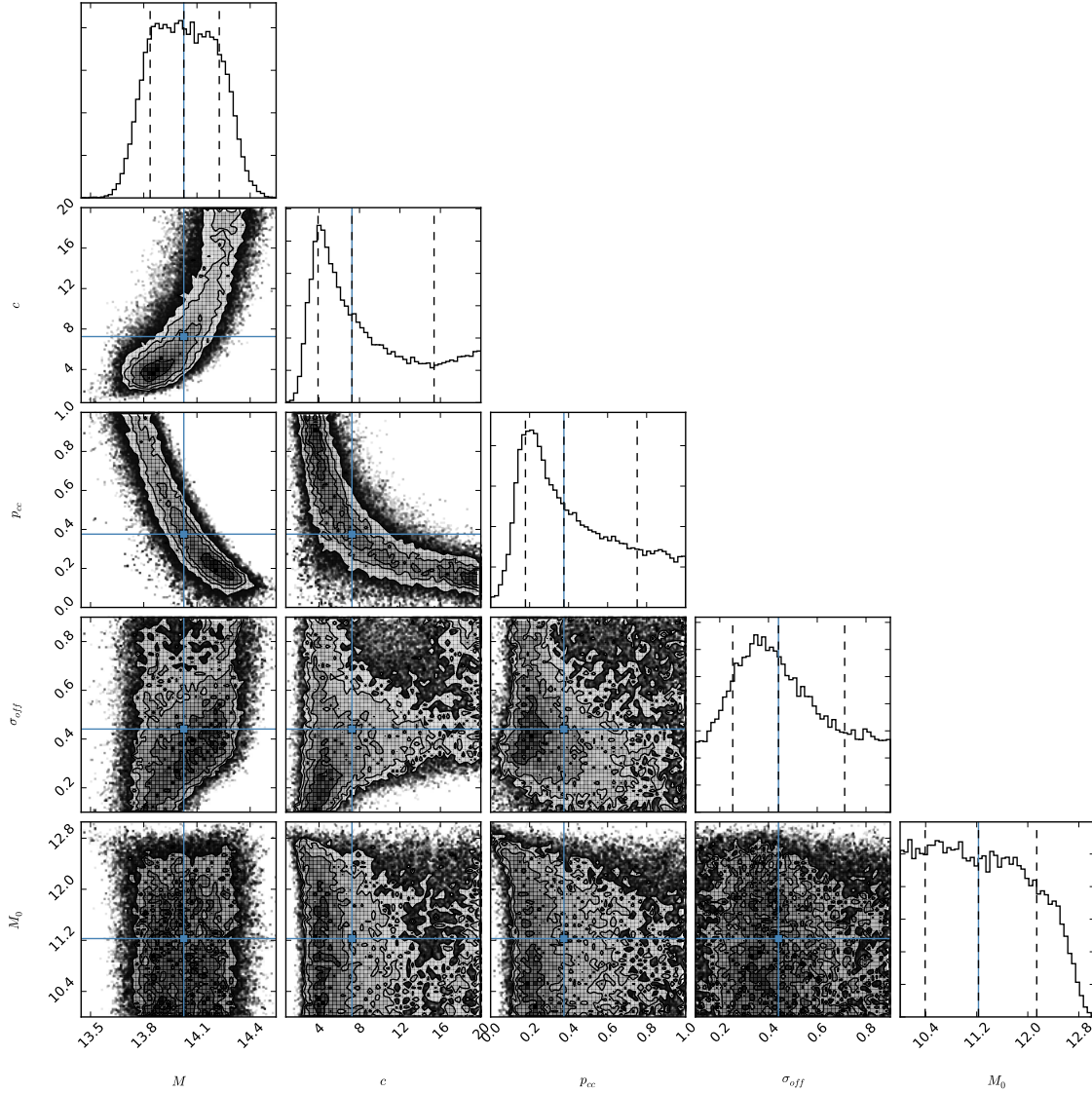
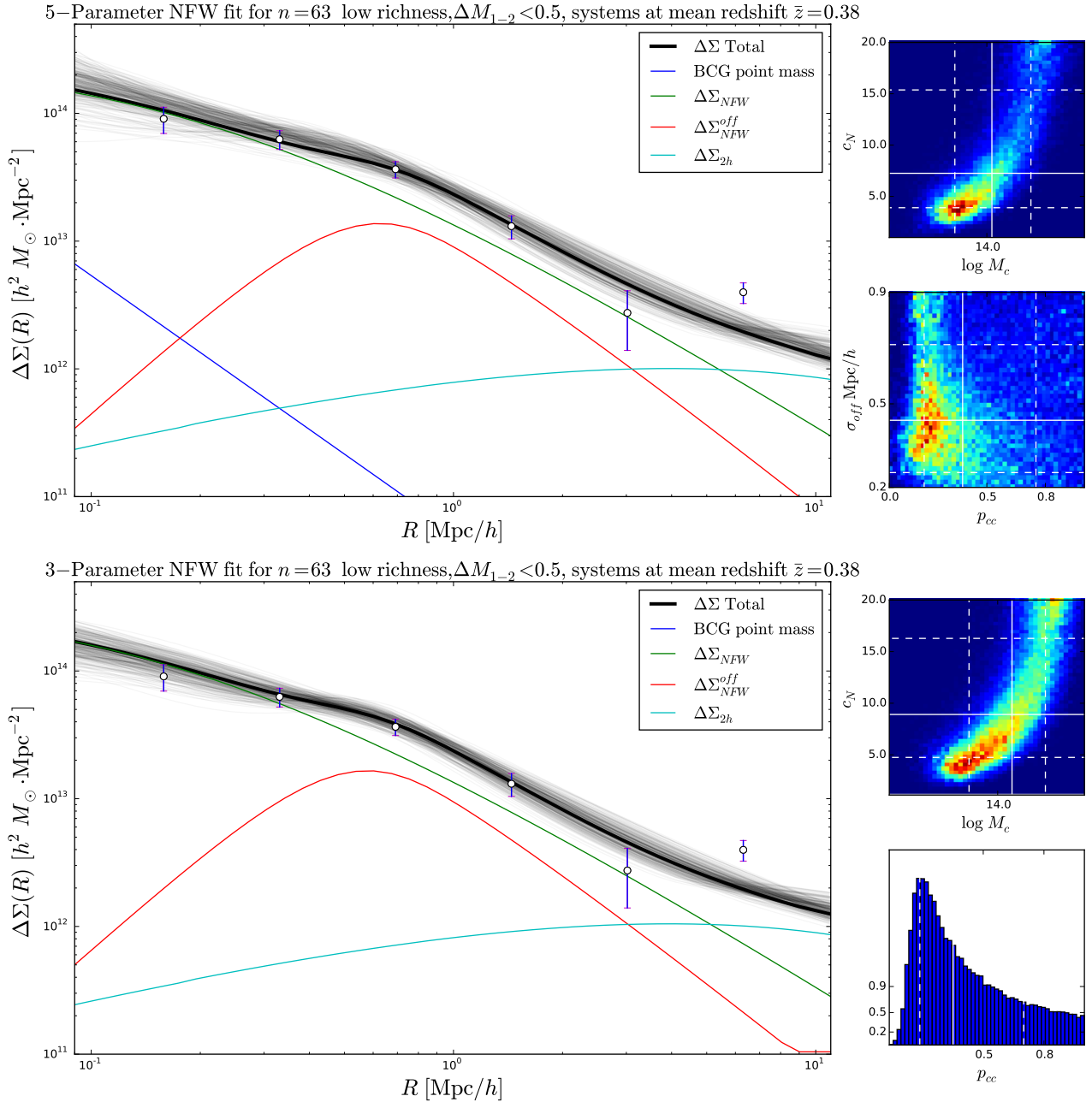


Figure 5.2: Example of a triangle plot for the 5 parameter model for the low redshift, low richness, middle magnitude gap stack. The whole result gallery with triangle plots and fit results as below for each of the fits will be made available online, together with the code as mentioned before.

To illustrate the results of the results of the fitting procedure, we display as an example of a so called *triangle plot*, that combines all 2D histograms of pairs of parameters for a single fit to represent the full multidimensional posterior distribution. We have chosen to display for that the low-richness, low-redshift, ΔM_{1-2} defined,

high magnitude gap bin in figure (Fig. 5.2). Some characteristics of the model that these plots suggest in general are that taking lower fractions of correctly centred clusters, the median inferred mass is higher, what illustrates an example of the degeneracies present in the model, and that choosing higher masses will result in higher concentrations.



We also present two examples of fits can be seen in the upper and lower figure 5.3 to understand the contribution of each factor in the full model (Eq. 4.32).

Figure 5.3: Example fit of the 5-parameter model into the low redshift, low richness, small ΔM_{1-2} stack. The colour curves are partial contributions to the overall profile, the black solid line the fitted curve and the gray curves a random sample of parameters drawn from their posterior probabilities distributions

	ΔM_{1-2}	< -1.5	[-1.5, -0.75]	[-0.75, 0]	ΔM_{1-2}	< -1.5	[-1.5, -0.75]	[-0.75, 0]	ΔM_{1-2}	< -1.5	[-1.5, -0.75]	[-0.75, 0]
$\lambda > 30$	M_{200}	$16.6^{+10.5}_{-6.5}$	$10.7^{+5.0}_{-3.3}$	$24.2^{+11.4}_{-6.6}$	M_{200}	$0.5^{+2.2}_{-0.5}$	$7.2^{+4.4}_{-2.6}$	$8.1^{+6.0}_{-3.2}$	M_{200}	$0.6^{+5.4}_{-0.5}$	$0.4^{+2.0}_{-0.4}$	$5.0^{+3.9}_{-2.5}$
	c_{200}	$8.9^{+6.5}_{-4.0}$	$9.0^{+6.4}_{-3.8}$	$5.7^{+5.5}_{-2.3}$	c_{200}	$10.4^{+6.5}_{-6.6}$	$10.6^{+6.1}_{-5.3}$	$8.7^{+6.6}_{-4.4}$	c_{200}	$9.2^{+7.0}_{-6.1}$	$11.2^{+6.2}_{-7.0}$	$11.5^{+5.9}_{-5.9}$
	c_{200}^{cor}	$8.9^{+6.5}_{-4.0}$	$8.6^{+6.1}_{-3.6}$	$5.9^{+5.7}_{-2.4}$	c_{200}^{cor}	$10.4^{+6.5}_{-6.6}$	$13.5^{+7.7}_{-6.8}$	$11.2^{+8.6}_{-5.7}$	c_{200}^{cor}	$9.2^{+7.0}_{-6.1}$	$10.9^{+6.0}_{-6.8}$	$14.0^{+7.2}_{-7.2}$
	P_{cc}	$0.39^{+0.35}_{-0.23}$	$0.51^{+0.32}_{-0.27}$	$0.23^{+0.22}_{-0.13}$	P_{cc}	$0.54^{+0.32}_{-0.27}$	$0.59^{+0.27}_{-0.28}$	$0.43^{+0.35}_{-0.23}$	P_{cc}	$0.45^{+0.38}_{-0.32}$	$0.51^{+0.34}_{-0.35}$	$0.55^{+0.30}_{-0.30}$
	σ_{off}	$0.42^{+0.30}_{-0.21}$	$0.36^{+0.38}_{-0.20}$	$0.35^{+0.19}_{-0.15}$	σ_{off}	$0.51^{+0.27}_{-0.28}$	$0.51^{+0.26}_{-0.27}$	$0.51^{+0.26}_{-0.22}$	σ_{off}	$0.50^{+0.27}_{-0.27}$	$0.50^{+0.27}_{-0.28}$	$0.47^{+0.30}_{-0.28}$
	M_0	$2.9^{+26.3}_{-2.6}$	$2.3^{+17.7}_{-2.0}$	$1.8^{+11.5}_{-1.5}$	M_0	$61.7^{+66.9}_{-60.2}$	$5.9^{+55.5}_{-5.5}$	$2.9^{+26.6}_{-2.6}$	M_0	$3.5^{+39.9}_{-3.2}$	$149.8^{+50.8}_{-77.8}$	$7.1^{+65.4}_{-6.7}$
	\bar{z}	0.38	0.25	0.35	\bar{z}	0.53	0.54	0.59	\bar{z}	0.72	0.74	0.73
	$\bar{\lambda}$	36.29	46.80	48.54	$\bar{\lambda}$	41.85	41.65	42.53	$\bar{\lambda}$	42.92	41.64	44.18
	\bar{L}	26.73	34.24	32.24	\bar{L}	29.70	31.06	30.41	\bar{L}	34.38	30.74	31.72
	ΔM_{1-2}	< -1.5	[-1.5, -0.75]	[-0.75, 0]	ΔM_{1-2}	< -1.5	[-1.5, -0.75]	[-0.75, 0]	ΔM_{1-2}	< -1.5	[-1.5, -0.75]	[-0.75, 0]
$\lambda < 30$	M_{200}	$3.7^{+3.8}_{-2.0}$	$10.6^{+6.2}_{-3.8}$	$5.7^{+4.6}_{-2.2}$	M_{200}	$3.1^{+3.1}_{-1.9}$	$1.6^{+1.4}_{-0.8}$	$6.2^{+3.2}_{-2.1}$	M_{200}	$0.3^{+2.0}_{-0.3}$	$0.2^{+1.2}_{-0.2}$	$5.6^{+4.1}_{-2.9}$
	c_{200}	$9.8^{+6.3}_{-5.1}$	$7.3^{+6.4}_{-3.4}$	$5.1^{+6.4}_{-3.2}$	c_{200}	$10.2^{+6.1}_{-5.5}$	$10.9^{+6.1}_{-5.8}$	$5.2^{+4.9}_{-2.0}$	c_{200}	$8.6^{+7.5}_{-6.6}$	$10.9^{+6.1}_{-6.7}$	$9.2^{+7.7}_{-5.9}$
	c_{200}^{cor}	$9.8^{+6.3}_{-5.1}$	$8.0^{+8.9}_{-3.7}$	$5.3^{+6.2}_{-3.3}$	c_{200}^{cor}	$10.2^{+6.1}_{-5.5}$	$10.9^{+5.7}_{-5.4}$	$5.5^{+5.2}_{-2.1}$	c_{200}^{cor}	$8.6^{+7.5}_{-6.6}$	$10.7^{+6.0}_{-6.6}$	$12.0^{+10.1}_{-7.7}$
	P_{cc}	$0.47^{+0.34}_{-0.29}$	$0.38^{+0.38}_{-0.20}$	$0.56^{+0.31}_{-0.30}$	P_{cc}	$0.51^{+0.33}_{-0.31}$	$0.52^{+0.32}_{-0.32}$	$0.35^{+0.35}_{-0.20}$	P_{cc}	$0.43^{+0.37}_{-0.31}$	$0.53^{+0.32}_{-0.35}$	$0.19^{+0.34}_{-0.13}$
	σ_{off}	$0.45^{+0.29}_{-0.23}$	$0.44^{+0.27}_{-0.19}$	$0.65^{+0.18}_{-0.28}$	σ_{off}	$0.48^{+0.28}_{-0.26}$	$0.42^{+0.32}_{-0.24}$	$0.29^{+0.32}_{-0.13}$	σ_{off}	$0.53^{+0.25}_{-0.28}$	$0.52^{+0.26}_{-0.27}$	$0.45^{+0.29}_{-0.20}$
	M_0	$4.3^{+34.2}_{-4.0}$	$1.7^{+12.1}_{-1.4}$	$6.4^{+39.6}_{-6.0}$	M_0	$5.9^{+43.6}_{-5.5}$	$3.3^{+22.7}_{-3.0}$	$1.5^{+9.2}_{-1.2}$	M_0	$2.5^{+18.0}_{-2.2}$	$85.6^{+30.1}_{-53.1}$	$1.5^{+9.8}_{-1.3}$
	\bar{z}	0.40	0.38	0.37	\bar{z}	0.50	0.59	0.59	\bar{z}	0.70	0.71	0.72
	$\bar{\lambda}$	19.98	21.24	20.47	$\bar{\lambda}$	20.80	19.96	19.79	$\bar{\lambda}$	20.24	20.21	20.28
	\bar{L}	14.60	15.51	14.80	\bar{L}	16.19	14.40	14.77	\bar{L}	16.43	15.10	14.52
	ΔM_{1-2}	< -1.5	[-1.5, -0.75]	[-0.75, 0]	ΔM_{1-2}	< -1.5	[-1.5, -0.75]	[-0.75, 0]	ΔM_{1-2}	< -1.5	[-1.5, -0.75]	[-0.75, 0]
$\lambda > 30$	M_{200}	$17.8^{+10.5}_{-7.1}$	$10.1^{+4.7}_{-2.9}$	$28.4^{+7.5}_{-7.9}$	M_{200}	$0.5^{+2.2}_{-0.5}$	$7.4^{+4.5}_{-2.6}$	$8.6^{+5.4}_{-3.5}$	M_{200}	$0.8^{+6.9}_{-0.7}$	$0.3^{+2.1}_{-0.3}$	$4.9^{+3.6}_{-2.2}$
	c_{200}	$9.6^{+6.2}_{-4.3}$	$8.8^{+6.5}_{-3.7}$	$7.6^{+4.6}_{-2.8}$	c_{200}	$10.9^{+6.2}_{-7.0}$	$11.0^{+5.8}_{-5.3}$	$8.7^{+6.4}_{-4.2}$	c_{200}	$9.3^{+7.0}_{-6.1}$	$11.6^{+6.0}_{-7.3}$	$11.7^{+5.8}_{-6.0}$
	c_{200}^{cor}	$9.6^{+6.2}_{-4.3}$	$8.3^{+6.2}_{-3.5}$	$7.9^{+4.8}_{-2.9}$	c_{200}^{cor}	$10.9^{+6.2}_{-7.0}$	$13.9^{+7.4}_{-6.7}$	$11.2^{+8.2}_{-5.4}$	c_{200}^{cor}	$9.3^{+7.0}_{-6.1}$	$10.7^{+6.5}_{-6.7}$	$13.9^{+6.9}_{-7.1}$
	P_{cc}	$0.39^{+0.34}_{-0.21}$	$0.60^{+0.27}_{-0.27}$	$0.21^{+0.20}_{-0.10}$	P_{cc}	$0.55^{+0.31}_{-0.36}$	$0.60^{+0.27}_{-0.28}$	$0.40^{+0.34}_{-0.22}$	P_{cc}	$0.43^{+0.36}_{-0.31}$	$0.52^{+0.33}_{-0.34}$	$0.60^{+0.27}_{-0.30}$
	σ_{off}	$0.39^{+0.34}_{-0.21}$	$0.60^{+0.27}_{-0.27}$	$0.21^{+0.20}_{-0.10}$	σ_{off}	$0.55^{+0.31}_{-0.36}$	$0.60^{+0.27}_{-0.28}$	$0.40^{+0.34}_{-0.22}$	σ_{off}	$0.43^{+0.36}_{-0.31}$	$0.52^{+0.33}_{-0.34}$	$0.60^{+0.27}_{-0.30}$
	M_0	$2.6^{+24.2}_{-2.3}$	$2.1^{+16.6}_{-1.9}$	$1.8^{+11.3}_{-1.5}$	M_0	$63.0^{+64.3}_{-60.8}$	$4.9^{+49.6}_{-4.6}$	$3.7^{+30.6}_{-3.4}$	M_0	$3.5^{+38.0}_{-3.2}$	$153.3^{+50.6}_{-78.4}$	$6.7^{+62.4}_{-6.3}$
	\bar{z}	0.38	0.25	0.35	\bar{z}	0.53	0.54	0.59	\bar{z}	0.72	0.74	0.73
	$\bar{\lambda}$	36.29	46.80	48.54	$\bar{\lambda}$	41.85	41.65	42.53	$\bar{\lambda}$	42.92	41.64	44.18
	\bar{L}	26.73	34.24	32.24	\bar{L}	29.70	31.06	30.41	\bar{L}	34.38	30.74	31.72
	ΔM_{1-2}	< -1.5	[-1.5, -0.75]	[-0.75, 0]	ΔM_{1-2}	< -1.5	[-1.5, -0.75]	[-0.75, 0]	ΔM_{1-2}	< -1.5	[-1.5, -0.75]	[-0.75, 0]
$\lambda < 30$	M_{200}	$4.1^{+4.1}_{-2.2}$	$12.1^{+5.0}_{-4.6}$	$4.9^{+3.0}_{-1.7}$	M_{200}	$3.4^{+3.4}_{-1.9}$	$1.5^{+1.3}_{-0.8}$	$6.7^{+3.6}_{-2.5}$	M_{200}	$0.3^{+2.0}_{-0.3}$	$0.2^{+1.0}_{-0.2}$	$6.6^{+4.0}_{-3.5}$
	c_{200}	$10.3^{+6.0}_{-5.2}$	$9.0^{+7.6}_{-4.4}$	$4.6^{+7.3}_{-3.0}$	c_{200}	$10.6^{+6.1}_{-5.5}$	$11.5^{+5.7}_{-6.2}$	$6.2^{+5.5}_{-2.7}$	c_{200}	$9.2^{+7.4}_{-6.8}$	$11.3^{+6.1}_{-7.1}$	$10.7^{+6.6}_{-6.5}$
	c_{200}^{cor}	$10.3^{+6.0}_{-5.2}$	$10.0^{+8.4}_{-4.9}$	$4.6^{+7.4}_{-3.1}$	c_{200}^{cor}	$10.6^{+6.1}_{-5.5}$	$10.7^{+5.3}_{-5.7}$	$6.7^{+5.9}_{-2.9}$	c_{200}^{cor}	$9.2^{+7.4}_{-6.8}$	$10.8^{+5.8}_{-6.8}$	$14.1^{+8.7}_{-8.6}$
	P_{cc}	$0.44^{+0.35}_{-0.27}$	$0.32^{+0.35}_{-0.15}$	$0.62^{+0.27}_{-0.32}$	P_{cc}	$0.49^{+0.32}_{-0.30}$	$0.58^{+0.28}_{-0.31}$	$0.39^{+0.32}_{-0.20}$	P_{cc}	$0.41^{+0.39}_{-0.29}$	$0.51^{+0.34}_{-0.35}$	$0.16^{+0.31}_{-0.11}$
	σ_{off}	$0.44^{+0.35}_{-0.27}$	$0.32^{+0.35}_{-0.15}$	$0.62^{+0.27}_{-0.32}$	σ_{off}	$0.49^{+0.32}_{-0.30}$	$0.58^{+0.28}_{-0.31}$	$0.39^{+0.32}_{-0.20}$	σ_{off}	$0.41^{+0.39}_{-0.29}$	$0.51^{+0.34}_{-0.35}$	$0.16^{+0.31}_{-0.11}$
	M_0	$4.4^{+34.3}_{-4.0}$	$1.8^{+12.5}_{-1.6}$	$7.6^{+42.0}_{-7.1}$	M_0	$5.5^{+43.0}_{-5.1}$	$3.3^{+25.1}_{-3.0}$	$1.2^{+7.6}_{-1.0}$	M_0	$2.1^{+17.4}_{-1.8}$	$89.8^{+28.2}_{-44.0}$	$1.7^{+10.2}_{-1.5}$
	\bar{z}	0.40	0.38	0.37	\bar{z}	0.50	0.59	0.59	\bar{z}	0.70	0.71	0.72
	$\bar{\lambda}$	19.98	21.24	20.47	$\bar{\lambda}$	20.80	19.96	19.79	$\bar{\lambda}$	20.24	20.21	20.28
	\bar{L}	14.60	15.51	14.80	\bar{L}	16.19	14.40	14.77	\bar{L}	16.43	15.10	14.52
	ΔM_{1-2}	< -1.5	[-1.5, -0.75]	[-0.75, 0]	ΔM_{1-2}	< -1.5	[-1.5, -0.75]	[-0.75, 0]	ΔM_{1-2}	< -1.5	[-1.5, -0.75]	[-0.75, 0]
$\lambda > 30$	M_{200}	$17.5^{+10.4}_{-6.8}$	$10.1^{+4.7}_{-2.8}$	$27.8^{+7.7}_{-7.5}$	M_{200}	$2.0^{+2.3}_{-1.6}$	$7.6^{+4.0}_{-2.3}$	$8.3^{+5.0}_{-3.2}$	M_{200}	$0.9^{+7.2}_{-0.9}$	$3.7^{+1.9}_{-1.4}$	$5.5^{+3.6}_{-2.0}$
	c_{200}	$9.9^{+6.0}_{-4.4}$	$9.2^{+6.5}_{-3.7}$	$7.5^{+4.5}_{-2.8}$	c_{200}	$12.6^{+5.2}_{-6.7}$	$12.1^{+5.2}_{-5.0}$	$9.2^{+6.0}_{-4.1}$	c_{200}	$9.6^{+6.9}_{-6.3}$	$15.5^{+3.2}_{-5.0}$	$13.0^{+4.9}_{-5.8}$
	c_{200}^{cor}	$9.9^{+6.0}_{-4.4}$	$8.8^{+6.2}_{-3.5}$	$7.9^{+4.7}_{-2.9}$	c_{200}^{cor}	$12.6^{+5.2}_{-6.7}$	$13.7^{+5.9}_{-5.7}$	$10.5^{+6.8}_{-4.7}$	c_{200}^{cor}	$9.6^{+6.9}_{-6.3}$	$17.5^{+3.7}_{-5.7}$	$15.3^{+5.8}_{-6.8}$
	P_{cc}	$0.42^{+0.34}_{-0.22}$	$0.62^{+0.26}_{-0.26}$	$0.24^{+0.20}_{-0.11}$	P_{cc}	$0.65^{+0.25}_{-0.33}$	$0.64^{+0.24}_{-0.25}$	$0.46^{+0.32}_{-0.22}$	P_{cc}	$0.43^{+0.37}_{-0.31}$	$0.76^{+0.17}_{-0.25}$	$0.64^{+0.24}_{-0.26}$
	σ_{off}	$0.42^{+0.34}_{-0.22}$	$0.62^{+0.26}_{-0.26}$	$0.24^{+0.20}_{-0.11}$	σ_{off}	$0.65^{+0.25}_{-0.33}$	$0.64^{+0.24}_{-0.25}$	$0.46^{+0.32}_{-0.22}$	σ_{off}	$0.43^{+0.37}_{-0.31}$	$0.76^{+0.17}_{-0.25}$	$0.64^{+0.24}_{-0.26}$
	M_0	$4.3^{+4.0}_{-2.0}$	$11.6^{+5.0}_{-4.3}$	$5.6^{+2.9}_{-1.5}$	M_0	$3.8^{+3.3}_{-1.7}$	$1.7^{+1.2}_{-0.6}$	$6.5^{+3.5}_{-2.4}$	M_0	$0.3^{+2.1}_{-0.3}$	$1.9^{+0.9}_{-0.6}$	$6.5^{+4.0}_{-3.4}$
	\bar{z}	0.38	0.25	0.35	\bar{z}	0.53	0.54	0.59	\bar{z}	0.72	0.74	0.73
	$\bar{\lambda}$	36.29	46.80	48.54	$\bar{\lambda}$	41.85	41.65	42.53	$\bar{\lambda}$	42.92	41.64	44.18
	\bar{L}	26.73	34.24	32.24	\bar{L}	29.70	31.06	30.41	\bar{L}	34.38	30.74	31.72
	ΔM_{1-2}	< -1.5	[-1.5, -0.75]	[-0.75, 0]	ΔM_{1-2}	< -1.5	[-1.5, -0.75]	[-0.75, 0]	ΔM_{1-2}	< -1.5	[-1.5, -0.75]	[-0.75, 0]
$\lambda < 30$	M_{200}	$4.3^{+4.0}_{-2.0}$	$11.6^{+5.0}_{-4.3}$	$5.6^{+2.9}_{-1.5}$	M_{200}	$3.8^{+3.3}_{-1.7}$	$1.7^{+1.2}_{-0.6}$	$6.5^{+3.5}_{-2.4}$	M_{200}	$0.3^{+2.1}_{-0.3}$	$1.9^{+0.9}_{-0.6}$	$6.5^{+4.0}_{-3.4}$
	c_{200}	$11.0^{+5.7}_{-5.1}$	$8.9^{+7.4}_{-4.2}$	$6.6^{+7.9}_{-2.9}$	c_{200}	$11.5^{+5.6}_{-5.3}$	$12.2^{+5.3}_{-5.8}$	$6.2^{+5.4}_{-2.6}$	c_{200}	$9.2^{+7.4}_{-7.0}$	$15.3^{+3.3}_{-5.1}$	$10.8^{+6.5}_{-6.5}$
	c_{200}^{cor}	$11.0^{+5.7}_{-5.1}$	$9.8^{+8.1}_{-4.6}$	$6.8^{+8.1}_{-3.0}$	c_{200}^{cor}	$11.5^{+5.6}_{-5.3}$	$11.4^{+4.9}_{-5.4}$	$6.6^{+5.7}_{-2.7}$	c_{200}^{cor}	$9.2^{+7.4}_{-7.0}$	$18.0^{+3.9}_{-6.0}$	$14.2^{+8.6}_{-8.5}$
	P_{cc}	$0.51^{+0.31}_{-0.28}$										

	ΔM_{1-4}	< -2	[-2, -1]	[-1, 0]	ΔM_{1-4}	< -2	[-2, -1]	[-1, 0]	ΔM_{1-4}	< -2	[-2, -1]	[-1, 0]	
$\lambda > 30$	M_{200}	$10.9^{+10.9}_{-5.3}$	$17.7^{+11.1}_{-6.9}$	$7.1^{+8.1}_{-4.5}$	M_{200}	$3.7^{+3.2}_{-2.9}$	$8.1^{+5.3}_{-3.4}$	$2.7^{+7.3}_{-2.5}$	M_{200}	$2.6^{+7.9}_{-2.6}$	$7.7^{+7.4}_{-4.0}$	$10.9^{+12.7}_{-6.8}$	
	c_{200}	$7.6^{+6.9}_{-4.4}$	$7.6^{+6.1}_{-3.8}$	$8.2^{+7.4}_{-5.1}$	c_{200}	$11.9^{+5.8}_{-7.6}$	$7.6^{+7.5}_{-3.8}$	$5.5^{+8.9}_{-4.3}$	c_{200}	$10.2^{+6.6}_{-6.2}$	$7.7^{+8.1}_{-4.7}$	$7.8^{+7.3}_{-4.7}$	
	c_{200}^{cor}	$7.6^{+6.9}_{-4.4}$	$8.0^{+6.4}_{-4.0}$	$7.9^{+7.1}_{-4.9}$	c_{200}^{cor}	$11.9^{+5.8}_{-7.6}$	$8.1^{+8.0}_{-4.1}$	$5.4^{+8.7}_{-4.2}$	c_{200}^{cor}	$10.2^{+6.6}_{-6.2}$	$8.5^{+9.0}_{-5.2}$	$8.8^{+8.3}_{-5.3}$	
	p_{cc}	$0.38^{+0.38}_{-0.24}$	$0.38^{+0.33}_{-0.20}$	$0.44^{+0.37}_{-0.29}$	p_{cc}	$0.61^{+0.27}_{-0.33}$	$0.31^{+0.39}_{-0.20}$	$0.38^{+0.40}_{-0.28}$	p_{cc}	$0.53^{+0.32}_{-0.34}$	$0.27^{+0.42}_{-0.19}$	$0.44^{+0.36}_{-0.29}$	
	σ_{off}	$0.62^{+0.19}_{-0.27}$	$0.65^{+0.17}_{-0.24}$	$0.48^{+0.28}_{-0.25}$	σ_{off}	$0.50^{+0.28}_{-0.28}$	$0.34^{+0.32}_{-0.15}$	$0.57^{+0.23}_{-0.29}$	σ_{off}	$0.49^{+0.28}_{-0.28}$	$0.43^{+0.30}_{-0.20}$	$0.53^{+0.25}_{-0.27}$	
	M_0	$14.9^{+74.5}_{-14.4}$	$11.3^{+76.3}_{-10.8}$	$3.7^{+33.3}_{-3.4}$	M_0	$57.9^{+88.4}_{-56.4}$	$1.6^{+13.0}_{-1.4}$	$3.1^{+23.8}_{-2.8}$	M_0	$38.7^{+210.8}_{-38.0}$	$1.9^{+14.4}_{-1.7}$	$5.2^{+51.2}_{-4.9}$	
	\bar{z}	0.25	0.35	0.36	\bar{z}	0.53	0.54	0.59	\bar{z}	0.72	0.73	0.68	
	$\bar{\lambda}$	35.47	48.93	46.97	$\bar{\lambda}$	40.94	41.96	42.81	$\bar{\lambda}$	40.03	42.62	43.37	
	\bar{L}	25.76	34.19	30.69	\bar{L}	29.36	30.97	30.36	\bar{L}	30.78	31.56	30.79	
	ΔM_{1-4}	< -2	[-2, -1]	[-1, 0]	ΔM_{1-4}	< -2	[-2, -1]	[-1, 0]	ΔM_{1-4}	< -2	[-2, -1]	[-1, 0]	
$\lambda < 30$	M_{200}	$15.2^{+7.5}_{-5.8}$	$6.2^{+3.9}_{-2.1}$	$12.9^{+9.2}_{-6.2}$	M_{200}	$1.9^{+2.1}_{-1.2}$	$1.4^{+1.1}_{-0.8}$	$3.3^{+3.3}_{-2.6}$	M_{200}	$0.6^{+2.2}_{-0.5}$	$0.8^{+1.1}_{-0.7}$	$13.1^{+12.8}_{-7.7}$	
	c_{200}	$7.5^{+7.1}_{-3.8}$	$6.7^{+5.6}_{-2.8}$	$6.5^{+7.9}_{-3.6}$	c_{200}	$9.6^{+6.8}_{-6.1}$	$10.0^{+5.9}_{-5.3}$	$9.6^{+6.8}_{-5.9}$	c_{200}	$9.8^{+6.7}_{-6.3}$	$10.4^{+6.5}_{-6.2}$	$5.0^{+7.5}_{-3.1}$	
	c_{200}^{cor}	$7.5^{+7.1}_{-3.8}$	$6.2^{+5.2}_{-2.6}$	$6.4^{+7.8}_{-3.6}$	c_{200}^{cor}	$9.6^{+6.8}_{-6.1}$	$9.8^{+5.8}_{-5.2}$	$10.1^{+7.1}_{-6.2}$	c_{200}^{cor}	$9.8^{+6.7}_{-6.3}$	$10.7^{+6.6}_{-6.4}$	$6.6^{+10.0}_{-4.0}$	
	p_{cc}	$0.16^{+0.22}_{-0.09}$	$0.49^{+0.31}_{-0.23}$	$0.17^{+0.35}_{-0.12}$	p_{cc}	$0.53^{+0.32}_{-0.31}$	$0.59^{+0.28}_{-0.32}$	$0.59^{+0.28}_{-0.34}$	p_{cc}	$0.50^{+0.34}_{-0.34}$	$0.54^{+0.32}_{-0.33}$	$0.14^{+0.36}_{-0.11}$	
	σ_{off}	$0.40^{+0.18}_{-0.14}$	$0.52^{+0.24}_{-0.24}$	$0.40^{+0.23}_{-0.16}$	σ_{off}	$0.51^{+0.27}_{-0.28}$	$0.44^{+0.32}_{-0.25}$	$0.54^{+0.25}_{-0.30}$	σ_{off}	$0.51^{+0.27}_{-0.27}$	$0.50^{+0.27}_{-0.28}$	$0.45^{+0.24}_{-0.19}$	
	M_0	$2.4^{+17.6}_{-2.1}$	$2.7^{+18.0}_{-2.4}$	$1.6^{+10.9}_{-1.4}$	M_0	$6.4^{+39.7}_{-6.0}$	$5.8^{+31.0}_{-5.4}$	$26.5^{+90.8}_{-25.8}$	M_0	$4.3^{+37.3}_{-3.9}$	$10.8^{+35.0}_{-10.3}$	$1.4^{+9.2}_{-1.1}$	
	\bar{z}	0.40	0.38	0.37	\bar{z}	0.55	0.59	0.59	\bar{z}	0.73	0.71	0.66	
	$\bar{\lambda}$	19.99	20.94	20.66	$\bar{\lambda}$	20.24	20.03	19.92	$\bar{\lambda}$	20.04	20.31	20.55	
	\bar{L}	15.46	15.06	14.50	\bar{L}	15.52	14.79	14.20	\bar{L}	16.27	15.07	14.03	
	ΔM_{1-4}	< -2	[-2, -1]	[-1, 0]	ΔM_{1-4}	< -2	[-2, -1]	[-1, 0]	ΔM_{1-4}	< -2	[-2, -1]	[-1, 0]	
$\lambda > 30$	M_{200}	$13.3^{+8.2}_{-5.4}$	$14.5^{+6.2}_{-4.1}$	$31.2^{+10.9}_{-14.9}$	M_{200}	$1.7^{+3.4}_{-1.6}$	$6.5^{+3.9}_{-2.3}$	$8.3^{+5.8}_{-3.3}$	M_{200}	$0.3^{+2.9}_{-0.3}$	$1.5^{+2.7}_{-1.4}$	$6.9^{+6.5}_{-3.7}$	
	c_{200}	$9.2^{+6.3}_{-4.2}$	$6.9^{+5.0}_{-2.4}$	$9.1^{+7.2}_{-6.1}$	c_{200}	$10.9^{+6.4}_{-7.9}$	$10.3^{+6.0}_{-4.7}$	$7.2^{+6.9}_{-3.7}$	c_{200}	$10.5^{+6.5}_{-6.6}$	$12.6^{+5.3}_{-7.2}$	$7.6^{+7.8}_{-4.8}$	
	c_{200}^{cor}	$9.2^{+6.3}_{-4.2}$	$6.9^{+5.1}_{-2.4}$	$9.8^{+7.8}_{-6.6}$	c_{200}^{cor}	$10.9^{+6.4}_{-7.9}$	$11.6^{+6.8}_{-5.3}$	$8.4^{+6.8}_{-4.3}$	c_{200}^{cor}	$10.5^{+6.5}_{-6.6}$	$14.7^{+6.2}_{-8.4}$	$10.2^{+10.5}_{-6.4}$	
	p_{cc}	$0.42^{+0.34}_{-0.23}$	$0.51^{+0.30}_{-0.23}$	$0.11^{+0.45}_{-0.08}$	p_{cc}	$0.56^{+0.31}_{-0.36}$	$0.54^{+0.30}_{-0.25}$	$0.49^{+0.33}_{-0.27}$	p_{cc}	$0.50^{+0.34}_{-0.34}$	$0.56^{+0.30}_{-0.36}$	$0.42^{+0.36}_{-0.27}$	
	M_0	$3.2^{+29.0}_{-2.9}$	$2.0^{+15.8}_{-1.8}$	$1.1^{+5.9}_{-0.9}$	M_0	$121.5^{+58.7}_{-107.9}$	$3.8^{+36.1}_{-3.5}$	$2.8^{+23.4}_{-2.5}$	M_0	$259.2^{+123.8}_{-172.2}$	$103.2^{+57.8}_{-97.4}$	$2.8^{+26.0}_{-2.5}$	
	\bar{z}	0.35	0.35	0.59	\bar{z}	0.53	0.54	0.59	\bar{z}	0.72	0.73	0.68	
	$\bar{\lambda}$	35.47	48.93	46.97	$\bar{\lambda}$	40.94	41.96	42.81	$\bar{\lambda}$	40.03	42.62	43.37	
	\bar{L}	25.76	34.19	30.69	\bar{L}	29.36	30.97	30.36	\bar{L}	30.78	31.56	30.79	
	ΔM_{1-4}	< -2	[-2, -1]	[-1, 0]	ΔM_{1-4}	< -2	[-2, -1]	[-1, 0]	ΔM_{1-4}	< -2	[-2, -1]	[-1, 0]	
	$\lambda < 30$	M_{200}	$7.2^{+4.3}_{-2.9}$	$5.3^{+2.8}_{-1.4}$	$11.6^{+6.8}_{-4.9}$	M_{200}	$3.3^{+3.6}_{-1.8}$	$3.6^{+2.1}_{-1.2}$	$4.6^{+3.3}_{-3.0}$	M_{200}	$0.2^{+0.9}_{-0.2}$	$1.1^{+1.3}_{-1.0}$	$5.1^{+4.8}_{-2.8}$
c_{200}		$11.7^{+5.3}_{-4.8}$	$4.5^{+5.1}_{-2.5}$	$5.7^{+7.3}_{-3.1}$	c_{200}	$10.7^{+6.3}_{-5.8}$	$7.4^{+6.2}_{-3.1}$	$5.8^{+6.3}_{-3.0}$	c_{200}	$10.2^{+6.7}_{-6.8}$	$11.2^{+5.8}_{-6.5}$	$7.2^{+8.9}_{-5.0}$	
c_{200}^{cor}		$11.7^{+5.3}_{-4.8}$	$4.3^{+5.0}_{-2.4}$	$6.0^{+7.6}_{-3.3}$	c_{200}^{cor}	$10.7^{+6.3}_{-5.8}$	$7.5^{+6.2}_{-3.1}$	$6.0^{+6.4}_{-3.1}$	c_{200}^{cor}	$10.2^{+6.7}_{-6.8}$	$13.1^{+6.9}_{-7.6}$	$9.7^{+12.1}_{-6.7}$	
p_{cc}		$0.39^{+0.31}_{-0.20}$	$0.70^{+0.21}_{-0.33}$	$0.31^{+0.42}_{-0.20}$	p_{cc}	$0.38^{+0.38}_{-0.25}$	$0.53^{+0.31}_{-0.25}$	$0.43^{+0.34}_{-0.25}$	p_{cc}	$0.47^{+0.34}_{-0.33}$	$0.55^{+0.31}_{-0.35}$	$0.23^{+0.42}_{-0.17}$	
M_0		$2.6^{+24.2}_{-2.4}$	$6.0^{+39.3}_{-5.6}$	$1.8^{+11.5}_{-1.5}$	M_0	$2.5^{+17.5}_{-2.2}$	$1.4^{+7.9}_{-1.1}$	$2.1^{+16.0}_{-1.8}$	M_0	$3.3^{+24.7}_{-3.0}$	$46.3^{+35.0}_{-44.2}$	$1.5^{+9.0}_{-1.2}$	
\bar{z}		0.40	0.38	0.37	\bar{z}	0.55	0.59	0.59	\bar{z}	0.73	0.71	0.66	
$\bar{\lambda}$		19.99	20.94	20.66	$\bar{\lambda}$	20.24	20.03	19.92	$\bar{\lambda}$	20.04	20.31	20.55	
\bar{L}		15.46	15.06	14.50	\bar{L}	15.52	14.79	14.20	\bar{L}	16.27	15.07	14.03	
ΔM_{1-4}		< -2	[-2, -1]	[-1, 0]	ΔM_{1-4}	< -2	[-2, -1]	[-1, 0]	ΔM_{1-4}	< -2	[-2, -1]	[-1, 0]	
$\lambda > 30$		M_{200}	$13.0^{+8.0}_{-5.0}$	$14.6^{+6.0}_{-4.0}$	$32.0^{+10.7}_{-14.6}$	M_{200}	$4.8^{+2.7}_{-1.6}$	$6.5^{+3.7}_{-2.2}$	$8.3^{+5.5}_{-3.0}$	M_{200}	$3.9^{+5.4}_{-3.7}$	$3.9^{+2.0}_{-1.2}$	$7.4^{+6.6}_{-3.7}$
	c_{200}	$9.6^{+6.2}_{-4.2}$	$7.2^{+5.0}_{-2.5}$	$9.8^{+7.0}_{-6.5}$	c_{200}	$14.7^{+3.8}_{-5.4}$	$11.3^{+5.5}_{-4.6}$	$7.8^{+6.6}_{-3.8}$	c_{200}	$13.4^{+4.7}_{-6.8}$	$15.5^{+3.2}_{-6.8}$	$8.4^{+7.6}_{-5.1}$	
	c_{200}^{cor}	$9.6^{+6.2}_{-4.2}$	$7.3^{+5.1}_{-2.5}$	$10.6^{+7.6}_{-7.1}$	c_{200}^{cor}	$14.7^{+3.8}_{-5.4}$	$11.6^{+5.6}_{-4.7}$	$8.1^{+7.0}_{-4.0}$	c_{200}^{cor}	$13.4^{+4.7}_{-6.8}$	$15.5^{+3.2}_{-6.8}$	$8.9^{+8.1}_{-5.4}$	
	p_{cc}	$0.47^{+0.32}_{-0.24}$	$0.52^{+0.29}_{-0.23}$	$0.10^{+0.40}_{-0.07}$	p_{cc}	$0.74^{+0.18}_{-0.25}$	$0.58^{+0.27}_{-0.24}$	$0.53^{+0.31}_{-0.27}$	p_{cc}	$0.67^{+0.23}_{-0.34}$	$0.74^{+0.18}_{-0.25}$	$0.43^{+0.35}_{-0.26}$	
	\bar{z}	0.25	0.35	0.36	\bar{z}	0.53	0.54	0.59	\bar{z}	0.72	0.73	0.68	
	$\bar{\lambda}$	35.47	48.93	46.97	$\bar{\lambda}$	40.94	41.96	42.81	$\bar{\lambda}$	40.03	42.62	43.37	
	\bar{L}	25.76	34.19	30.69	\bar{L}	29.36	30.97	30.36	\bar{L}	30.78	31.56	30.79	
	ΔM_{1-4}	< -2	[-2, -1]	[-1, 0]	ΔM_{1-4}	< -2	[-2, -1]	[-1, 0]	ΔM_{1-4}	< -2	[-2, -1]	[-1, 0]	
	$\lambda < 30$	M_{200}	$6.9^{+4.2}_{-2.7}$	$5.9^{+2.9}_{-1.4}$	$11.7^{+6.7}_{-4.8}$	M_{200}	$3.5^{+3.5}_{-1.8}$	$3.5^{+2.1}_{-1.2}$	$4.6^{+3.3}_{-1.8}$	M_{200}	$0.2^{+1.0}_{-0.2}$	$1.9^{+1.2}_{-0.6}$	$5.2^{+4.9}_{-2.8}$
		c_{200}	$12.2^{+5.0}_{-4.8}$	$6.1^{+7.2}_{-2.2}$	$6.1^{+7.5}_{-3.3}$	c_{200}	$10.9^{+6.2}_{-5.7}$	$7.7^{+6.4}_{-3.2}$	$6.5^{+6.1}_{-3.2}$	c_{200}	$10.6^{+6.4}_{-6.8}$	$13.8^{+4.3}_{-5.2}$	$7.3^{+9.0}_{-4.9}$
c_{200}^{cor}		$12.2^{+5.0}_{-4.8}$	$6.0^{+7.1}_{-2.1}$	$6.4^{+7.9}_{-3.5}$	c_{200}^{cor}	$10.9^{+6.2}_{-5.7}$	$7.7^{+6.4}_{-3.2}$	$6.6^{+6.2}_{-3.3}$	c_{200}^{cor}	$10.6^{+6.4}_{-6.8}$	$16.9^{+5.2}_{-6.3}$	$9.7^{+12.0}_{-6.6}$	
p_{cc}		$0.44^{+0.32}_{-0.20}$	$0.66^{+0.24}_{-0.31}$	$0.32^{+0.40}_{-0.20}$	p_{cc}	$0.42^{+0.36}_{-0.25}$	$0.55^{+0.29}_{-0.25}$	$0.47^{+0.33}_{-0.25}$	p_{cc}	$0.49^{+0.35}_{-0.33}$	$0.71^{+0.20}_{-0.26}$	$0.25^{+0.42}_{-0.18}$	
\bar{z}		0.40	0.38	0.37	\bar{z}	0.55	0.59	0.59	\bar{z}	0.73	0.71	0.66	
$\bar{\lambda}$		19.99	20.94	20.66	$\bar{\lambda}$	20.24	20.03	19.92	$\bar{\lambda}$	20.04	20.31	20.55	
\bar{L}		15.46	15.06	14.50	\bar{L}	15.52	14.79	14.20	\bar{L}	16.27	15.07	14.03	
ΔM_{1-4}		< -2	[-2, -1]	[-1, 0]	ΔM_{1-4}	< -2	[-2, -1]	[-1, 0]	ΔM_{1-4}	< -2	[-2, -1]	[-1, 0]	

 $0.2 < z < 0.4$
 $0.4 < z < 0.6$
 $0.6 < z < 0.75$

Table 5.2: Marginalised median values for the parameters with 16th and 84th percentiles, together with averages in z , λ and L . M_{200} in $10^{13}M_{\odot}$, M_0 in $10^{11}M_{\odot}$, and L in $10^{10}L_{\odot}$, for the 3 models (up: Full, mid; $\sigma_{off} = 0.42h$, low; and $M_0 = 0$)

5.3 Model Comparison

The different models, with 5, 4, or 3 parameters, have been looked into by comparing the median values and percentiles calculated from the posterior distributions. By looking at the tables 5.1 & 5.2 one can see that there is no distinguishable difference between the three models. For an example, we look into the masses and concentrations of two examples of stacks under the three models, which are displayed in the table 5.3.

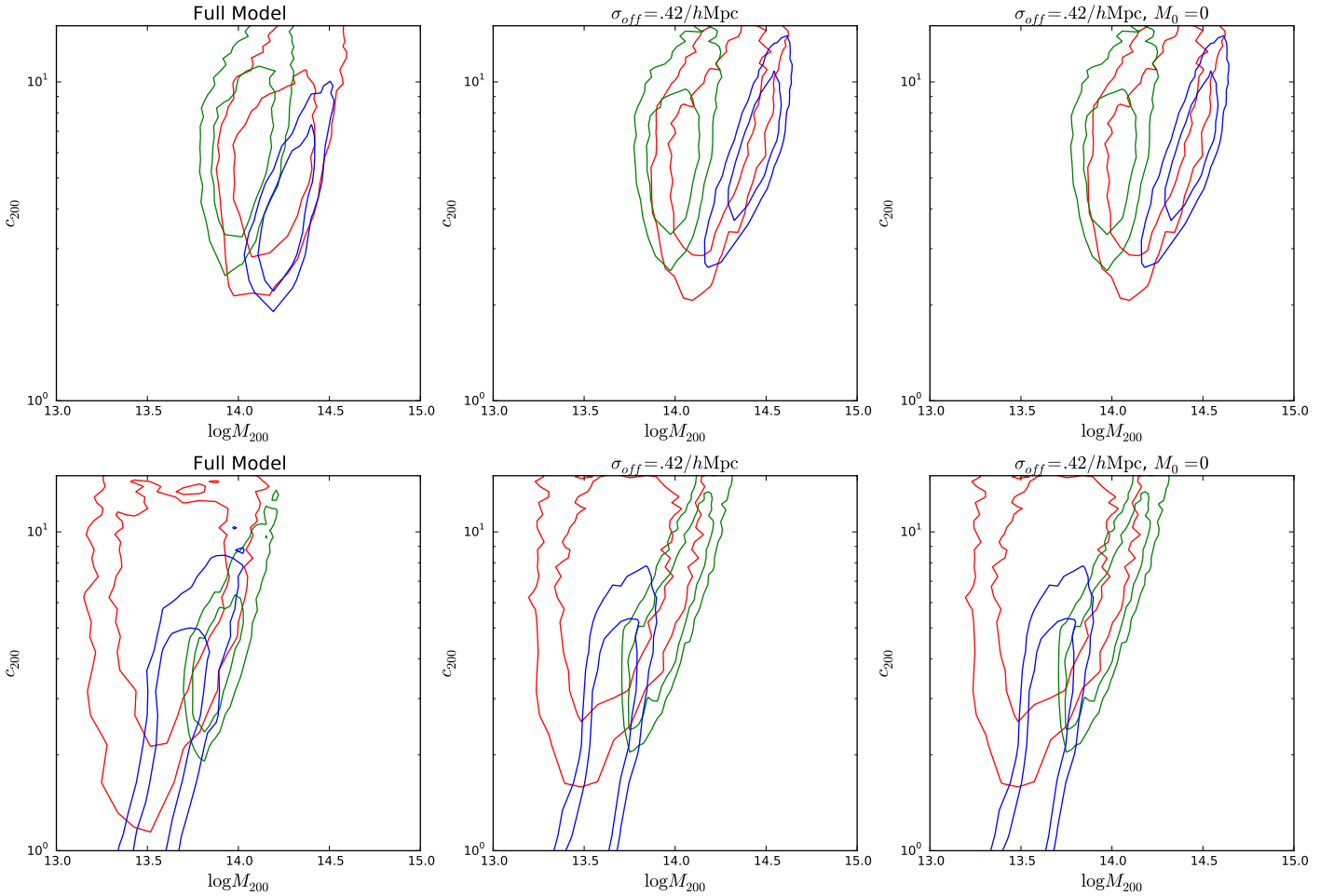


Figure 5.4: 2D histograms depicted by curves at half-maximum and 1/4 maximum for comparison between different models.

On the upper panel, it is shown the ΔM_{1-2} selected, large magnitude gap, high λ , low z stack. On the lower, everything the same, but with the low λ stack.

We also illustrate some differences in the models comparing 2D histograms for mass and concentrations in the ΔM_{1-2} defined stacks in figure (5.4). This figure displays only the first 2 redshift divisions comparing the full 5 parameter model with the 4 parameter model that has constrained characteristic miscentering length $\sigma_{off} = 0.42 h \text{ Mpc}$.

This change does not alter significantly the results, but in the high-richness, low redshift, stacks (upper right) pair of panels, the small gap stacks tend to display a shift to higher concentrations when the miscentering length is fixed.

	5 parameter	4 parameter	3 parameter
Large ΔM_{1-2} , low z , high λ			
Masses [$10^{14}M_{\odot}$]	$1.6^{+1.0}_{-0.7}$	$1.8^{+1.1}_{-0.7}$	$1.8^{+1.0}_{-0.7}$
Concentrations	$8.9^{+6.5}_{-4.0}$	$9.6^{+6.2}_{-4.3}$	$9.9^{+6.0}_{-4.4}$
Small ΔM_{1-2} , low z , low λ			
Masses [$10^{14}M_{\odot}$]	$5.7^{+4.6}_{-2.2}$	$4.9^{+3.0}_{-1.7}$	$5.6^{+2.9}_{-1.5}$
Concentrations	$5.1^{+6.4}_{-3.2}$	$4.6^{+7.3}_{-3.0}$	$6.6^{+7.9}_{-2.9}$

Table 5.3: Comparison between quantiles out of different models, showing no significant difference

Overall, the models seems compatible one between another, however, a full model comparison was left for future work. The data does have low SNR we do not foresee that to yield a definitive better model. This and alternatives will be better discussed in the last chapter 6.

5.4 *Masses & Concentrations*

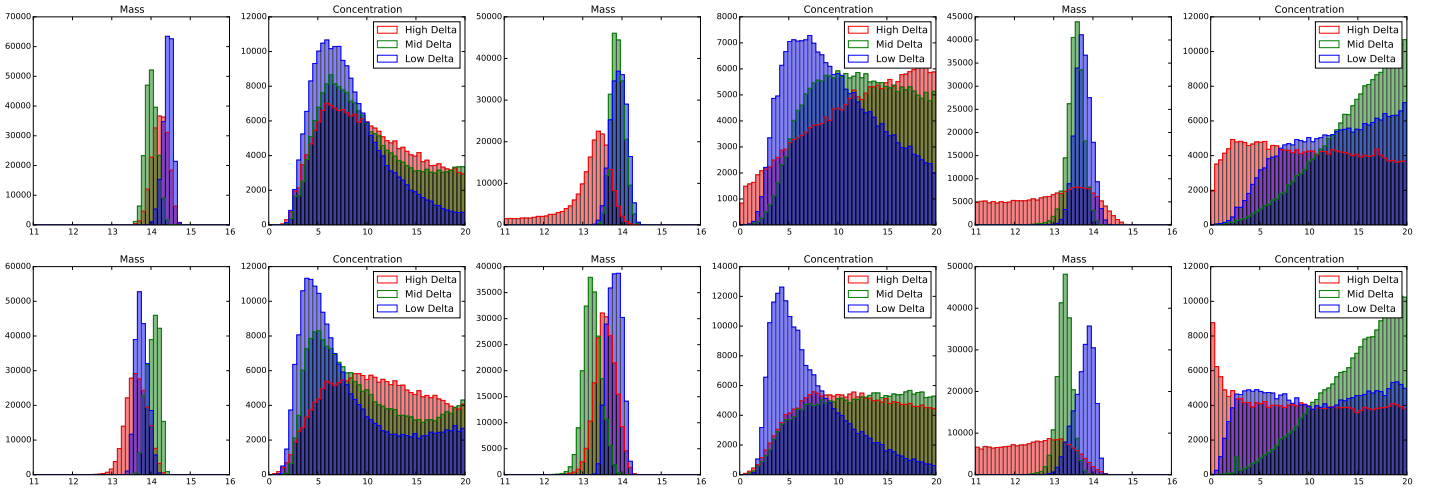


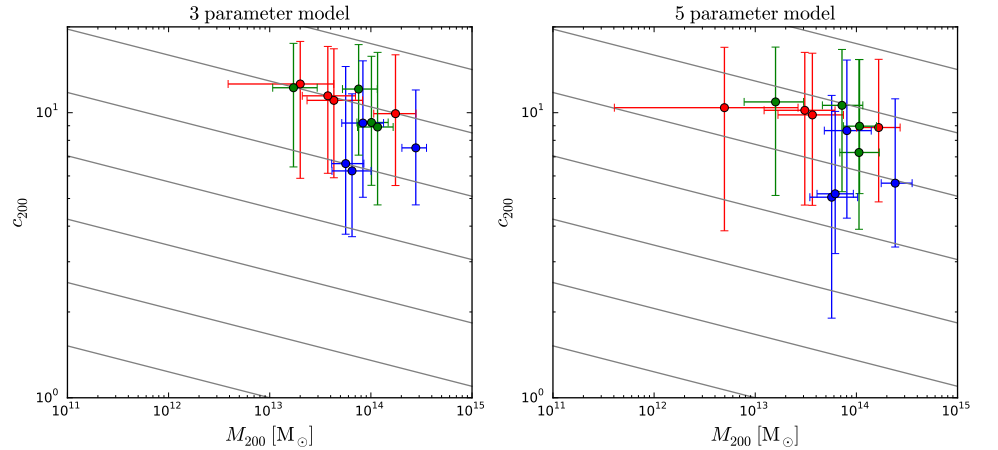
Figure 5.5: Posterior distributions for masses and concentrations of all stacks for ΔM_{1-2} , in the 3 parameter model. Each pair mass/concentration side by side represent a bin in richness and redshift, with colours distinguishing between magnitude gaps.

The mass and concentration posterior distributions represents the first objective result of this work (Fig. 5.5). It is usually the case that masses are better constrained with weak lensing studies than concentrations, as many other effects, such as miscentering, can introduce biases in concentrations and the radial position of the scale radius r_s is harder to constrain than the overall curve

height. All of the posteriors obtained for masses look sharp in logarithmic units of solar masses on the plots, relatively to the very wide priors adopted. The concentration parameters, on the other hand, display spread out posteriors. with peaks in lower values, but long, non-vanishing tails towards higher values, as the algorithm did not distinguish between concentrations and other effects. Converting masses back to the linear scale, however, we find that the average relative size of the 68%CL regions is roughly the same for both c_{200} and M_{200} , with $\langle \delta c_{200}/c_{200} \rangle = 0.22$ and $\langle \delta M_{200}/M_{200} \rangle = 0.24$.

The masses and concentrations we have obtained were compared to the $c-M$ relation of [Duffy et al. \[2008\]](#), as displayed in Fig. 5.6. For ΔM_{1-2} the c_{200} and M_{200} are moderately correlated within the 3-parameter model (Spearman $\rho = -0.56, p = 0.06$), but slightly less so with 4 or 5 parameters, ($\rho = -0.49, p = 0.10$) and ($\rho = -0.50, p = 0.09$), respectively. For ΔM_{1-4} , this correlation weakens considerably and reverses the tendency of diminishing in models with higher degrees of freedom with ($\rho = -0.09, p = 0.78$), ($\rho = -0.26, p = 0.41$), and ($\rho = -0.42, p = 0.17$) for 3, 4, and 5 parameter models respectively.

Figure 5.6: Masses and concentrations for the 2 lower redshift bins, using 5 and 3 parameters. The gray lines in the background are indications of the slope of the Duffy $c-M$ relation [Duffy et al. \[2008\]](#)



Using the [Duffy et al. \[2008\]](#) $c-M$ relation, we have calculated corrected parameter distributions for the concentrations for each

$\lambda \times z$ set, by using:

$$c_{200}^{corr} = c_{200} \left(\frac{M'_{200}}{M_{200}} \right)^{-0.13}, \quad (5.1)$$

where, for each set, we correct the intermediate and small ΔM concentrations by the mass (M'_{200}) of the one with the largest ΔM , so that concentrations can be compared in "equal-mass frame". Then, we have calculated the distribution of differences of randomly selected pairs of random draws of the c_{200}^{corr} distributions between the members of the set in all combinations (Fig. 5.7).

⁴ actually by counting how many results we have above zero

We integrate these distributions in $[0, \infty]^4$ to calculate the overall probability that the first quantity is larger than the second, to see how probable it is, from the data that samples with larger average magnitude gaps display larger average concentrations. In most cases, the high-low difference probability tends to be closer to the middle-low difference, whereas the high-middle concentration difference distribution seemed to be closer to the uniform random chance (0.5) that one is higher than the other (Tb. 5.4). However, none of these probabilities depart significantly from the average, in a way that would firmly suggest a difference of concentrations between samples of different magnitude gaps.

$\lambda > 30$	$P [c_{200}^{corr}(\Delta M_{1-2}^{high}) > c_{200}^{corr}(\Delta M_{1-2}^{low})] : 0.62$	$P [c_{200}^{corr}(\Delta M_{1-2}^{high}) > c_{200}^{corr}(\Delta M_{1-2}^{low})] : 0.55$
	$P [c_{200}^{corr}(\Delta M_{1-2}^{high}) > c_{200}^{corr}(\Delta M_{1-2}^{mid})] : 0.55$	$P [c_{200}^{corr}(\Delta M_{1-2}^{high}) > c_{200}^{corr}(\Delta M_{1-2}^{mid})] : 0.42$
	$P [c_{200}^{corr}(\Delta M_{1-2}^{mid}) > c_{200}^{corr}(\Delta M_{1-2}^{low})] : 0.57$	$P [c_{200}^{corr}(\Delta M_{1-2}^{mid}) > c_{200}^{corr}(\Delta M_{1-2}^{low})] : 0.63$
$\lambda < 30$	$P [c_{200}^{corr}(\Delta M_{1-2}^{high}) > c_{200}^{corr}(\Delta M_{1-2}^{low})] : 0.67$	$P [c_{200}^{corr}(\Delta M_{1-2}^{high}) > c_{200}^{corr}(\Delta M_{1-2}^{low})] : 0.72$
	$P [c_{200}^{corr}(\Delta M_{1-2}^{high}) > c_{200}^{corr}(\Delta M_{1-2}^{mid})] : 0.53$	$P [c_{200}^{corr}(\Delta M_{1-2}^{high}) > c_{200}^{corr}(\Delta M_{1-2}^{mid})] : 0.52$
	$P [c_{200}^{corr}(\Delta M_{1-2}^{mid}) > c_{200}^{corr}(\Delta M_{1-2}^{low})] : 0.64$	$P [c_{200}^{corr}(\Delta M_{1-2}^{mid}) > c_{200}^{corr}(\Delta M_{1-2}^{low})] : 0.72$
$0.2 < z < 0.4$		$0.4 < z < 0.6$

Finally, for the sake of completeness, we have performed Fisher's method [Mosteller and Fisher, 1948] to combine results of different redshifts and richness into a single probability. The method consists in asserting that a collection of k independent tests yielding probabilities p_i of rejecting the null hypothesis when it is true, is related to a χ^2 distribution with $2k$ degrees of freedom

Table 5.4: Probabilities for the parameters between two different magnitude gaps ΔM_{1-2} calculated by integrating the distribution of differences of random draws from the Markov chains, using the 3-parameter ($\sigma_{off} = 0.42h\text{Mpc}$, no CG baryonic component) model.

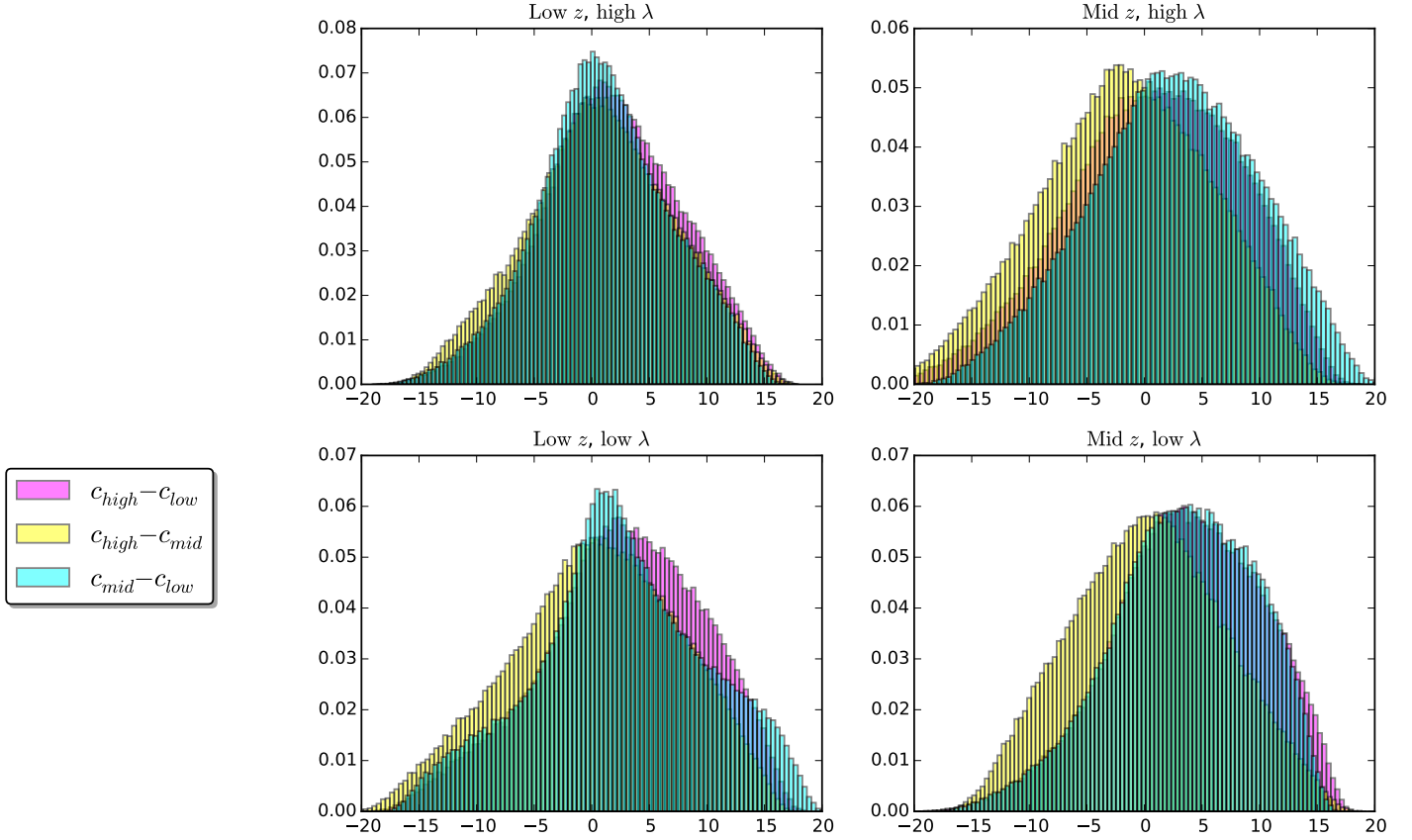


Figure 5.7: Posterior distributions for masses and concentrations of all stacks for ΔM_{1-2} , in the 3 parameter model.

through

$$\chi_{2k}^2 \sim -2 \sum_i^k \ln(p_i) \quad (5.2)$$

which can then be used to be calculated the new combined probability by

$$p = 1 - \frac{\gamma(k, x/2)}{\Gamma(k)} \quad (5.3)$$

where $\gamma(k, x)$ is the lower incomplete gamma function. We have used our probabilities P_i in the table 5.4 to interpret the $p_i = 1 - P_i$ as "p-values", and combined them into overall p s (table below) which remain far from statistically significant.

Table 5.5: Probabilities for rejecting one of the 4 null-hypotheses given that it is true of each set of concentration differences for each of the sets of concentration differences.

$c_{200}^{corr}(\Delta M_{1-2}^{high}) < c_{200}^{corr}(\Delta M_{1-2}^{low})$	$p = 0.60$
$c_{200}^{corr}(\Delta M_{1-2}^{high}) < c_{200}^{corr}(\Delta M_{1-2}^{mid})$	$p = 0.32$
$c_{200}^{corr}(\Delta M_{1-2}^{mid}) < c_{200}^{corr}(\Delta M_{1-2}^{low})$	$p = 0.59$

5.5 System Luminosities and M/L

Finally, we have investigated luminosities and mass-to-light ratios of systems following Khosroshahi et al. [2007], Proctor et al. [2011], in order search for differences between the larger and smaller magnitude gap populations. Using the calculated M_{200} we divide by the average i-band luminosity of each stack to look for any peculiarity among different stacks in magnitude gaps. We have not found any substantial differences between the populations. In the figure 5.8 we rank together all 3 different tracers of mass to each other.

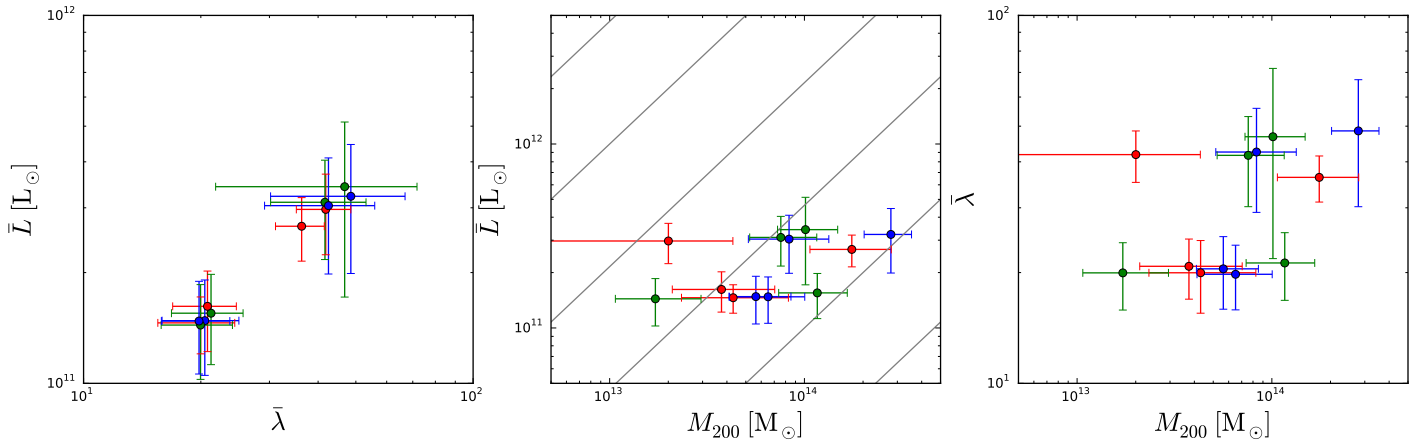
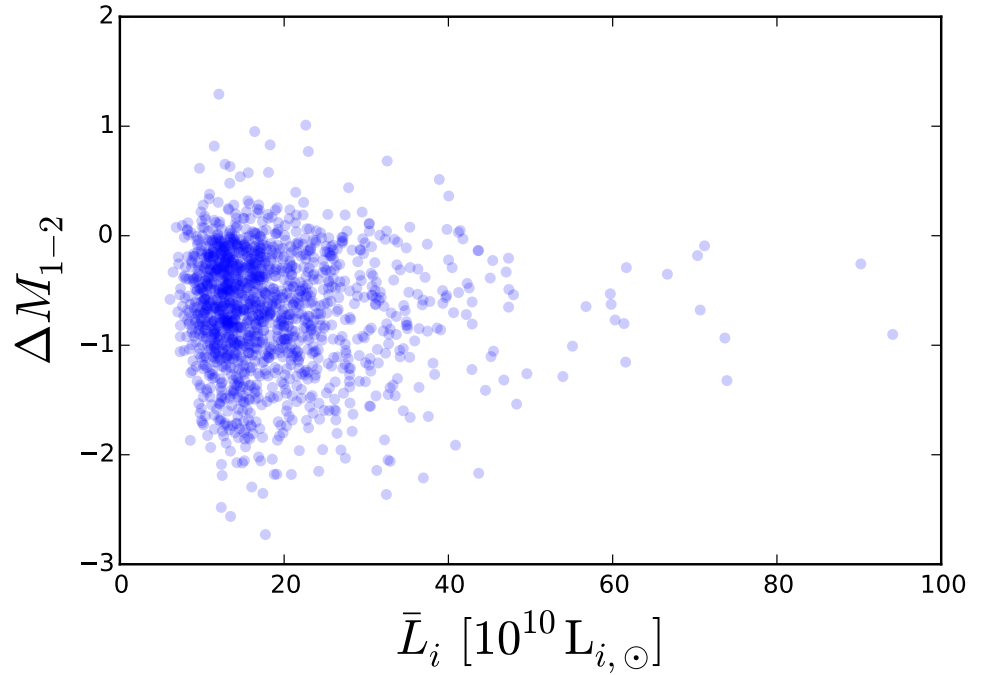


Figure 5.8: Results for the 3 main tracers of system mass: the M_{200} from weak lensing measurements, the average redMaPPer richness $\bar{\lambda}$ for each stacks, and the average luminosity \bar{L} , also from the redMaPPer catalogue.

Luminosities are highly correlated with richness ($\rho = 0.94, p = 0.01$), as one would expect not only since they are intrinsically connected, but also because luminosity is one of the filters of the redMaPPer algorithm, which tries to optimise member selection so that the richness λ is related to the mass. Between the other two mass tracers, M_{200}

Luminosities and richness, unlike the other stack derived parameters, can be directly compared to magnitude gaps object by object, as they are given by the redmapper catalogue. However no significant correlation was found between the two variables

Figure 5.9: Plot for all objects, magnitude gap ΔM_{1-2} by i-band luminosity by redMaPPer.



($\rho = -0.06$, $p = 0.02$).

5.6 Previous Literature Results

It is thought that the concentration parameter codifies some information about the local environment at the time of the collapse of halos and, consequently, information of their formation epoch [Khosroshahi et al., 2007, Navarro et al., 1995]. Accordingly, we expect that if magnitude gaps are indeed indicators of earlier mass accretion bias, that a higher magnitude gap would be correlated to higher concentrations, as concentration tends to be higher in dark matter halos with early formation epochs. After analysing our data, we do not find evidence neither to support nor to rule out these statements.

As it can be seen in figure 5.10, our points are placed in the middle way between the more massive clusters and the $c - M$ relations used by Khosroshahi et al. [2007], and the largest of the fossil groups. As our largest magnitude gap samples were not selected as optical fossil candidates, but only by having larger magnitude gaps among the total set, it is possible that they represent transitional ensembles between fossils and non-

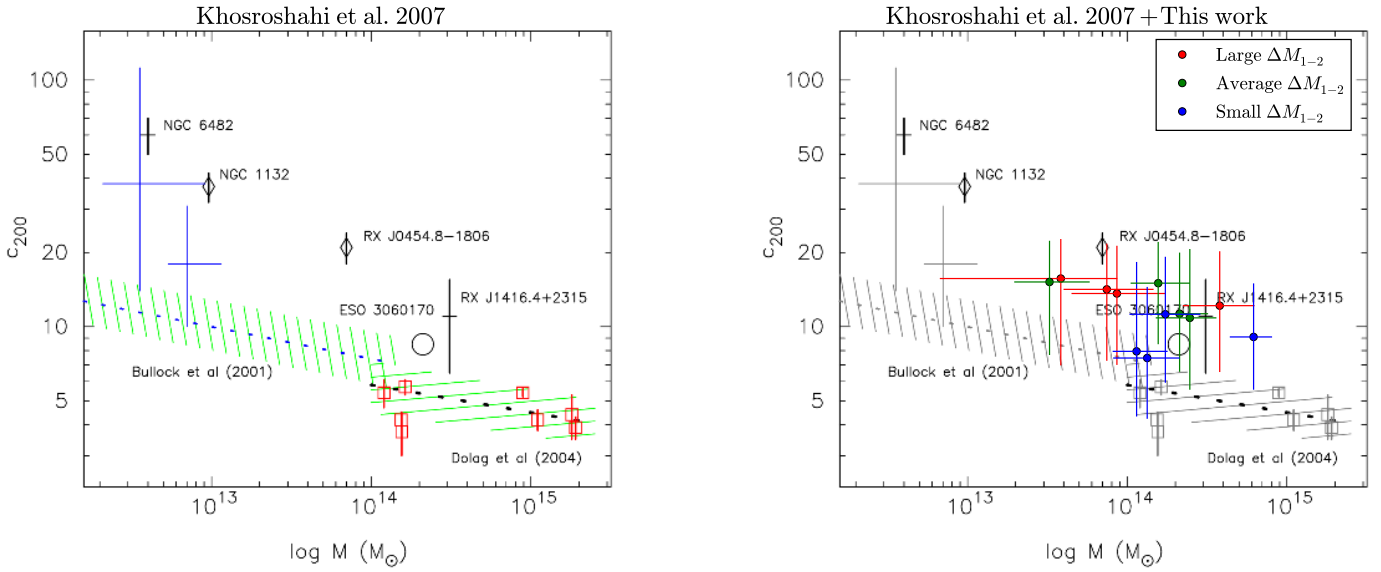


Figure 5.10: The $c - M$ relation of Khosroshahi et al. [2007], **Left:** caption from the original: Comparison between the mass concentration in fossils and non-fossil groups and clusters. Three fossils with resolved temperature profile and two isolated OLEGs (diamonds) are compared with non-fossil clusters (open squares) from Pratt and Arnaud [2005]. The expected values of the dark matter concentration and its variation with the halo mass from the numerical studies of Dolag et al. [2004] and Bullock et al. [2001] also are presented. The reasonable agreement between the non-fossils mass concentration from Pratt and Arnaud [2005] with the dark matter concentration from the study of Dolag et al. [2004] suggest that the excess concentration in fossils is due to their dark matter concentrations. In low mass end, two recent estimates (90%confidence) for the concentration of NGC 6482, after accounting for the baryonic matter (see Humphrey et al. [2006] for details) are also shown (blue) which again lie above the numerical expectations. **Right:** The superimposed points from this work.

fossils, on the concentration excess scale. However, our data is not statistically significant to directly support these affirmations.

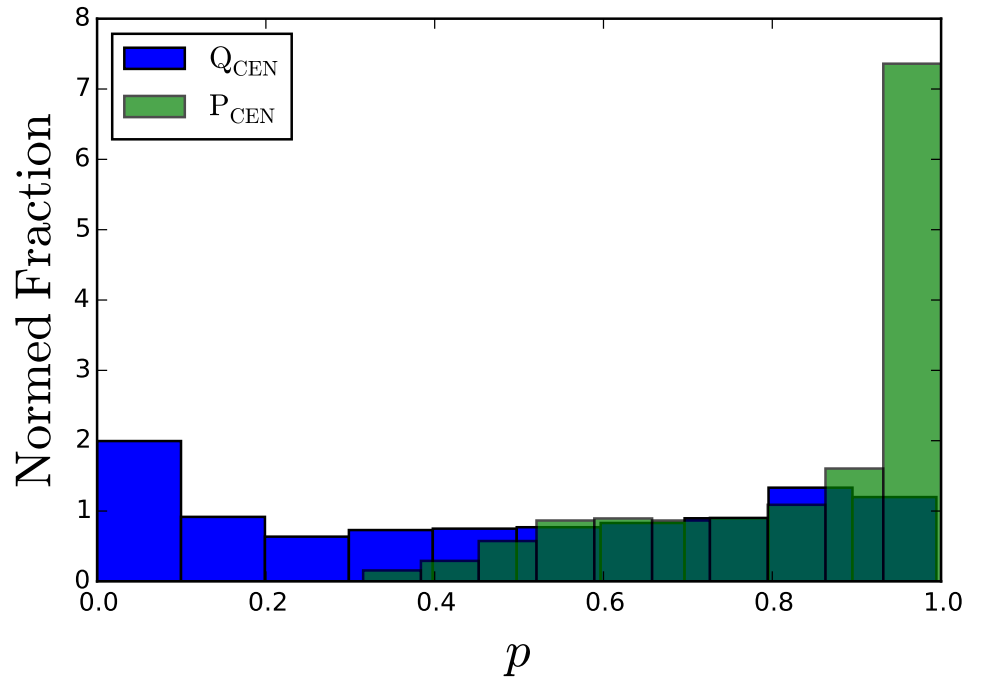
For mass-to-light ratios, there has been conflicting findings for fossil groups. [Vikhlinin et al., 1999], for example, finds high mass-to-light ratios for OLEGs (*Overluminous elliptical galaxies*), while Khosroshahi et al. [2004, 2007] found ratios that even if in the upper envelope of the distribution, are not altogether exceptional. As before, we find no evidence to support a correlation between magnitude gaps and higher M/L ratios.

5.7 A Note on Miscentering and Central Baryonic Component

The issue of cluster miscentering is of central importance in cross-correlation lensing studies. As seen in figure 4.7 on chapter 4 and in the literature [Ford et al., 2015, Johnston et al., 2007, Shan et al., 2015] a combination of miscentered profiles will alter the shear map radial distribution shape, lowering the inner radii average shears. As a result, large fractions of miscentered clusters will add important effects on the overall profile - and therefore on inferred mass and concentrations. For an example of crucial importance in this work, miscentering can mimic lower concentration values for NFW models [Ford et al., 2015].

In the light of these statements, it is tempting to try fitting both p_{cc} and σ_{off} as (non-nuisance) parameters on their own right, as a means to investigate the issue. However, a strong degeneracy between the p_{cc} and σ_{off} , and the lack of counts in each stack limits the constraining power considerably. Furthermore, projection effects in small stacks can also distort the shape of the profile in much the same way as miscentering does. This is expected to be mitigated by larger stacks, as it is a purely random effect, but not in the scale of the this work.

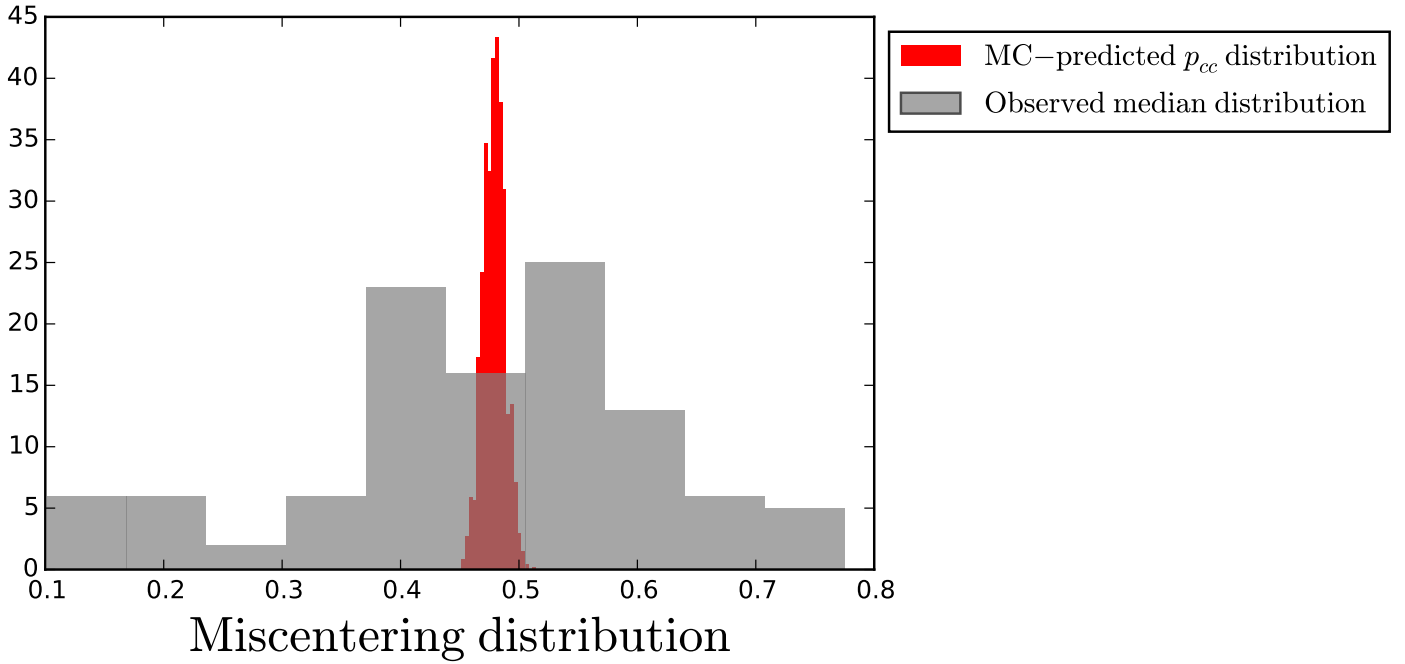
Figure 5.11: The probability distribution for the miscentered fraction is given by the distribution of correctly centred probabilities as calculated by the redMaPPer. The picture shows this distribution for the whole ensemble, but each stack has its own distribution calculated.



In the end, as in Johnston et al. [2007], we find very little power to for these results, and have thus tested for fixed parameter models. We have tried, however, to investigate the relationship between the probability of misidentified cluster centre from the redMaPPer catalogue with the calculated miscentered fraction parameter for our stacks.

The expected distribution of p_{cc} s can be properly evaluated by a Monte-Carlo method, by sorting out against the redMaPPer correct centring probability and checking the miscentered object fraction resulting from the tests, much in the same way we tried at first with magnitude gaps. The redMaPPer catalogue lists two probabilities for the 5 most-likely CG candidates: P_{CEN} and Q_{CEN} which are, respectively, the probability of the galaxy being

the correct centre galaxy, and the same probability, but now accounting for the fact that the CG may have not been listed as a cluster member by the algorithm. These second probabilities are then always lower, and sometimes much lower than the former as we can see in Fig. 5.11.



The result of the MC test of the expected distribution of $p_{cc}^{MC} = 0.47(15)$, taking into account the whole 1502 systems sample using the galaxy with the highest Q_{CEN} as the probability for each object, agrees closely to the average fitted $p_{cc} = 0.48(1)$ from the data. As such, we conclude this note by indicating that Q_{CEN} may better represent the actual probability of a redMaPPer cluster to be correctly centred, and that the expected fraction of miscentered clusters in a stack of redMaPPer objects can be well represented by a normal distribution $P(p_{cc}) = \mathcal{N}(\bar{p}_{cc} = 0.48, \sigma_{p_{cc}} = 0.01)$.

Figure 5.12: The probability distribution for the miscentered fraction is given by the distribution of correctly centred probabilities as calculated by the redMaPPer. The picture shows this distribution for the whole ensemble, but each stack has its own distribution calculated.

Conclusions and Perspectives

WE CONCLUDE THIS WORK by reviewing its main contents into few remarks and conclusions, and then we turn to examine future perspectives that these results suggest us.

After presenting the whole scenario, from the earliest cosmological times to the formation and evolution of galaxy systems, we posed the question about whether galaxy systems with overly dominant central galaxies are a peculiar population or just statistical outliers. In particular, we have investigated possible relationships between galaxy system magnitude gaps and masses, concentrations, and mass-to-light ratios.

From the information we have obtained, we draw the following conclusions:

- we have found inconclusive evidence on the subject of magnitude gaps and concentrations; and
- we have not found evidence to support that larger magnitude gap systems have greater mass-to-light ratios.

Had we found a significant correlation between the magnitude gaps and concentrations, it would have lent credibility to the idea that fossil groups and clusters really represent mature structures in the universe, as it is strongly believed that more relaxed clusters tend to be more concentrated, because of some of the effects listed in [chapter 2](#). However, the low number of systems present difficulties to evaluate their characteristics - a problem that near future surveys may overcome.

Throughout the course of this work, we have also developed an acquaintance with the modern technique of cross-correlation

lensing, and developed prototype software that can be easily adapted to future work in larger samples, such as that coming from the future J-PAS cluster catalogue [Benítez et al., 2015]. All the software will be available online with `IPYTHON` `NOTEBOOKS` for easy application and study.

As a next step, we plan to examine more closely the effect of selecting clusters by Q_{cen} from the redMaPPer catalogue on the fraction of correctly centred clusters p_{cc} in an attempt to constrain the model to better assess the parameters of our interest, namely M_{200} and c_{200} . Furthermore, we want to use Bayesian model comparison to evaluate the better option among the previously described models, with 3, 4, and 5 parameters.

Another complementary possibility, alternative to cross-correlation lensing, is to perform a multiple fit to all individual systems, still divided into redshift bins, simultaneously, where the log-likelihood is the sum of all the log-likelihoods for each system, and the fit constrain is a mass-concentration relation. The collection of these results and whatever finds we may encounter will be sent for publishing in the near future.

Part III

References and Index

Bibliography

- R. A. Alpher, H. Bethe, and G. Gamow. The Origin of Chemical Elements. *Physical Review*, 73:803--804, April 1948. DOI: 10.1103/PhysRev.73.803.
- E. A. Baltz, P. Marshall, and M. Oguri. Analytic models of plausible gravitational lens potentials. *Journal of Cosmology and Astroparticle Physics*, 1:015, January 2009. DOI: 10.1088/1475-7516/2009/01/015.
- J. M. Bardeen. Gauge-invariant cosmological perturbations. *Physical Review D*, 22:1882--1905, October 1980. DOI: 10.1103/PhysRevD.22.1882.
- M. Bartelmann and P. Schneider. Weak gravitational lensing. *Physics Report*, 340:291--472, January 2001. DOI: 10.1016/S0370-1573(00)00082-X.
- D. Baumann. TASI Lectures on Inflation. *ArXiv e-prints*, July 2009.
- N. Benítez, R. Dupke, M. Moles, L. Sodré, A. J. Cenarro, A. Marín Franch, K. Taylor, D. Cristóbal, A. Fernández-Soto, C. Mendes de Oliveira, J. Cepa-Nogué, L. R. Abramo, J. S. Alcaniz, R. Overzier, C. Hernández-Monteagudo, E. J. Alfaro, A. Kanaan, M. Carvano, R. R. R. Reis, and J-PAS collaboration. J-PAS: The Javalambre-Physics of the Accelerated Universe Astrophysical Survey. In A. J. Cenarro, F. Figueras, C. Hernández-Monteagudo, J. Trujillo Bueno, and L. Valdivielso, editors, *Highlights of Spanish Astrophysics VIII*, pages 148--153, May 2015.
- G. B. Brammer, P. G. van Dokkum, and P. Coppi. EAZY: A Fast, Public Photometric Redshift Code. *Astrophysical Journal*, 686: 1503--1513, October 2008. DOI: 10.1086/591786.

- J. S. Bullock, T. S. Kolatt, Y. Sigad, R. S. Somerville, A. V. Kravtsov, A. A. Klypin, J. R. Primack, and A. Dekel. Profiles of dark haloes: evolution, scatter and environment. *Monthly Notices of the Royal Astronomical Society*, 321:559--575, March 2001. DOI: 10.1046/j.1365-8711.2001.04068.x.
- D. Carter and N. Metcalfe. The morphology of clusters of galaxies. *Monthly Notices of the Royal Astronomical Society*, 191:325--337, May 1980.
- S. Chandrasekhar. Dynamical Friction. I. General Considerations: the Coefficient of Dynamical Friction. *Astrophysical Journal*, 97:255, March 1943. DOI: 10.1086/144517.
- O. Chwolson. Über eine mögliche Form fiktiver Doppelsterne. *Astronomische Nachrichten*, 221:329, June 1924.
- A. K. Cline. *FITPACK - A Software Package for Curve and Surface Fitting Employing Splines Under Tension*. 1974.
- D. Clowe, M. Bradač, A. H. Gonzalez, M. Markevitch, S. W. Randall, C. Jones, and D. Zaritsky. A Direct Empirical Proof of the Existence of Dark Matter. *Astrophysical Journal Letters*, 648:L109--L113, September 2006. DOI: 10.1086/508162.
- M. Colless, G. Dalton, S. Maddox, W. Sutherland, P. Norberg, S. Cole, J. Bland-Hawthorn, T. Bridges, R. Cannon, C. Collins, W. Couch, N. Cross, K. Deeley, R. De Propris, S. P. Driver, G. Efstathiou, R. S. Ellis, C. S. Frenk, K. Glazebrook, C. Jackson, O. Lahav, I. Lewis, S. Lumsden, D. Madgwick, J. A. Peacock, B. A. Peterson, I. Price, M. Seaborne, and K. Taylor. The 2dF Galaxy Redshift Survey: spectra and redshifts. *Monthly Notices of the Royal Astronomical Society*, 328:1039--1063, December 2001. DOI: 10.1046/j.1365-8711.2001.04902.x.
- A. Cooray and R. Sheth. Halo models of large scale structure. *Physics Reports*, 372:1--129, December 2002. DOI: 10.1016/S0370-1573(02)00276-4.
- D. J. Croton, V. Springel, S. D. M. White, G. De Lucia, C. S. Frenk, L. Gao, A. Jenkins, G. Kauffmann, J. F. Navarro, and N. Yoshida. The many lives of active galactic nuclei: cooling

- flows, black holes and the luminosities and colours of galaxies. *Monthly Notices of the Royal Astronomical Society*, 365:11--28, January 2006. DOI: 10.1111/j.1365-2966.2005.09675.x.
- E. S. Cypriano, C. L. Mendes de Oliveira, and L. Sodré, Jr. Velocity Dispersion, Mass, and the Luminosity Function of the Fossil Cluster RX J1416.4+2315. *Astronomical Journal*, 132: 514--520, August 2006. DOI: 10.1086/505044.
- A. Dariush, H. G. Khosroshahi, T. J. Ponman, F. Pearce, S. Raychaudhury, and W. Hartley. The mass assembly of fossil groups of galaxies in the Millennium simulation. *Monthly Notices of the Royal Astronomical Society*, 382:433--442, November 2007. DOI: 10.1111/j.1365-2966.2007.12385.x.
- A. A. Dariush, S. Raychaudhury, T. J. Ponman, H. G. Khosroshahi, A. J. Benson, R. G. Bower, and F. Pearce. The mass assembly of galaxy groups and the evolution of the magnitude gap. *Monthly Notices of the Royal Astronomical Society*, 405:1873--1887, July 2010. DOI: 10.1111/j.1365-2966.2010.16569.x.
- S. Dodelson and G. Efstathiou. Modern Cosmology. *Physics Today*, 57:60--61, July 2004. DOI: 10.1063/1.1784308.
- K. Dolag, M. Bartelmann, F. Perrotta, C. Baccigalupi, L. Moscardini, M. Meneghetti, and G. Tormen. Numerical study of halo concentrations in dark-energy cosmologies. *Astronomy & Astrophysics*, 416:853--864, March 2004. DOI: 10.1051/0004-6361:20031757.
- E. D'Onghia and G. Lake. Cold Dark Matter's Small-Scale Crisis Grows Up. *Astrophysical Journal*, 612:628--632, September 2004. DOI: 10.1086/422794.
- E. D'Onghia, J. Sommer-Larsen, A. D. Romeo, A. Burkert, K. Pedersen, L. Portinari, and J. Rasmussen. The Formation of Fossil Galaxy Groups in the Hierarchical Universe. *Astrophysical Journal Letters*, 630:L109--L112, September 2005. DOI: 10.1086/491651.
- A. Dressler. The Evolution of Galaxies in Clusters. *Annual*

- Review of Astronomy and Astrophysics*, 22:185--222, 1984.
DOI: 10.1146/annurev.aa.22.090184.001153.
- J. Dubinski. The Origin of the Brightest Cluster Galaxies. *Astrophysical Journal*, 502:141--149, July 1998. DOI: 10.1086/305901.
- J. Dubinski and R. G. Carlberg. The structure of cold dark matter halos. *Astrophysical Journal*, 378:496--503, September 1991. DOI: 10.1086/170451.
- A. R. Duffy, J. Schaye, S. T. Kay, and C. Dalla Vecchia. Dark matter halo concentrations in the Wilkinson Microwave Anisotropy Probe year 5 cosmology. *Monthly Notices of the Royal Astronomical Society*, 390:L64--L68, October 2008. DOI: 10.1111/j.1745-3933.2008.00537.x.
- F. Durret, C. Adami, E. Bertin, J. Hao, I. Márquez, N. Martinet, S. Maurogordato, T. Sauvaget, N. Sceph, and M. P. Ulmer. Galaxy clusters in the SDSS Stripe 82. In J. Ballet, F. Martins, F. Bournaud, R. Monier, and C. Reylé, editors, *SF2A-2014: Proceedings of the Annual meeting of the French Society of Astronomy and Astrophysics*, pages 315--319, December 2014.
- F. W. Dyson, A. S. Eddington, and C. Davidson. A Determination of the Deflection of Light by the Sun's Gravitational Field, from Observations Made at the Total Eclipse of May 29, 1919. *Royal Society of London Philosophical Transactions Series A*, 220:291--333, 1920. DOI: 10.1098/rsta.1920.0009.
- A. S. Eddington. *Space, time and gravitation. an outline of the general relativity theory*. 1920.
- J. Ehlers, P. Geren, and R. K. Sachs. Isotropic solutions of the Einstein-Liouville equations. *Journal of Mathematical Physics*, 9:1344--1349, 1968. DOI: 10.1063/1.1664720.
- A. Einstein. Lens-Like Action of a Star by the Deviation of Light in the Gravitational Field. *Science*, 84:506--507, December 1936. DOI: 10.1126/science.84.2188.506.

- G. F. R. Ellis. Relativistic Cosmology. In R. K. Sachs, editor, *General Relativity and Cosmology*, pages 104--182, 1971.
- G. F. R. Ellis. On the Raychaudhuri equation. *Pramana*, 69:15, July 2007. DOI: 10.1007/s12043-007-0107-4.
- G. F. R. Ellis and H. van Elst. Cosmological Models (Cargèse lectures 1998). In M. Lachièze-Rey, editor, *NATO Advanced Science Institutes (ASI) Series C*, volume 541 of *NATO Advanced Science Institutes (ASI) Series C*, pages 1--116, 1999.
- G. F. R. Ellis, R. Maartens, and M. A. H. MacCallum. *Relativistic Cosmology*. March 2012.
- T. Erben, H. Hildebrandt, L. Miller, L. van Waerbeke, C. Heymans, H. Hoekstra, T. D. Kitching, Y. Mellier, J. Benjamin, C. Blake, C. Bonnett, O. Cordes, J. Coupon, L. Fu, R. Gavazzi, B. Gillis, E. Grocutt, S. D. J. Gwyn, K. Holhjem, M. J. Hudson, M. Kilbinger, K. Kuijken, M. Milkeraitis, B. T. P. Rowe, T. Schrabback, E. Semboloni, P. Simon, M. Smit, O. Toader, S. Vafaei, E. van Uitert, and M. Velander. CFHTLenS: the Canada-France-Hawaii Telescope Lensing Survey - imaging data and catalogue products. *Monthly Notices of the Royal Astronomical Society*, 433:2545--2563, August 2013. DOI: 10.1093/mnras/stt928.
- C. W. F. Everitt, D. B. Debra, B. W. Parkinson, J. P. Turneare, J. W. Conklin, M. I. Heifetz, G. M. Keiser, A. S. Silbergleit, T. Holmes, J. Kolodziejczak, M. Al-Meshari, J. C. Mester, B. Muhlfelder, V. G. Solomonik, K. Stahl, P. W. Worden, Jr., W. Bencze, S. Buchman, B. Clarke, A. Al-Jadaan, H. Al-Jibreen, J. Li, J. A. Lipa, J. M. Lockhart, B. Al-Suwaidan, M. Taber, and S. Wang. Gravity Probe B: Final Results of a Space Experiment to Test General Relativity. *Physical Review Letters*, 106(22): 221101, June 2011. DOI: 10.1103/PhysRevLett.106.221101.
- A. C. Fabian. Cooling Flows in Clusters of Galaxies. *Annual Review of Astronomy and Astrophysics*, 32:277--318, 1994. DOI: 10.1146/annurev.aa.32.090194.001425.
- V. Fock. *The Theory of Space, Time and Gravitation*. Elsevier Science, 1955/2015. ISBN 9781483184906.

- J. Ford, L. Van Waerbeke, M. Milkeraitis, C. Laigle, H. Hildebrandt, T. Erben, C. Heymans, H. Hoekstra, T. Kitching, Y. Mellier, L. Miller, A. Choi, J. Coupon, L. Fu, M. J. Hudson, K. Kuijken, N. Robertson, B. Rowe, T. Schrabback, and M. Velander. CFHTLenS: a weak lensing shear analysis of the 3D-Matched-Filter galaxy clusters. *Monthly Notices of the Royal Astronomical Society*, 447:1304–1318, February 2015. DOI: 10.1093/mnras/stu2545.
- D. Foreman-Mackey, D. W. Hogg, D. Lang, and J. Goodman. emcee: The MCMC Hammer. *Publications of the Astronomical Society of the Pacific*, 125:306–312, March 2013. DOI: 10.1086/670067.
- R. Gavazzi, T. Treu, J. D. Rhodes, L. V. E. Koopmans, A. S. Bolton, S. Burles, R. J. Massey, and L. A. Moustakas. The Sloan Lens ACS Survey. IV. The Mass Density Profile of Early-Type Galaxies out to 100 Effective Radii. *Astrophysical Journal*, 667:176–190, September 2007. DOI: 10.1086/519237.
- M. Girardi, E. Escalera, D. Fadda, G. Giuricin, F. Mardirossian, and M. Mezzetti. Optical Substructures in 48 Galaxy Clusters: New Insights from a Multiscale Analysis. *Astrophysical Journal*, 482:41–62, June 1997.
- J. Goodman and J. Weare. Ensemble samplers with affine invariance. *Communications in Applied Mathematics & Computational Science*, 5:65–80, January 2010.
- G. Gozaliasl, A. Finoguenov, H. G. Khosroshahi, M. Mirkazemi, M. Salvato, D. M. Z. Jassur, G. Erfanianfar, P. Popesso, M. Tanaka, M. Lerchster, J. P. Kneib, H. J. McCracken, Y. Mellier, E. Egami, M. J. Pereira, F. Brimiouille, T. Erben, and S. Seitz. Mining the gap: evolution of the magnitude gap in X-ray galaxy groups from the 3-square-degree XMM coverage of CFHTLS. *Astronomy and Astrophysics*, 566:A140, June 2014. DOI: 10.1051/0004-6361/201322459.
- J. E. Gunn and J. R. Gott, III. On the Infall of Matter Into Clusters of Galaxies and Some Effects on Their Evolution. *Astrophysical Journal*, 176:1, August 1972. DOI: 10.1086/151605.

- C. D. Harrison, C. J. Miller, J. W. Richards, E. J. Lloyd-Davies, B. Hoyle, A. K. Romer, N. Mehrrens, M. Hilton, J. P. Stott, D. Capozzi, C. A. Collins, P.-J. Deadman, A. R. Liddle, M. Sahlén, S. A. Stanford, and P. T. P. Viana. The XMM Cluster Survey: The Stellar Mass Assembly of Fossil Galaxies. *Astrophysical Journal*, 752:12, June 2012. DOI: 10.1088/0004-637X/752/1/12.
- D. Harvey, R. Massey, T. Kitching, A. Taylor, and E. Tittley. The nongravitational interactions of dark matter in colliding galaxy clusters. *Science*, 347:1462--1465, March 2015. DOI: 10.1126/science.1261381.
- S. W. Hawking and G. F. R. Ellis. *The Large-scale Structure of Space-time*. 1973.
- S. W. Hawking and R. Penrose. The Singularities of Gravitational Collapse and Cosmology. *Royal Society of London Proceedings Series A*, 314:529--548, January 1970. DOI: 10.1098/rspa.1970.0021.
- A. P. Hearin, A. R. Zentner, J. A. Newman, and A. A. Berlind. Mind the gap: tightening the mass-richness relation with magnitude gaps. *Monthly Notices of the Royal Astronomical Society*, 430:1238--1246, April 2013. DOI: 10.1093/mnras/sts699.
- G. Hinshaw, D. Larson, E. Komatsu, D. N. Spergel, C. L. Bennett, J. Dunkley, M. R.olta, M. Halpern, R. S. Hill, N. Odegard, L. Page, K. M. Smith, J. L. Weiland, B. Gold, N. Jarosik, A. Kogut, M. Limon, S. S. Meyer, G. S. Tucker, E. Wollack, and E. L. Wright. Nine-year Wilkinson Microwave Anisotropy Probe (WMAP) Observations: Cosmological Parameter Results. *Astrophysical Journal Supplements*, 208: 19, October 2013. DOI: 10.1088/0067-0049/208/2/19.
- E. Hubble. A Relation between Distance and Radial Velocity among Extra-Galactic Nebulae. *Proceedings of the National Academy of Science*, 15:168--173, March 1929. DOI: 10.1073/pnas.15.3.168.
- P. J. Humphrey, D. A. Buote, F. Gastaldello, L. Zappacosta, J. S. Bullock, F. Brighenti, and W. G. Mathews. A Chandra View of

- Dark Matter in Early-Type Galaxies. *Astrophysical Journal*, 646:899--918, August 2006. DOI: 10.1086/505019.
- B. Jain, A. Joyce, R. Thompson, A. Upadhye, J. Battat, P. Brax, A.-C. Davis, C. de Rham, S. Dodelson, A. Erickcek, G. Gabadadze, W. Hu, L. Hui, D. Hutnerer, M. Kamionkowski, J. Khoury, K. Koyama, B. Li, E. Linder, F. Schmidt, R. Scoccimarro, G. Starkman, C. Stubbs, M. Takada, A. Tolley, M. Trodden, J.-P. Uzan, V. Vikram, A. Weltman, M. Wyman, D. Zaritsky, and G. Zhao. Novel Probes of Gravity and Dark Energy. *ArXiv e-prints*, September 2013.
- D. E. Johnston, E. S. Sheldon, R. H. Wechsler, E. Rozo, B. P. Koester, J. A. Frieman, T. A. McKay, A. E. Evrard, M. R. Becker, and J. Annis. Cross-correlation Weak Lensing of SDSS galaxy Clusters II: Cluster Density Profiles and the Mass--Richness Relation. *ArXiv e-prints*, September 2007.
- L. R. Jones, T. J. Ponman, and D. A. Forbes. Multiwavelength observations of an evolved galaxy group: an end-point of galaxy merging? *Monthly Notices of the Royal Astronomical Society*, 312:139--150, February 2000. DOI: 10.1046/j.1365-8711.2000.03118.x.
- L. R. Jones, T. J. Ponman, A. Horton, A. Babul, H. Ebeling, and D. J. Burke. The nature and space density of fossil groups of galaxies. *Monthly Notices of the Royal Astronomical Society*, 343:627--638, August 2003. DOI: 10.1046/j.1365-8711.2003.06702.x.
- F. Kahlhoefer, K. Schmidt-Hoberg, M. T. Frandsen, and S. Sarkar. Colliding clusters and dark matter self-interactions. *Monthly Notices of the Royal Astronomical Society*, 437:2865--2881, January 2014. DOI: 10.1093/mnras/stt2097.
- N. Katz. Dissipationless collapse in an expanding universe. *Astrophysical Journal*, 368:325--336, February 1991. DOI: 10.1086/169696.
- H. G. Khosroshahi, L. R. Jones, and T. J. Ponman. An old galaxy group: Chandra X-ray observations of the nearby fossil group NGC 6482. *Monthly Notices of the Royal Astronomical*

- Society*, 349:1240--1250, April 2004. DOI: 10.1111/j.1365-2966.2004.07575.x.
- H. G. Khosroshahi, T. J. Ponman, and L. R. Jones. The central elliptical galaxy in fossil groups and formation of brightest cluster galaxies. *Monthly Notices of the Royal Astronomical Society*, 372:L68--L72, October 2006. DOI: 10.1111/j.1745-3933.2006.00228.x.
- H. G. Khosroshahi, T. J. Ponman, and L. R. Jones. Scaling relations in fossil galaxy groups. *Monthly Notices of the Royal Astronomical Society*, 377:595--606, May 2007. DOI: 10.1111/j.1365-2966.2007.11591.x.
- T. D. Kitching, L. Miller, C. E. Heymans, L. van Waerbeke, and A. F. Heavens. Bayesian galaxy shape measurement for weak lensing surveys - II. Application to simulations. *Monthly Notices of the Royal Astronomical Society*, 390:149--167, October 2008. DOI: 10.1111/j.1365-2966.2008.13628.x.
- A. A. Klypin, S. Trujillo-Gomez, and J. Primack. Dark Matter Halos in the Standard Cosmological Model: Results from the Bolshoi Simulation. *Astrophysical Journal*, 740:102, October 2011. DOI: 10.1088/0004-637X/740/2/102.
- B. P. Koester, T. A. McKay, J. Annis, R. H. Wechsler, A. E. Evrard, E. Rozo, L. Bleem, E. S. Sheldon, and D. Johnston. MaxBCG: A Red-Sequence Galaxy Cluster Finder. *Astrophysical Journal*, 660:221--238, May 2007. DOI: 10.1086/512092.
- A. V. Kravtsov and S. Borgani. Formation of Galaxy Clusters. *Annual Review of Astronomy and Astrophysics*, 50:353--409, September 2012. DOI: 10.1146/annurev-astro-081811-125502.
- J. Krempec-Krygier and B. Krygier. Interaction of Abell Cluster 2063 and the Group of Galaxies MKW3s. *Acta Astronomica*, 49:403--420, September 1999.
- M. Lachieze-Rey and J. Luminet. Cosmic topology. *Physics Reports*, 254:135--214, March 1995. DOI: 10.1016/0370-1573(94)00085-H.

- S. M. LaMassa, C. M. Urry, E. Glikman, N. Cappelluti, A. Comastri, H. Boehringer, G. T. Richards, and S. S. Murray. Stripe 82 X: X-ray Survey of SDSS Stripe 82. In *AAS/High Energy Astrophysics Division*, volume 13 of *AAS/High Energy Astrophysics Division*, page 109.05, April 2013.
- A. Lewis and A. Challinor. Evolution of cosmological dark matter perturbations. *Physical Review D*, 66(2):023531, July 2002. DOI: 10.1103/PhysRevD.66.023531.
- M. Lima and W. Hu. Self-calibration of cluster dark energy studies: Observable-mass distribution. *Physical Review D*, 72(4):043006, August 2005. DOI: 10.1103/PhysRevD.72.043006.
- G.B. Lima Neto. *Astronomia Extragaláctica*. 2014.
- D. Lynden-Bell. Statistical mechanics of violent relaxation in stellar systems. *Monthly Notices of the Royal Astronomical Society*, 136:101, 1967.
- R. Lynds and V. Petrosian. Giant Luminous Arcs in Galaxy Clusters. In *Bulletin of the American Astronomical Society*, volume 18 of *Bulletin of the American Astronomical Society*, page 1014, September 1986.
- R. Mandelbaum. *Weak gravitational lensing analysis of Sloan Digital Sky Survey data*. PhD thesis, Princeton University, 2006.
- A. B. Mantz, S. W. Allen, R. G. Morris, R. W. Schmidt, A. von der Linden, and O. Urban. Cosmology and astrophysics from relaxed galaxy clusters - I. Sample selection. *Monthly Notices of the Royal Astronomical Society*, 449:199--219, May 2015. DOI: 10.1093/mnras/stv219.
- Julian Merten. A Combining Weak and Strong Lensing for Galaxy-Cluster Mass Reconstructions. Master's thesis, University of Heidelberg, 2008.
- Julian Merten. *An advanced method to recover the mass distribution of galaxy clusters*. PhD thesis, University of Heidelberg, 2010.

- P. Meszaros. The behaviour of point masses in an expanding cosmological substratum. *Astronomy & Astrophysics*, 37: 225--228, December 1974.
- G. Meylan, P. Jetzer, P. North, P. Schneider, C. S. Kochanek, and J. Wambsganss, editors. *Gravitational Lensing: Strong, Weak and Micro*, 2006.
- L. Miller, T. D. Kitching, C. Heymans, A. F. Heavens, and L. van Waerbeke. Bayesian galaxy shape measurement for weak lensing surveys - I. Methodology and a fast-fitting algorithm. *Monthly Notices of the Royal Astronomical Society*, 382:315--324, November 2007. DOI: 10.1111/j.1365-2966.2007.12363.x.
- L. Miller, C. Heymans, T. D. Kitching, L. van Waerbeke, T. Erben, H. Hildebrandt, H. Hoekstra, Y. Mellier, B. T. P. Rowe, J. Coupon, J. P. Dietrich, L. Fu, J. Harnois-Déraps, M. J. Hudson, M. Kilbinger, K. Kuijken, T. Schrabback, E. Semboloni, S. Vafaei, and M. Velander. Bayesian galaxy shape measurement for weak lensing surveys - III. Application to the Canada-France-Hawaii Telescope Lensing Survey. *Monthly Notices of the Royal Astronomical Society*, 429:2858--2880, March 2013. DOI: 10.1093/mnras/sts454.
- C. W. Misner, K. S. Thorne, and J. A. Wheeler. *Gravitation*. 1973.
- B. Moraes, J.-P. Kneib, A. Leauthaud, M. Makler, L. Van Waerbeke, K. Bundy, T. Erben, C. Heymans, H. Hildebrandt, L. Miller, H. Y. Shan, D. Woods, A. Charbonnier, and M. E. Pereira. The CFHT/MegaCam Stripe-82 Survey. In *Revista Mexicana de Astronomia y Astrofisica Conference Series*, volume 44 of *Revista Mexicana de Astronomia y Astrofisica*, vol. 27, pages 202--203, October 2014.
- Frederick Mosteller and R. A. Fisher. Questions and answers. *The American Statistician*, 2(5):pp. 30--31, 1948. ISSN 00031305. URL <http://www.jstor.org/stable/2681650>.
- J. S. Mulchaey and A. I. Zabludoff. The Isolated Elliptical NGC 1132: Evidence for a Merged Group of Galaxies? *Astrophysical Journal*, 514:133--137, March 1999. DOI: 10.1086/306952.

- R. Narayan, R. Blandford, and R. Nityananda. Multiple imaging of quasars by galaxies and clusters. *Nature*, 310:112--115, July 1984. DOI: 10.1038/310112a0.
- J. F. Navarro, C. S. Frenk, and S. D. M. White. The assembly of galaxies in a hierarchically clustering universe. *Monthly Notices of the Royal Astronomical Society*, 275:56--66, July 1995.
- J. F. Navarro, C. S. Frenk, and S. D. M. White. The Structure of Cold Dark Matter Halos. *Astrophysical Journal*, 462:563, May 1996. DOI: 10.1086/177173.
- J. F. Navarro, C. S. Frenk, and S. D. M. White. A Universal Density Profile from Hierarchical Clustering. *Astrophysical Journal*, 490:493--508, December 1997.
- E. Noether. Invariante Variationsprobleme. *Nachrichten von der Gesellschaft der Wissenschaften zu Göttingen, Mathematisch-Physikalische Klasse*, 1:235--257, July 1918.
- A. L. O'Mill, F. Duplancic, D. García Lambas, and L. Sodré, Jr. Photometric redshifts and k-corrections for the Sloan Digital Sky Survey Data Release 7. *Monthly Notices of the Royal Astronomical Society*, 413:1395--1408, May 2011. DOI: 10.1111/j.1365-2966.2011.18222.x.
- B. Paczynski. Giant luminous arcs discovered in two clusters of galaxies. *Nature*, 325:572--573, February 1987. DOI: 10.1038/325572a0.
- T. Padmanabhan. *Structure Formation in the Universe*. May 1993.
- A. Paranjape and R. K. Sheth. The luminosities of the brightest cluster galaxies and brightest satellites in SDSS groups. *Monthly Notices of the Royal Astronomical Society*, 423:1845--1855, June 2012. DOI: 10.1111/j.1365-2966.2012.21008.x.
- J. A. Peacock. Large-scale surveys and cosmic structure. *ArXiv Astrophysics e-prints*, September 2003.
- P. J. E. Peebles. The origin of galaxies and clusters of galaxies. *Science*, 224:1385--1391, June 1984. DOI: 10.1126/science.224.4656.1385.

- Planck Collaboration, P. A. R. Ade, N. Aghanim, M. Arnaud, M. Ashdown, J. Aumont, C. Baccigalupi, A. J. Banday, R. B. Barreiro, J. G. Bartlett, and et al. Planck 2015 results. XIII. Cosmological parameters. *ArXiv e-prints*, February 2015.
- T. J. Ponman, D. J. Allan, L. R. Jones, M. Merrifield, I. M. McHardy, H. J. Lehto, and G. A. Luppino. A possible fossil galaxy group. *Nature*, 369:462--464, June 1994. DOI: 10.1038/369462a0.
- G. W. Pratt and M. Arnaud. XMM-Newton observations of three poor clusters: Similarity in dark matter and entropy profiles down to low mass. *Astronomy & Astrophysics*, 429:791--806, January 2005. DOI: 10.1051/0004-6361:20041479.
- W. H. Press and P. Schechter. Formation of Galaxies and Clusters of Galaxies by Self-Similar Gravitational Condensation. *Astrophysical Journal*, 187:425--438, February 1974. DOI: 10.1086/152650.
- R. N. Proctor, C. M. de Oliveira, R. Dupke, R. L. de Oliveira, E. S. Cypriano, E. D. Miller, and E. Rykoff. On the mass-to-light ratios of fossil groups. Are they simply dark clusters? *Monthly Notices of the Royal Astronomical Society*, 418: 2054--2073, December 2011. DOI: 10.1111/j.1365-2966.2011.19625.x.
- S. Refsdal. The gravitational lens effect. *Monthly Notices of the Royal Astronomical Society*, 128:295, 1964a.
- S. Refsdal. On the possibility of determining Hubble's parameter and the masses of galaxies from the gravitational lens effect. *Monthly Notices of the Royal Astronomical Society*, 128:307, 1964b.
- R. R. R. Reis, M. Soares-Santos, J. Annis, S. Dodelson, J. Hao, D. Johnston, J. Kubo, H. Lin, H.-J. Seo, and M. Simet. The Sloan Digital Sky Survey Co-add: A Galaxy Photometric Redshift Catalog. *Astrophysical Journal*, 747:59, March 2012. DOI: 10.1088/0004-637X/747/1/59.
- A. G. Riess, A. V. Filippenko, P. Challis, A. Clocchiatti, A. Diercks, P. M. Garnavich, R. L. Gilliland, C. J. Hogan,

- S. Jha, R. P. Kirshner, B. Leibundgut, M. M. Phillips, D. Reiss, B. P. Schmidt, R. A. Schommer, R. C. Smith, J. Spyromilio, C. Stubbs, N. B. Suntzeff, and J. Tonry. Observational Evidence from Supernovae for an Accelerating Universe and a Cosmological Constant. *AJ*, 116:1009--1038, September 1998. DOI: 10.1086/300499.
- E. S. Rykoff, B. P. Koester, E. Rozo, J. Annis, A. E. Evrard, S. M. Hansen, J. Hao, D. E. Johnston, T. A. McKay, and R. H. Wechsler. Robust Optical Richness Estimation with Reduced Scatter. *Astrophysical Journal*, 746:178, February 2012. DOI: 10.1088/0004-637X/746/2/178.
- E. S. Rykoff, E. Rozo, M. T. Busha, C. E. Cunha, A. Finoguenov, A. Evrard, J. Hao, B. P. Koester, A. Leauthaud, B. Nord, M. Pierre, R. Reddick, T. Sadibekova, E. S. Sheldon, and R. H. Wechsler. redMaPPer. I. Algorithm and SDSS DR8 Catalog. *Astrophysical Journal*, 785:104, April 2014. DOI: 10.1088/0004-637X/785/2/104.
- A. D. Sakharov. SPECIAL ISSUE: Violation of CP in variance, C asymmetry, and baryon asymmetry of the universe. *Soviet Physics Uspekhi*, 1991.
- A. Sandage. Current Problems in the Extragalactic Distance Scale. *Astrophysical Journal*, 127:513, May 1958. DOI: 10.1086/146483.
- P. Schechter. An analytic expression for the luminosity function for galaxies. *Astrophysical Journal*, 203:297--306, January 1976. DOI: 10.1086/154079.
- M. Schmidt. 3C 273 : A Star-Like Object with Large Red-Shift. *Nature*, 197:1040, March 1963. DOI: 10.1038/1971040a0.
- P. Schneider. *Extragalactic Astronomy and Cosmology*. 2006.
- P. Schneider, J. Ehlers, and E. E. Falco. *Gravitational Lenses*. 1992.
- H. Shan, J.-P. Kneib, R. Li, J. Comparat, T. Erben, M. Makler, B. Moraes, L. Van Waerbeke, J. E. Taylor, and A. Charbonnier. The Mass-Concentration Relation and the Stellar-to-Halo Mass Ratio in the CFHT Stripe 82 Survey. *ArXiv e-prints*, February 2015.

- V. M. Slipher. Radial velocity observations of spiral nebulae. *The Observatory*, 40:304--306, August 1917.
- G. F. Smoot. COBE observations and results. In L. Maiani, F. Melchiorri, and N. Vittorio, editors, *3K cosmology*, volume 476 of *American Institute of Physics Conference Series*, pages 1--10, May 1999. DOI: 10.1063/1.59326.
- J. G. v Soldner. Ueber die Ablenkung eines Lichtstrals von seiner geradlinigen Bewegung, durch die Attraktion eines Weltkörpers, an welchem er nahe vorbei geht. *Astronomisches Jahrbuch für das Jahr 1804*, pages 161--172, March 1804.
- G. Soucail, B. Fort, Y. Mellier, and J. P. Picat. A blue ring-like structure, in the center of the A 370 cluster of galaxies. *Astronomy & Astrophysics*, 172:L14--L16, January 1987.
- G. Soucail, Y. Mellier, B. Fort, G. Mathez, and M. Cailloux. The giant arc in A 370 - Spectroscopic evidence for gravitational lensing from a source at $Z = 0.724$. *Astronomy & Astrophysics*, 191:L19--L21, February 1988.
- V. Springel, S. D. M. White, A. Jenkins, C. S. Frenk, N. Yoshida, L. Gao, J. Navarro, R. Thacker, D. Croton, J. Helly, J. A. Peacock, S. Cole, P. Thomas, H. Couchman, A. Evrard, J. Colberg, and F. Pearce. Simulations of the formation, evolution and clustering of galaxies and quasars. *Nature*, 435: 629--636, June 2005. DOI: 10.1038/nature03597.
- G. Steigman. Primordial Nucleosynthesis in the Precision Cosmology Era. *Annual Review of Nuclear and Particle Science*, 57:463--491, November 2007. DOI: 10.1146/annurev.nucl.56.080805.140437.
- W. R. Stoeger, R. Maartens, and G. F. R. Ellis. Proving almost-homogeneity of the universe: an almost Ehlers-Geren-Sachs theorem. *Astrophysical Journal*, 443:1--5, April 1995. DOI: 10.1086/175496.
- N. R. Tanvir, D. B. Fox, A. J. Levan, E. Berger, K. Wiersema, J. P. U. Fynbo, A. Cucchiara, T. Krühler, N. Gehrels, J. S. Bloom, J. Greiner, P. A. Evans, E. Rol, F. Olivares, J. Hjorth, P. Jakobsson, J. Farihi, R. Willingale, R. L. C. Starling, S. B.

- Cenko, D. Perley, J. R. Maund, J. Duke, R. A. M. J. Wijers, A. J. Adamson, A. Allan, M. N. Bremer, D. N. Burrows, A. J. Castro-Tirado, B. Cavanagh, A. de Ugarte Postigo, M. A. Dopita, T. A. Fatkhullin, A. S. Fruchter, R. J. Foley, J. Gorosabel, J. Kennea, T. Kerr, S. Klose, H. A. Krimm, V. N. Komarova, S. R. Kulkarni, A. S. Moskvitin, C. G. Mundell, T. Naylor, K. Page, B. E. Penprase, M. Perri, P. Podsiadlowski, K. Roth, R. E. Rutledge, T. Sakamoto, P. Schady, B. P. Schmidt, A. M. Soderberg, J. Sollerman, A. W. Stephens, G. Stratta, T. N. Ukwatta, D. Watson, E. Westra, T. Wold, and C. Wolf. A γ -ray burst at a redshift of $z \sim 8.2$. *Nature*, 461: 1254--1257, October 2009. DOI: 10.1038/nature08459.
- J. Tinker, A. V. Kravtsov, A. Klypin, K. Abazajian, M. Warren, G. Yepes, S. Gottlöber, and D. E. Holz. Toward a Halo Mass Function for Precision Cosmology: The Limits of Universality. *Astrophysical Journal*, 688:709--728, December 2008. DOI: 10.1086/591439.
- L. van Waerbeke. Noise properties of gravitational lens mass reconstruction. *Monthly Notices of the Royal Astronomical Society*, 313:524--532, April 2000.
- M. P. Viero, V. Asboth, I. G. Roseboom, L. Moncelsi, G. Marsden, E. Mentuch Cooper, M. Zemcov, G. Addison, A. J. Baker, A. Beelen, J. Bock, C. Bridge, A. Conley, M. J. Devlin, O. Doré, D. Farrah, S. Finkelstein, A. Font-Ribera, J. E. Geach, K. Gebhardt, A. Gill, J. Glenn, A. Hajian, M. Halpern, S. Jogee, P. Kurczynski, A. Lapi, M. Negrello, S. J. Oliver, C. Papovich, R. Quadri, N. Ross, D. Scott, B. Schulz, R. Somerville, D. N. Spergel, J. D. Vieira, L. Wang, and R. Wechsler. The Herschel Stripe 82 Survey (HerS): Maps and Early Catalog. *Astrophysical Journal, Supplement*, 210:22, February 2014. DOI: 10.1088/0067-0049/210/2/22.
- A. Vikhlinin, B. R. McNamara, A. Hornstrup, H. Quintana, W. Forman, C. Jones, and M. Way. X-Ray Overluminous Elliptical Galaxies: A New Class of Mass Concentrations in the Universe? *Astrophysical Journal Letters*, 520:L1--L4, July 1999. DOI: 10.1086/312134.

- A. Voevodkin, K. Borozdin, K. Heitmann, S. Habib, A. Vikhlinin, A. Mescheryakov, A. Hornstrup, and R. Burenin. Fossil Systems in the 400d Cluster Catalog. *Astrophysical Journal*, 708:1376--1387, January 2010. DOI: 10.1088/0004-637X/708/2/1376.
- M. Vogelsberger, S. Genel, V. Springel, P. Torrey, D. Sijacki, D. Xu, G. Snyder, D. Nelson, and L. Hernquist. Introducing the Illustris Project: simulating the coevolution of dark and visible matter in the Universe. *Monthly Notices of the Royal Astronomical Society*, 444:1518--1547, October 2014. DOI: 10.1093/mnras/stu1536.
- A. M. von Benda-Beckmann, E. D'Onghia, S. Gottlöber, M. Hoeft, A. Khalatyan, A. Klypin, and V. Müller. The fossil phase in the life of a galaxy group. *Monthly Notices of the Royal Astronomical Society*, 386:2345--2352, June 2008. DOI: 10.1111/j.1365-2966.2008.13221.x.
- A. von der Linden, P. N. Best, G. Kauffmann, and S. D. M. White. How special are brightest group and cluster galaxies? *Monthly Notices of the Royal Astronomical Society*, 379:867--893, August 2007. DOI: 10.1111/j.1365-2966.2007.11940.x.
- D. Walsh, R. F. Carswell, and R. J. Weymann. 0957 + 561 A, B - Twin quasistellar objects or gravitational lens. *Nature*, 279: 381--384, May 1979. DOI: 10.1038/279381a0.
- D. H. Weinberg, M. J. Mortonson, D. J. Eisenstein, C. Hirata, A. G. Riess, and E. Rozo. Observational probes of cosmic acceleration. *Physics Reports*, 530:87--255, September 2013. DOI: 10.1016/j.physrep.2013.05.001.
- S. Weinberg. *Cosmology*. Oxford University Press, 2008.
- C. M. Will. The Confrontation between General Relativity and Experiment. *Living Reviews in Relativity*, 17:4, June 2014. DOI: 10.12942/lrr-2014-4.
- C. O. Wright and T. G. Brainerd. Gravitational Lensing by NFW Halos. *Astrophysical Journal*, 534:34--40, May 2000. DOI: 10.1086/308744.

- X. Yang, H. J. Mo, F. C. van den Bosch, Y. P. Jing, S. M. Weinmann, and M. Meneghetti. Weak lensing by galaxies in groups and clusters - I. Theoretical expectations. *Monthly Notices of the Royal Astronomical Society*, 373:1159--1172, December 2006. DOI: 10.1111/j.1365-2966.2006.11091.x.
- Y. B. Zel'dovich. Gravitational instability: An approximate theory for large density perturbations. *Astronomy & Astrophysics*, 5: 84--89, March 1970.
- A. Zitrin, I. Labbe, S. Belli, R. Bouwens, R. S. Ellis, G. Roberts-Borsani, D. P. Stark, P. A. Oesch, and R. Smit. Lyman-alpha Emission from a Luminous $z=8.68$ Galaxy: Implications for Galaxies as Tracers of Cosmic Reionization. *ArXiv e-prints*, July 2015.
- F. Zwicky. Die Rotverschiebung von extragalaktischen Nebeln. *Helvetica Physica Acta*, 6:110--127, 1933.
- F. Zwicky. Nebulae as Gravitational Lenses. *Physical Review*, 51: 290--290, February 1937. DOI: 10.1103/PhysRev.51.290.

Index

- Acceleration equation, 29
- Bias, 51
- Big Bang, 36
- Brightest Cluster Galaxy, 56, 61
- Bullet Cluster, 56
- c_{200} , 90
- Caustic, 71
- Central Galaxy, 56
- Comoving Coordinates, 34
- Congruence, 27
- Cooling flows, 57
- Corrected concentration c_{200}^{corr} , 113
- Correlation Function, 43
- Cosmic Microwave Background, 36, 41
- Cosmological Model, 31
- Cosmological Principle, 29
- Cosmological Simulations, 42
- Covariant Conservation, 33
- Critical curves, 71
- Critical surface density of the lens, 69
- Curvature Density, 32
- Density Contrast, 38
- Density Fractions, 32
- Dynamical friction, 55
- Einstein
 - Field Equations, 27
 - Radius, 71
 - Ring, 71
 - Theory of Gravity, 26
- emcee, 100
- Etherington's reciprocity relation, 36
- Expanding universe, 30
- Filtered variance (σ_R^2), 49
- Flexions, 72
- Fossil
 - Clusters, 62
 - Fraction, 89
 - Groups, 61
 - Optical candidates, 64
- Phase, 63
- Friedmann Equation, 31
- Friedmann-Lemaître Model, 29
- Galaxy Groups, 57
- General Relativity, see Einstein's Theory of Gravity 26
- Growing Mode, 39
- Growth Function, 39
- Hierarchical scenario, 47
- Hubble
 - Horizon, 35
- Jeans Length, 41
- L^* galaxies, 57
- Lens equation, 68
- Lensing
 - Jacobian, 70
 - Potential, 69
 - Signal, 95
 - Strong, 71
 - Weak, 71, 72
- Likelihood, 99
- Luminosity, 101
- Luminosity Function, 62
- M_{200} , 90
- Magnification, 71
- Mass function, 48
- Mass-sheet degeneracy, 74
- Mass-to-light ratio, 101
- MCMC, 98
- Measured $\Delta\Sigma$ s, 103
- Miscentering, 91, 117
- Model comparison, 110
- Multiple fitting, 122
- Mészáros
 - Effect, 40
 - Equation, 40
- Nuisance parameters, 94
- Observables, 57
- OLEGs, 117
- Parameter estimation, 104
- Parametric modelling, 75, 89
- Peak-background split, 51
- Perturbation Theory, 38
- Power Spectrum, 43
- Press Schechter model, 49
- Priors, 100
- Profile
 - BMO, 48
 - Einasto, 48
 - NFW, 47, 90
- Projected mass density, 53, 90
- Raychaudhuri's Equation, 29
- Red sequence, 55
- Reduced shear, 74
- Results, 103
- Ricci Identity, 28
- Robertson-Walker Metric, 29
- Shear (γ), 70
- Standard Candles, 35
- Tensor
 - expansion, 27
 - Ricci, 27
 - Riemann, 27
 - shear, 28
 - vorticity, 28
- Thin lens limit, 67
- Tinker mass function, 51
- Top Hat Model, 46
- Topology, 30
- Two-halo term, 53, 93
- Universality, 48
- Violent Relaxation, 55
- Virial Overdensity, 47
- Walkers, 100